

Nuclear Structure of ^{80}Sr and ^{85}Y

by

Valan Q Wood

B.S., University of California, 1993

M.S., University of Pittsburgh, 1995

Submitted to the Graduate Faculty of
Arts and Sciences in partial fulfillment
of the requirements for the degree of
Doctor of Philosophy

University of Pittsburgh

2000

UNIVERSITY OF PITTSBURGH

FACULTY OF ARTS AND SCIENCES

This dissertation was presented

by

Valan Q Wood

It was defended on

2000

and approved by

Prof. Jurg X. Saladin (Chairman)

Prof. C. Martin Vincent

Prof. Frank Tabakin

Prof. Paul Shepard

Prof. Joel Falk

Committee Chairperson(s)

Nuclear Structure of ^{80}Sr and ^{85}Y

Valan Q Wood, Ph.D.

University of Pittsburgh, 2000

High-spin states in ^{80}Sr and ^{85}Y were investigated using the detector arrays Gammasphere and Microball, at the 88-Inch Cyclotron at LBNL. ^{80}Sr was populated with the reaction $^{58}\text{Ni}(^{29}\text{Si}, \alpha 2pn)^{80}\text{Sr}$ using a 128 MeV beam, and with the reaction $^{58}\text{Ni}(^{29}\text{Si}, \alpha 2pn)^{80}\text{Sr}$ using a 130 MeV beam. ^{85}Y was populated with the reaction $^{58}\text{Ni}(^{31}\text{P}, 4p)^{85}\text{Y}$ using a 134 MeV beam. Data was analyzed using coincidence analysis, lifetime measurements for ^{80}Sr , and angular distributions. New structures in the expanded level schemes are reported, including a tentative superdeformed band in ^{85}Y . Results are discussed in terms of a Cranked Shell Model and compared to theoretical cranked Woods-Saxon shell model calculations. Based on the comparison between these calculations and the experimental results, shape evolution for both isotopes are suggested. Band termination was investigated for ^{80}Sr , but no evidence for band termination was found.

Contents

List of Figures	vi
List of Tables	x
1 INTRODUCTION	1
2 THEORETICAL BACKGROUND	3
2.1 The Liquid Drop Model	3
2.1.1 Semi-empirical Mass Formula	4
2.1.2 Deformation and Shape Parameterization	7
2.2 Shell Model	10
2.2.1 The Spherical Shell Model	11
2.2.2 Nuclear Density	12
2.2.3 Woods-Saxon Potential	12
2.2.4 Nilsson Deformed Potential Model	14
2.3 Collective Motion	17
2.4 Cranking Model	19
2.4.1 Cranking About the Symmetry Axis	21
2.4.2 Cranking Perpendicular to the Symmetry Axis	23
2.5 Cranked Mean-Field Calculation with Pairing	23
2.6 Strutinsky Shell Correction	26
2.7 Comparing Theory to Experiment	28
3 EXPERIMENT AND ANALYSIS METHODS	31
3.1 Population of High Spin Nuclear States	31
3.2 Gammasphere Detector Array at LBNL	32
3.2.1 Compton-suppressed germanium detectors	34
3.3 Microball Detector Array	35
3.4 Data Analysis	37
3.4.1 Kinematics	37
3.4.2 Coincidence Analysis	39
3.4.3 Background Subtraction	42
3.4.4 Gamma Decay and Gamma Angular Distributions	44
4 RESULTS AND DISCUSSION	50
4.1 Strontium 80	50

4.1.1	Experimental Specifics	50
4.1.2	Results Using Thin Target Data	52
4.1.3	Backed-Target Data: Lifetimes and Intrinsic Quadrupole Moments	61
4.1.4	Cranking Analysis	64
4.1.5	Comparison to cranked mean-field with pairing Calculations	68
4.2	Yttrium 85	73
4.2.1	Experimental Specifics	73
4.2.2	Results	74
4.2.3	Level Scheme	78
4.2.3.1	Yrast Band	81
4.2.3.2	Bands 1, 2 and Possible New Band	82
4.2.3.3	Negative Parity Bands 4 and 5	83
4.2.3.4	Band 6	84
4.2.4	Discussion	86
4.2.4.1	Cranking Model Analysis	87
4.2.4.2	Cranked mean-field calculations	89
4.2.4.3	Shape mixing and the decay out of the $37/2^+$ state	93
5	SUMMARY	96
	Bibliography	98

List of Figures

2.1	Empirical specific binding energies (B/A) compared with the average curve representing the semi-empirical mass formula. Deviations mark shell structure effects. The nuclei are chosen along the line of β -stability while the inset shows $N = Z$ nuclei. [2]	6
2.2	A deformed nuclear surface described by a function $R(\theta, \phi)$	7
2.3	The three principal axes R_1 , R_2 , and R_3 of a general quadrupole deformed nucleus.	9
2.4	Woods-Saxon potential.	13
2.5	Deformed energy level diagram for a Woods-Saxon potential. Energy is indicated in units of MeV. States are labeled on the right by Ω and parity. Each state is two-fold degenerate with signature states of $\alpha = +1/2$ and $\alpha = -1/2$. Underlined numbers labeled in gaps indicate the number of states below the gap.	16
2.6	Idealized example of low spin decay sequence for an even-even nucleus. The energy of each state is labeled on the left. The spin of each state is labeled on the right. Decay transitions are indicated with arrows.	18
2.7	The total angular momentum \vec{I} is the sum of the intrinsic angular momentum \vec{J} and the collective angular momentum \vec{R} . For a nucleus with an axis of symmetry (here chosen as the x_3 axis), the values Ω and K are the projection onto the symmetry axis of the intrinsic and total angular momentum respectively.	19
2.8	When cranking about the x_1 axis (in the figure, the x_1 axis is coming out of the page) with angular velocity ω , the lab frame x, y, z , and intrinsic frame x_1, x_2, x_3 are related as shown.	21
2.9	Schematic plot of single particle Routhians as a function of ω for the case of rotation around the symmetry axis.	22
2.10	Example of smoothed energy levels used for Strutinsky smoothing.	27

2.11	Components of the angular momentum shown for the case of rotation about the x axis, where the x axis is perpendicular to the symmetry or x_3 axis.	28
3.1	A schematic diagram showing the decay of a compound nucleus from the reaction $^{124}\text{Sn}(^{40}\text{Ar}, xn)^{164-x}\text{Er}$ with a beam energy of 147 MeV. The middle plot shows the energy vs. angular momentum of the system. Below and to the left are intensity profiles for the entry populations of the 3n, 4n, and 5n channels. The top plot shows the expected input angular momentum for this experiment [10].	33
3.2	Two sample spectra demonstrating the affect of Compton suppression. The spectra contain two peaks with tails due to Compton scattering. The Compton suppressed spectrum has peak to total ratio much higher than the unsuppressed spectrum.	35
3.3	Picture of Microball placed inside of one hemisphere of Gammasphere.	36
3.4	Diagram of the kinematics in a beam on target experiment: a) A projectile nucleus is incident on a target nucleus; b) The projectile and target nuclei fuse together to form a compound nucleus; c) The compound nucleus evaporates neutrons, protons, and/or α particles; d) The product nucleus decays through electromagnetic emission (\vec{q} being the momentum of the γ ray).	37
3.5	Emission of a γ ray in the a) lab frame and b) nuclear rest frame. . .	38
3.6	Schematic of the gates of a coincidence matrix from a sample level scheme.[13] (a) The sample level structure. (b) Spectra that result from various gates.	41
3.7	A sample plot of the total projection of a coincidence matrix. At $i = 930$ keV, $P_i \approx 3.5 \times 10^7$ counts and the estimated background $b_i \approx 1.3 \times 10^7$ counts.	43
3.8	Decay from a spin and parity $I^\pi = 4^+$ state into a $I^\pi = 3^+$ state. . . .	45
3.9	Plot of a_k for a change in angular momentum of $2\hbar$ ($J \rightarrow J - 2$). The solid line is calculated for an initial angular momentum of $10\hbar$ and final angular momentum of $8\hbar$. The dashed line is calculated for an initial angular momentum of $7\hbar$ and final angular momentum of $5\hbar$. Mixing ratio δ is the ratio of octupole to quadrupole transition strengths. . .	47

3.10	Plot of a_k for a change in angular momentum of $1\hbar$ ($J \rightarrow J - 1$). The solid line is calculated for an initial angular momentum of $10\hbar$ and final angular momentum of $9\hbar$. The dashed line is calculated for an initial angular momentum of $6\hbar$ and final angular momentum of $5\hbar$. Mixing ratio δ is the ratio of dipole to quadrupole transition strengths.	48
4.1	Total projection of the $\alpha 2p$ channel.	52
4.2	Deduced level scheme of ^{80}Sr	54
4.3	Gates on the $\alpha 2p$ channel.	55
4.4	More gates on the $\alpha 2p$ channel.	56
4.5	Angular distributions	57
4.6	Example of backed target data, showing DBLS fit. The line shown is the 1065 keV $10^+ \rightarrow 8^+$ transition.	63
4.7	Transition quadrupole moments in the ground-state band derived from lineshape analysis. Also shown are results from an earlier work in ^{80}Sr	64
4.8	Experimental $\mathfrak{S}^{(1)}$ and $\mathfrak{S}^{(2)}$ for the ground state band in ^{80}Sr	65
4.9	Experimental $\mathfrak{S}^{(1)}$ and $\mathfrak{S}^{(2)}$ for the side bands in ^{80}Sr	67
4.10	TRS surfaces calculated for ^{80}Sr . The angular velocity is labeled in each plot in units of MeV/\hbar . For $\omega = 0.2 \text{ MeV}/\hbar$, the deepest minima is labeled 'a'. Another local minima exists at coordinates $(\beta = 0.20, \gamma = -60^\circ)$, and two more local minima $(\beta = 0.20, \gamma = +60^\circ)$ and $(\beta = 0.35, \gamma = -120^\circ)$ which are due to the symmetry related with low angular velocity. Local maxima exist at $(\beta = 0.20, \gamma = 0^\circ)$ and $(\beta = 0.20, \gamma = -120^\circ)$. At $\omega = 0.6 \text{ MeV}/\hbar$ the local maximum at $\gamma = 0^\circ$ has disappeared. At $\omega = 0.8 \text{ MeV}/\hbar$ only two local minima remain.	69
4.11	Theoretical $\mathfrak{S}^{(1)}$ for ^{80}Sr	70
4.12	Figure obtained from Nazarewicz <i>et al.</i> [29] for the energies of even signature states of ^{80}Sr at various deformations described in the inset using the Hill-Wheeler coordinates.	71
4.13	Figure obtained from Nazarewicz <i>et al.</i> [29] for the energies of odd signature states of ^{80}Sr at various deformations described in the inset using the Hill-Wheeler coordinates.	72
4.14	Total projection of data from the ^{85}Y experiment.	74
4.15	Deduced level scheme for ^{85}Y	75

4.16	Some gated spectra for ^{85}Y	76
4.17	Angular distributions for some transitions in ^{85}Y	77
4.18	Summed singles spectra for the superdeformed band.	85
4.19	Decay sequence for the $(\pi, \alpha) = (+, +)$ states drawn to illustrate the forking. Path 1 indicates the entire decay sequence that passes through band 1, and path 2 indicates the entire decay sequence through the yrast states in band 3.	86
4.20	(a) Experimental $\mathfrak{S}^{(1)}$ and (b) Routhians for paths 1 (solid) and 3 (dashed), showing the backbends in each case.	88
4.21	Total Routhian surfaces for ^{85}Y	90
4.22	$\mathfrak{S}^{(1)}$ plot comparing experiment to HFBC calculations for lowest energy $(\pi, \alpha) = (+, +)$ prolate deformation ($\beta_2 = 0.27$, $\gamma = -11$, $\beta_4 = 0.010$). The circles indicate the data for band 3, the solid line indicates theory. The long and medium dashed lines represent the theoretical proton and neutron contributions respectively. The theoretical calculations are for $0.4 \text{ MeV} < \hbar\omega < 0.7 \text{ MeV}$	91
4.23	$\mathfrak{S}^{(1)}$ plot comparing experiment to HFBC calculations for lowest energy $(\pi, \alpha) = (+, +)$ oblate deformation ($\beta_2 = 0.27$, $\gamma = -57$, $\beta_4 = 0.010$). The circles represent data along decay path 1, the solid line indicates theory. The long and medium dashed lines represent the proton and neutron contributions respectively.	92
4.24	Schematic branching scheme. Note that the states ψ and ψ' are very close in energy. Their separation is exaggerated in the figure.	94

List of Tables

3.1	Selection rules tabled by the angular momentum and parity of the γ ray.	44
4.1	Partial table of transitions in ^{80}Sr .	60
4.2	Measured lifetimes and quadrupole moments for selected transitions in the GSB and SB1 of ^{80}Sr .	63
4.3	Table of transitions in ^{85}Y for bands 1 and 2.	79
4.4	Table of transitions in ^{85}Y for band 3.	79
4.5	Table of transitions in ^{85}Y for bands 4 and 5.	80
4.6	Table of transitions in ^{85}Y for band 6 and some of the levels in the level scheme that do not appear to belong to a band.	80
4.7	Table of transitions in ^{85}Y for some of the levels in the level scheme that do not appear to belong to a band.	81

Chapter 1

INTRODUCTION

High spin spectroscopy is at the forefront of Nuclear Structure research. At the outset of this thesis work, new state of the art instrumentation, namely Gammasphere and Microball, have become available to study the behavior of nuclei at large angular momenta. Gammasphere is an array of up to 110 Compton suppressed Ge detectors for γ ray spectroscopy. Microball consists of 98 CsI detectors covering a solid angle of nearly 4π and permitting to identify light charged particles like protons, deuterons, and α particles, and to measure their energies and angles of emission. The combination of these two instruments makes it possible to separate different reaction channels and to conduct high resolution γ ray spectroscopy on each of these reaction channels.

The theoretical motivation for these experiments was based on behavior of rotational bands at high spins, including sudden changes of moments of inertia, shape changes, and the occurrence of so-called super deformed states.

^{80}Sr and ^{85}Y were studied and are discussed in chapter 4. Band termination, superdeformation, and shape evolution are primary topics. State of the art theoretical models are described in chapter 2, which lays out the theoretical framework used

in the analysis of the data. Chapter 3 describes the experimental methods and some of the analysis techniques. The experimental setup is briefly described in this thesis; the instruments used belong to the National Facility “Gammasphere” and the experiments were carried out at Lawrence Berkeley National Laboratory (LBNL). The analysis techniques include coincidence analysis, lifetime measurements, and angular distributions.

Chapter 2

THEORETICAL BACKGROUND

2.1 The Liquid Drop Model

The earliest model of nuclear structure proposed was the liquid drop model. It still yields many useful insights, since there are a number of similarities between a nucleus and a liquid drop. The density of nuclear matter is almost independent of mass number. This indicates that nuclear matter is nearly incompressible. Otherwise nuclear density would be larger for larger nuclei as the binding forces increase. The total binding energy of a nucleus is approximately proportional to the number of nucleons. This is analogous to the energy required to completely evaporate a liquid drop. The surface tension of a liquid drop causes a correction to this relation because the binding energy of the surface molecules is somewhat smaller than that of the interior molecules. This is similar to the smaller binding energy per nucleon at the surface of a nucleus.

The similarities between a nucleus and a liquid drop arise from the fact that in both a nucleus and a liquid drop, the constituent particles have a strong repulsion at close range but attract beyond that range. In a nucleus this comes from the form

of the strong force. Between about 1 fm (10^{-15} m) and 2 fm there exists a minimum in the potential of the strong force that holds nucleons at about that distance from each other.

There is an important scale difference between a nucleus and a liquid drop. The scales of the kinetic energy and interparticle distance lead to a significant physical difference between a nucleus and a liquid drop. The kinetic energy of a typical molecule in a liquid may be around 0.025 eV. The corresponding de Broglie wavelength is about 1.8×10^{-10} m. This is very much smaller than the distance between molecules. A typical nucleon might have about 30 MeV of kinetic energy. The corresponding de Broglie wavelength is about 3×10^{-15} m, which is about the same as the internucleon distance. Hence, in ordinary liquids, the motion of the constituents can be described in classical terms and their positions can be well defined, compared to their mutual distance, whereas in nuclei the motion is necessarily of quantum character, since the uncertainty in the localization of the constituents is of the order of magnitude of their distance.

We will now develop some useful ideas on binding energy and shape that are suggested by the liquid drop model.

2.1.1 Semi-empirical Mass Formula

The semi-empirical mass formula, which describes the binding energies of nuclei, was motivated by the liquid drop model. The nuclear binding energy $B(N, Z)$ can be defined in the following way

$$m(N, Z) = \frac{1}{c^2} E(N, Z) = NM_n + ZM_p - \frac{1}{c^2} B(N, Z) \quad (2.1)$$

where the nuclear mass m is a function of neutron number N and proton number Z and $NM_n + ZM_p$ is the total mass of the constituent nucleons. The binding energy $B(N, Z)$ can then be calculated from measured isotope masses. The semi-empirical mass formula $B(N, Z)$ is given below

$$B(N, Z) = a_v A - a_s A^{2/3} - a_c \frac{Z^2}{A^{1/3}} - a_I \frac{(N - Z)^2}{A} - \delta A^{-3/4} \quad (2.2)$$

where A is the nuclear mass number, and a_v , a_s , a_c , a_I , and δ are adjusted for the best fit to known nuclear masses. Values of these parameters are $a_v = 15.677$ MeV, $a_s = 18.56$ MeV, $a_c = 0.717$ MeV, $a_I = 28.1$ MeV, and $\delta = 34$ MeV for odd-odd nuclei, 0 for odd-even nuclei, and -34 MeV for even-even nuclei [1]. Figure 2.1 shows experimental binding energies per nucleon for stable nuclei. The points indicate data, and the smooth line is from the semi-empirical mass formula. Each term in this formula has a definite physical interpretation. The term $a_v A$ is proportional to the number of nucleons, which is proportional to volume since nuclear matter is incompressible. The term $a_s A^{2/3}$ is proportional to surface area and models the surface tension energy. The term $a_c \frac{Z^2}{A^{1/3}}$ is the Coulomb repulsion energy. The term $a_I \frac{(N-Z)^2}{A}$ describes the energy contribution resulting from unequal numbers of protons and neutrons so that if Z and N are equal, its contribution is zero. This term can be thought of as an effect of the Pauli exclusion principle. The lowest states for each type of nucleon are filled first, so having unequal numbers of the two types of nucleons will require that higher energy states be filled. The last term describes pairing energy.

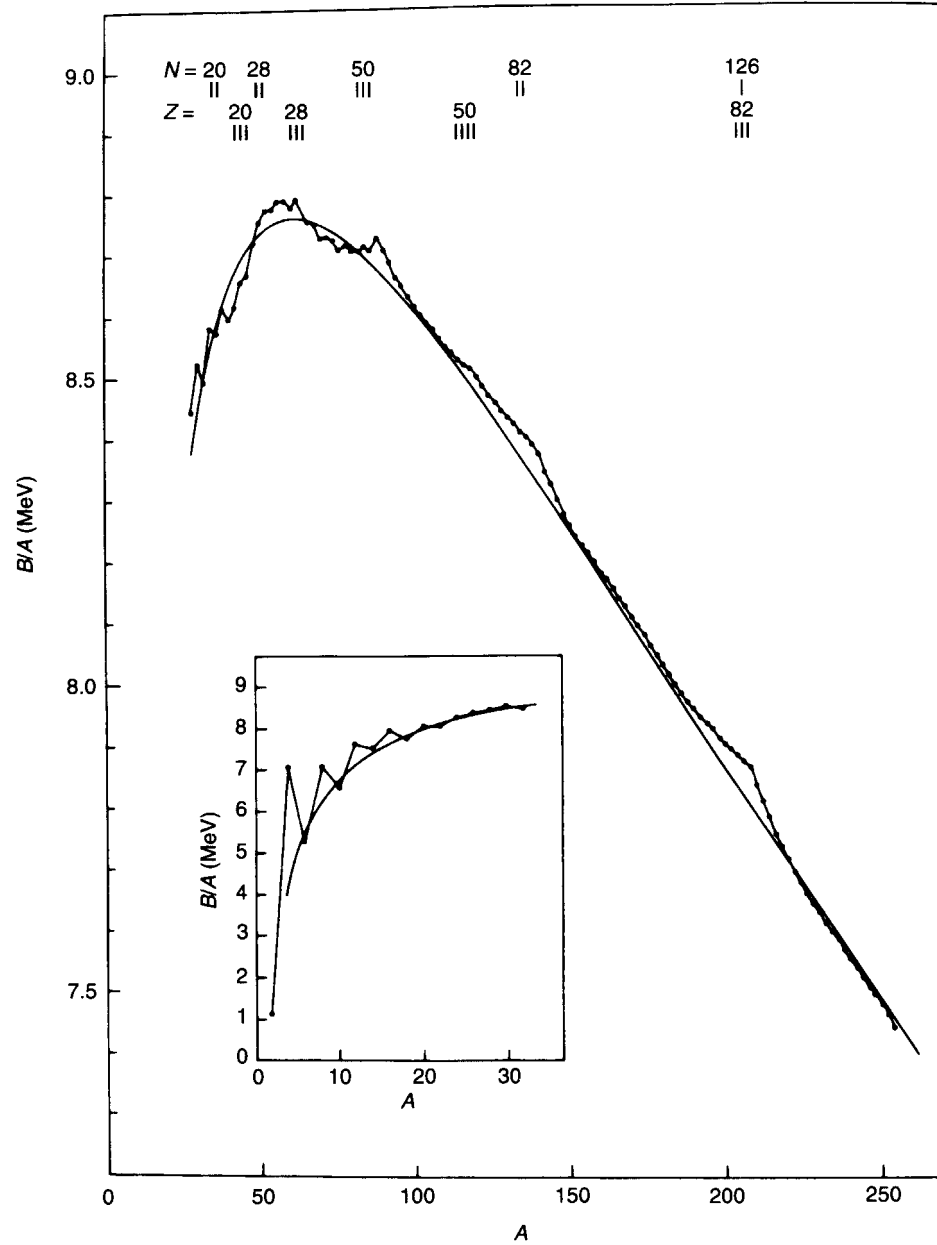


Figure 2.1: Empirical specific binding energies (B/A) compared with the average curve representing the semi-empirical mass formula. Deviations mark shell structure effects. The nuclei are chosen along the line of β -stability while the inset shows $N = Z$ nuclei. [2]

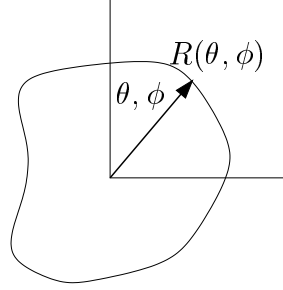


Figure 2.2: A deformed nuclear surface described by a function $R(\theta, \phi)$.

2.1.2 Deformation and Shape Parameterization

Like a liquid drop, a nucleus may also experience deformations and shape changes. For a strongly deformed nucleus, the oscillations introduce small effects compared to those of deformation. In the mass 80 region, rarely are nuclei found to be spherical, so we will focus on permanent deformation without discussing oscillations. So it is important to consider the shape of a nucleus in detail.

A deformed nuclear surface can be described by a function $R(\theta, \phi)$ that gives the distance from the center of mass to a point on the surface as shown in Fig. 2.2, where θ is the angle from the azimuthal axis and ϕ is the angle about the azimuthal axis. A general form for $R(\theta, \phi)$ can be expressed as a sum of spherical harmonics $Y_{\lambda\mu}$:

$$R(\theta, \phi) = R_0 \left[1 + \sum_{\lambda=0}^{\infty} \sum_{\mu=-\lambda}^{\lambda} \alpha_{\lambda\mu} Y_{\lambda\mu}(\theta, \phi) \right], \quad (2.3)$$

where $\alpha_{\lambda\mu}$ and R_0 define the particular surface. This formula can be simplified for the specific purpose of describing the surface of a deformed nucleus. The $\lambda = 0$ term is not dependent on θ or ϕ : $\alpha_{00} Y_{00}(\theta, \phi) = \alpha_{00} / \sqrt{4\pi}$. So expression (2.3) can be

rearranged as:

$$R(\theta, \phi) = R_0 \left(1 + \frac{\alpha_{00}}{\sqrt{4\pi}} \right) \left[1 + \sum_{\lambda=1}^{\infty} \sum_{\mu=-\lambda}^{\lambda} \frac{\alpha_{\lambda\mu}}{1 + \frac{\alpha_{00}}{\sqrt{4\pi}}} Y_{\lambda\mu}(\theta, \phi) \right]. \quad (2.4)$$

A redundancy can be seen from this. The $\lambda = 0$ term can be removed and R_0 and $\alpha_{\mu\lambda}$ redefined by factors of $\left(1 + \frac{\alpha_{00}}{\sqrt{4\pi}} \right)^{-1}$. Alternatively, R_0 can be chosen for a spherical nucleus, and then for a deformed nucleus the value of a_{00} can be determined so that the deformed nucleus and the spherical nucleus have the same volume. Keeping the volume the same is physically important because of the incompressibility of nuclear matter. These two methods produce identical surfaces, but the deformation parameters are defined differently by the factor of $\left(1 + \frac{\alpha_{00}}{\sqrt{4\pi}} \right)$. For small deformations, terms with $\lambda = 1$ would correspond to a translation of the center of mass. Since $R(\theta, \phi)$ is defined in the center of mass reference frame, this would be a violation of conservation of momentum, so terms with $\lambda = 1$ must be zero. Finally, since $R(\theta, \phi)$ is real and $Y_{\lambda\mu}^* = (-1)^\mu Y_{\lambda-\mu}$ we can conclude that

$$\alpha_{\lambda\mu}^* = (-1)^\mu \alpha_{\lambda-\mu} \quad (2.5)$$

so that the imaginary parts of eq. (2.4) add to zero.

The terms with $\lambda = 2$ are the most significant terms in describing the deformation of a nucleus. The $\lambda = 0$ and $\lambda = 1$ terms have been discussed with regards to volume conservation and translation respectively. Terms with $\lambda = 3$ would remove the reflection symmetry, which would have an effect on the parities of observed states. Such effects have been observed in experiments. Terms with $\lambda \geq 4$ have much smaller coefficients than the $\lambda = 2$ terms.

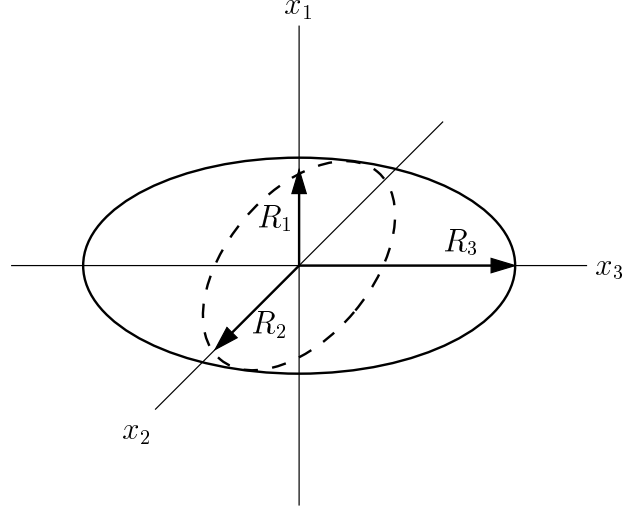


Figure 2.3: The three principal axes R_1 , R_2 , and R_3 of a general quadrupole deformed nucleus.

For a quadrupole deformation ($\lambda = 2$) there are five coefficients: α_{22} , α_{21} , α_{20} , α_{2-1} , and α_{2-2} which correspond to five degrees of freedom. Of these five degrees of freedom, three describe the orientation. A rotational transformation from space fixed axes (x, y, z) to body fixed axes (x_1, x_2, x_3) can be performed so that the five coefficients are transformed into five new coefficients a_{22} , a_{21} , a_{20} , a_{2-1} , and a_{2-2} . From eq. (2.5) we know that $a_{21}^* = -a_{2-1}$ and $a_{22} = a_{2-2}$. A rotation chosen so that the coefficients $a_{21} = a_{2-1} = 0$ orients the principal axes of the nucleus along the coordinate axes. The lengths of the principal axes can then be related to the coefficients $a_{22} = a_{2-2}$ and a_{20} . The following equation shows the relationship between a_{22} and a_{20} in terms of the three principal axis R_1 , R_2 , and R_3 as shown in Fig. 2.3:

$$\begin{aligned} a_{20} &= \frac{R_3 - R_0}{R_0} \sqrt{\frac{4\pi}{5}} \\ a_{22} &= \frac{R_1 - R_2}{R_0} \sqrt{\frac{2\pi}{15}} \end{aligned} \tag{2.6}$$

These two coefficients are often parameterized by the Hill-Wheeler coordinates (β, γ) as

$$\begin{aligned} a_{20} &= \beta \cos \gamma, \\ a_{22} &= \frac{1}{\sqrt{2}} \beta \sin \gamma. \end{aligned} \tag{2.7}$$

In this way $\beta = \sqrt{2a_{22}^2 + a_{20}^2}$ describes the magnitude of the deformation and $\gamma = \tan^{-1} \left(\frac{\sqrt{2}a_{22}}{a_{20}} \right)$ describes the deviation from axial symmetry. Note that if $\gamma = 0^\circ$ then a_{22} is zero, and the shape is symmetric about R_3 . For $\gamma = 60^\circ$ the shape is symmetric about R_1 . For $\gamma = -60^\circ$ the shape is symmetric about R_2 . In the intervals between these 60° points the shape is triaxial, so that the three principal axes have different lengths.

2.2 Shell Model

While the classical liquid drop model adequately describes some of the bulk properties of a nucleus, the nucleus is a quantum liquid and should be treated quantum mechanically. Constructing a Hamiltonian with a number of interacting particles typical of most nuclei leads to a mesoscopic system: there are too many degrees of freedom to solve exactly but too few to be treated statistically. Since the nucleus is a quantum liquid, we can approximate the motion of the individual nucleons as being independent of each other, and use a mean-field potential to approximate the potential that one nucleon feels from all other nucleons. Residual interactions that cannot be well approximated by a mean-field potential can be treated as corrections to the mean-field potential.

2.2.1 The Spherical Shell Model

Consider a nucleon in a spherically symmetric potential $V(r)$ where the Hamiltonian expressed in spherical coordinates is

$$H = -\frac{\hbar^2}{2M} \frac{1}{r} \frac{\partial^2}{\partial r^2} r + \frac{\vec{l}^2(\theta, \phi)}{2Mr^2} + V(r) \quad (2.8)$$

where $\vec{l}(\theta, \phi)$ is the angular momentum operator such that

$$\vec{l}^2 = -\hbar^2 \left[\frac{1}{\sin \theta} \frac{\partial}{\partial \theta} \left(\sin \theta \frac{\partial}{\partial \theta} \right) + \frac{1}{\sin^2 \theta} \frac{\partial^2}{\partial \phi^2} \right]. \quad (2.9)$$

Each eigenfunction of this Hamiltonian can be split into a radial part and an angular part. The radial part has principal quantum number n which corresponds to the number of radial nodes. The angular part is the spherical harmonic $Y_{lm}(\theta, \phi)$ which has quantum numbers l and m corresponding to the angular momentum of the state and the projection of the angular momentum onto an axis.

For the mean-field potential of a nucleus an additional degeneracy exists due to spin, since nucleons can have spin up or spin down. The spin degeneracy is split by adding to the Hamiltonian a spin-orbit term proportional to $\vec{l} \cdot \vec{s}$. With the splitting of this degeneracy, the number of nucleons in each shell agrees with the observed shell closure. Consider the operator \vec{j} which is the sum of the angular momentum and spin operator vectors $\vec{j} \equiv \vec{l} + \vec{s}$. Squaring both sides and solving for $2\vec{l} \cdot \vec{s}$ yields $2\vec{l} \cdot \vec{s} = \vec{j}^2 - \vec{l}^2 - \vec{s}^2$. Since \vec{l} , \vec{j} , and \vec{s} commute with the Hamiltonian, $2\vec{l} \cdot \vec{s}$ will also commute with the Hamiltonian. Then, expressing \vec{l} and \vec{s} in terms of the eigenvalues

$$2\vec{l} \cdot \vec{s} \rightarrow [j(j+1) - l(l+1) - s(s+1)]. \quad (2.10)$$

Then, for $s = \pm\frac{1}{2}$

$$2\langle \vec{l} \cdot \vec{s} \rangle = \begin{cases} l & \text{for } j = l + \frac{1}{2} \\ -l - 1 & \text{for } j = l - \frac{1}{2} \end{cases} . \quad (2.11)$$

So the inclusion of the spin-orbit term in the Hamiltonian with negative value and appropriate strength reproduces the observed energy splitting, decreasing the energy for $l + \frac{1}{2}$ states and increasing the energy for $l - \frac{1}{2}$ states.

2.2.2 Nuclear Density

Since the strong force has an interaction range shorter than the nuclear size, the mean-field potential should have a form similar to that of the nuclear density distribution. As mentioned, the nuclear density is relatively uniform inside the nucleus. At the surface the density smoothly decreases from 0.17 nucleons/fm³ to about one tenth of that over a range of about 2.5 fm. So the nuclear density can be quantitatively described by the density function

$$\rho(r) = \rho_0 \left[1 + \exp\left(\frac{r - R}{a}\right) \right]^{-1} \quad (2.12)$$

where $\rho_0 \approx 0.17$ nucleons/fm³, $R \approx 1.2A^{1/3}$ fm, and $a \approx 0.57$ fm.

2.2.3 Woods-Saxon Potential

The Woods-Saxon potential has radial dependence similar to that of the nuclear density distribution. A disadvantage of using the Woods-Saxon potential instead of a harmonic oscillator approximation is that the Hamiltonian with a Woods-Saxon potential cannot be solved analytically. The Woods-Saxon potential is

$$V_{WS}(r) = -V_0 \left\{ 1 + e^{[r-R_0]/a} \right\}^{-1} . \quad (2.13)$$

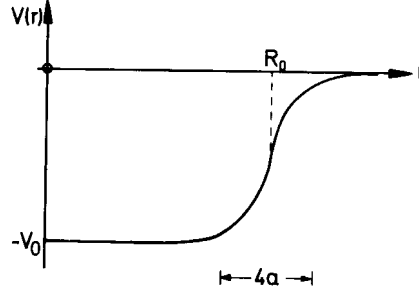


Figure 2.4: Woods-Saxon potential.

Appropriate values for the parameters are: well depth $V_0 = 50$ MeV, nuclear radius $R_0 = 1.2A^{1/3}$ fm, and surface thickness $a = 0.5$ fm. Dudek and Werner have done a survey to determine (N, Z) dependent values for these parameters to reproduce ground state spins and parities [3, 4, 5]. A schematic plot of the Woods-Saxon potential is shown in Fig. 2.4.

The Hamiltonian for the single-particle shell model must also include terms for the spin-orbit potential and Coulomb repulsion.

$$H_{WS} = T + V_{WS}(r) + \lambda \frac{1}{r} \frac{\partial V_{WS}(r)}{\partial r} \vec{l} \cdot \vec{s} + \frac{1}{2}(1 + \tau_3)V_{coul}(r). \quad (2.14)$$

The spin-orbit strength $\lambda \approx -0.5 fm^2$ is empirical, and τ_3 is the isospin. The Coulomb potential is calculated classically assuming the charge distribution is the same as the nuclear density with total charge equal to Z . For protons $\tau_3 = +1$, for neutrons $\tau_3 = -1$ so the Coulomb term is zero for neutrons and

$$V_{coul} = \frac{e^2}{4\pi\epsilon_0} \int \frac{\rho(\vec{r}')d^3r'}{|\vec{r} - \vec{r}'|} \quad (2.15)$$

for protons where $\rho(\vec{r}')$ is given by eq. (2.12) but with ρ_0 chosen so that the number of protons is $Z = \int \rho(\vec{r}')d^3r'$.

2.2.4 Nilsson Deformed Potential Model

Calculating energy levels for *deformed* nuclei was a primary motivation for the Nilsson model, so it introduces a Hamiltonian with an axially symmetric deformed harmonic oscillator potential.

$$H_{Nilsson} = T + V_{osc} + C\vec{l} \cdot \vec{s} + D\vec{l}^2 \quad (2.16)$$

where T is the kinetic energy, $V_{osc} = \frac{M}{2} [\omega_{\perp}^2 (x_1^2 + x_2^2) + \omega_3^2 x_3^2]$ is an axially symmetric harmonic oscillator potential, $\vec{l} \cdot \vec{s}$ is the spin-orbit coupling term, and \vec{l}^2 is the angular momentum term. The addition of the angular momentum term is to correct the harmonic oscillator potential so that nucleons will behave similar as if they were in a realistic nuclear potential. Nucleons with greater angular momentum are more likely to be at a greater r , where a realistic nuclear potential is lower than the harmonic oscillator potential. So a negative value of D in eq. (2.16) causes nucleons that are more likely to be at greater r to experience a lower energy, similar to if the potential was more like a Woods-Saxon potential. The purpose for doing this instead of using the Woods-Saxon potential was so that this model could be solved analytically. The Hamiltonian H can be written as follows: The harmonic oscillator can be related to the shape parameters described in section 2.1.2. Since this model is symmetric about the x_3 -axis, $a_{22} \propto R_1 - R_2 = 0$. From eq. (2.7) the triaxiality parameter γ is zero. We also find that $\beta = a_{20} \propto \omega_{\perp}^2 - \omega_0^2$.

As soon as a deformation is given to the potential, the spherical symmetry of the Hamiltonian is broken. The angular momentum operator \vec{l} no longer commutes with the Hamiltonian. Thus the energy eigenstates will have mixed orbital angular

momentum l . So l will no longer be a good quantum number. Similarly, the energy eigenstates will have mixed principal quantum number n , and n will no longer be a good quantum number for the energy eigenstates. The shape is symmetric about the x_3 -axis, so Ω , the projection of the total angular momentum on the x_3 -axis, will be a good quantum number. The shape is also symmetric by reflection about the origin, so parity will be a good quantum number. There is also a rotational symmetry, since the Hamiltonian is invariant under $R_1(\pi)$, a rotation of π radians about the x_1 axis. This symmetry is associated with the quantum number α called signature, where

$$R_1(\pi)\psi_\alpha = e^{-i\pi J_1}\psi_\alpha = e^{-i\pi\alpha}\psi_\alpha. \quad (2.17)$$

Note that α provides the same result for the exponential if α is increased or decreased by two. By convention we pick the four values of $\alpha = -1/2, 0, 1/2, 1$ to denote signature for the following spin sequences:

$$\alpha = 0 : \quad I = 0, 2, 4, \dots \quad (2.18)$$

$$\alpha = 1 : \quad I = 1, 3, 5, \dots \quad (2.19)$$

$$\alpha = +1/2 : \quad I = \frac{1}{2}, \frac{5}{2}, \frac{9}{2}, \dots \quad (2.20)$$

$$\alpha = -1/2 : \quad I = \frac{3}{2}, \frac{7}{2}, \frac{11}{2}, \dots \quad (2.21)$$

For an odd number particles, α can have $\alpha = +1/2$ or $-1/2$. For an even number particles, α can have $\alpha = 0$ or 1 .

A Nilsson diagram plots the energy levels for an axially symmetric quadrupole deformed potential as a function of the deformation. A similar deformed energy level diagram is shown in Fig. 2.5 which uses a deformed Woods-Saxon potential instead of

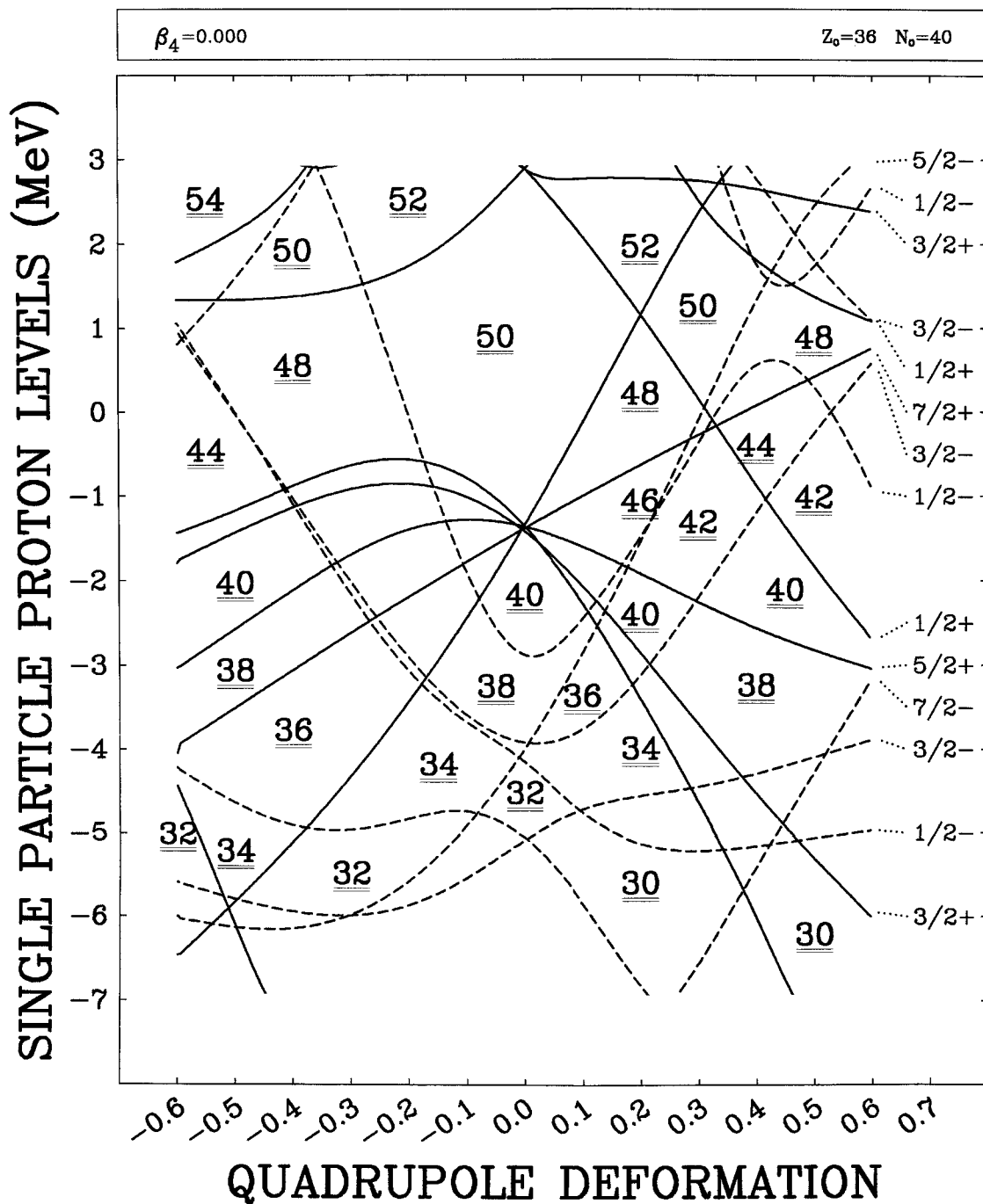


Figure 2.5: Deformed energy level diagram for a Woods-Saxon potential. Energy is indicated in units of MeV. States are labeled on the right by Ω and parity. Each state is two-fold degenerate with signature states of $\alpha = +1/2$ and $\alpha = -1/2$. Underlined numbers labeled in gaps indicate the number of states below the gap.

the modified oscillator. Because of the symmetries described above, the good quantum numbers used to describe each energy level are Ω , parity π , and signature α . In the figure, each state is labeled on the right by Ω and the parity of the state. Since the energy is not dependent on the signature, there is a two-fold degeneracy: for each energy there exists one state with $\alpha = +\frac{1}{2}$ and one state with $\alpha = -\frac{1}{2}$. To aid in counting levels, large gaps are labeled by the number of states that exist below the gap.

2.3 Collective Motion

Consider a nucleus which gains angular momentum. This can happen through two mechanisms. One is the aligning of the angular momentum from one or more single-particle orbitals. The other is the coherent motion of many nucleons, referred to as collective rotation. In order for a quantum system such as an atomic nucleus to undergo collective rotation, it must be deformed in some way, because different orientations of a spherically symmetric nucleus are indistinguishable.

A quantum mechanical rotor has energy levels with energies

$$E = \frac{\hbar^2 I(I+1)}{2\mathfrak{S}} \quad (2.22)$$

where $I(I+1)$ is the eigenvalue of the angular momentum operator squared, \vec{I}^2 , and \mathfrak{S} is the moment of inertia of the rotor. For a quantum system made up of fermions, I must take on integer (even number of fermions) or half-integer (odd number of fermions) values. Many even-even nuclei exhibit strong decay sequences that emit quadrupole radiation consistent with transitions between energy levels of the form of

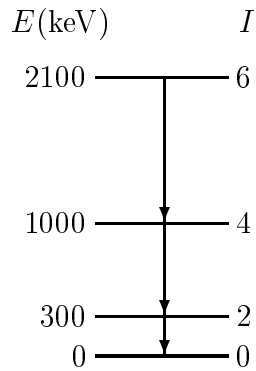


Figure 2.6: Idealized example of low spin decay sequence for an even-even nucleus. The energy of each state is labeled on the left. The spin of each state is labeled on the right. Decay transitions are indicated with arrows.

eq. (2.22) where I takes on values that differ by two. Figure 2.6 shows a schematic level scheme similar to what might be deduced from observed electromagnetic transitions. The implication of this level scheme is that the nucleus undergoes collective motion similar to a rotor. The moment of inertia can be determined from such a level scheme.

It is important to use a model that accommodates both collective and non-collective mechanisms. In slow collective rotation, where the collective motion is much slower than the motion of the constituent nucleons, the centrifugal and Coriolis forces produce only a small perturbation on the intrinsic structure. For such slow collective rotation, the motion of the constituent nucleons and the collective rotation are therefore essentially decoupled. The total angular momentum I can be thought of as the sum of a collective angular momentum R and an intrinsic angular momentum as shown in Fig. 2.7. In a quantum mechanical description, there can be no component of collective angular momentum parallel to an axis of symmetry. So for an axially symmetric nucleus, $\Omega = K$ (see Fig. 2.11).

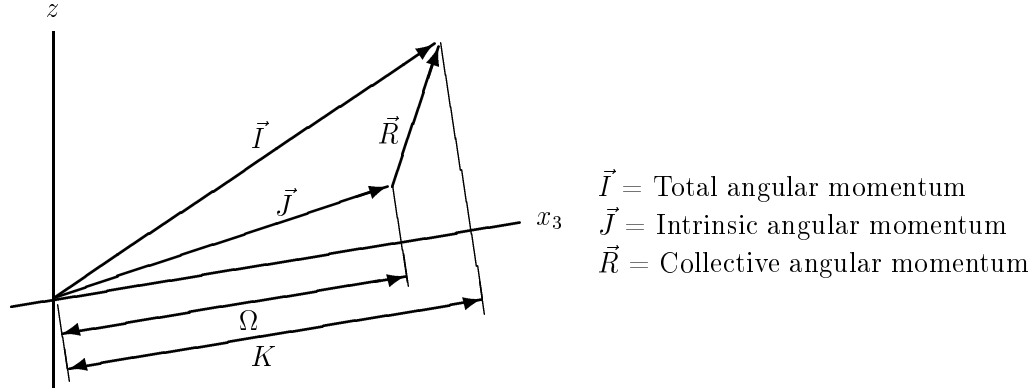


Figure 2.7: The total angular momentum \vec{I} is the sum of the intrinsic angular momentum \vec{J} and the collective angular momentum \vec{R} . For a nucleus with an axis of symmetry (here chosen as the x_3 axis), the values Ω and K are the projection onto the symmetry axis of the intrinsic and total angular momentum respectively.

2.4 Cranking Model

As the collective angular momentum increases, the centrifugal and Coriolis forces affect the intrinsic states more and more. If the angular velocity of the collective rotation is not slow compared to the motion of the nucleons, then the cranking model is needed to calculate the centrifugal and Coriolis corrections to the intrinsic Hamiltonian.

Schrödinger's equation can be expressed in terms of the intrinsic Hamiltonian and wave function by applying a time dependent rotational operator $R = e^{i(\vec{\omega} \cdot \vec{J})t/\hbar}$ to the lab frame Hamiltonian and wave function:

$$\begin{aligned}
 H_{lab} (R^{-1} R\psi_{lab}) &= i\hbar \frac{\partial (R^{-1} R\psi_{lab})}{\partial t} \\
 &= i\hbar \left[-\frac{i\vec{\omega} \cdot \vec{J}}{\hbar} R^{-1} (R\psi_{lab}) + R^{-1} \frac{\partial (R\psi_{lab})}{\partial t} \right] \\
 R H_{lab} R^{-1} R\psi_{lab} &= i\hbar R \left[-\frac{i\vec{\omega} \cdot \vec{J}}{\hbar} R^{-1} (R\psi_{lab}) + R^{-1} \frac{\partial (R\psi_{lab})}{\partial t} \right]. \quad (2.23)
 \end{aligned}$$

And since \vec{J} commutes with R ,

$$\left(RH_{lab}R^{-1}\right)(R\psi_{lab}) = \vec{\omega} \cdot \vec{J}(R\psi_{lab}) + i\hbar \frac{\partial (R\psi_{lab})}{\partial t}. \quad (2.24)$$

The Hamiltonian and wave function in the intrinsic reference frame are $H_{intr} \equiv RH_{lab}R^{-1}$ and $\psi_{intr} \equiv R\psi_{lab}$ respectively, and we have

$$\left(H_{intr} - \vec{\omega} \cdot \vec{J}\right)\psi_{intr} = i\hbar \frac{\partial \psi_{intr}}{\partial t}. \quad (2.25)$$

Eq. (2.25) leads to the expression for the cranking Hamiltonian

$$H_{\omega} = H_{intr} - \vec{\omega} \cdot \vec{J}. \quad (2.26)$$

The term $\vec{\omega} \cdot \vec{J}$ represents both the effect of the centrifugal and Coriolis interactions. This result can also be found using a classical coordinate transformation instead of the quantum mechanical approach shown above. The intrinsic Hamiltonian can be any Hamiltonian to be expressed in the rotating frame. Our calculations use the single-particle Woods-Saxon Hamiltonian to find the single-particle states in the intrinsic frame.

By convention the rotation is chosen about the x_1 -axis so that the cranking Hamiltonian is

$$H_{\omega} = H_{intr} - \omega J_1. \quad (2.27)$$

Because H_{ω} is time independent, Schrödinger's equation with the cranking Hamiltonian can be solved as an eigenvalue problem. The energy eigenvalues for the cranking Hamiltonian are the energies in the rotating frame, or the *Routhian* eigenvalues.

For comparison to experiment, it is necessary to make a rotation to the lab frame since the cranking Hamiltonian represents the energy in the nuclear body-fixed frame, whereas measurements are made in the lab frame.

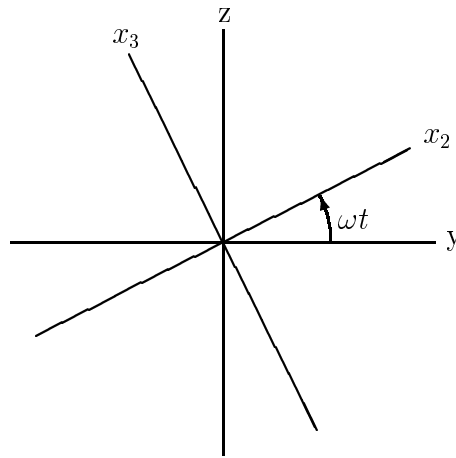


Figure 2.8: When cranking about the x_1 axis (in the figure, the x_1 axis is coming out of the page) with angular velocity ω , the lab frame x, y, z , and intrinsic frame x_1, x_2, x_3 are related as shown.

2.4.1 Cranking About the Symmetry Axis

It is straightforward to solve the Cranking Model for the case when the symmetry axis corresponds to the axis of rotation. This is because the Hamiltonian in the cranking reference frame is identical to the Hamiltonian in the lab frame. Because the Hamiltonian in the lab frame is stationary, the rotation is non-collective. Furthermore, since the Hamiltonian in the lab frame is also symmetric about the rotation axis, J_1 commutes with the Hamiltonian. Therefore, using eq. (2.27) the Routhian eigenvalues, e'_i , can be expressed in terms of the intrinsic Hamiltonian eigenvalues e_i , angular momentum projection eigenvalues Ω_i , and the cranking frequency ω by

$$e'_i = e_i - \omega\Omega_i. \quad (2.28)$$

Since Ω_i is a good quantum number (i.e. eigenvalue of J_1), the relationship between the cranking eigenvalues e'_i and the cranking frequency ω is linear with slope Ω_i (see Fig. 2.9). Note that the energy degeneracy between positive and negative values of Ω is removed when the angular velocity ω is non-zero, and that the energy levels

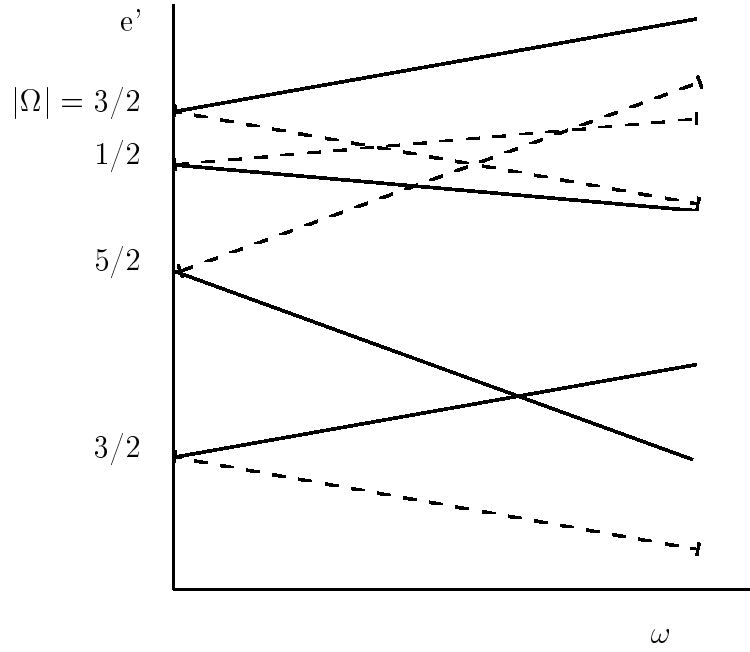


Figure 2.9: Schematic plot of single particle Routhians as a function of ω for the case of rotation around the symmetry axis.

for different spin states can cross. This removal of spin degeneracy corresponds to a removal of the signature degeneracy. The solid lines in Fig. 2.9 are $\alpha = +1/2$ and the dashed lines are $\alpha = -1/2$ states.

The total energy of the system is the sum of the energies of occupied single particle states, which can be expressed in terms of E , the eigenvalue of the intrinsic Hamiltonian, the angular frequency ω , and the total spin I_1 about the x_1 -axis:

$$E' \equiv \sum_i e'_i = \sum_i (e_i - \omega \Omega_i) = E - \omega I_1 \quad (2.29)$$

where the total spin about the x -axis is

$$I_1 = \sum_{i=1}^N \Omega_i \quad (2.30)$$

and is a constant value for a given configuration.

2.4.2 Cranking Perpendicular to the Symmetry Axis

The solution to the Cranking Model with the cranking axis perpendicular to the symmetry axis is more complicated than the previous case. The intrinsic Hamiltonian no longer commutes with J_1 , the component of the angular momentum operator in the direction of the cranking axis x_1 . Thus the eigenstates of the cranking Hamiltonian are not eigenstates of J_1 , so the set of Ω_i are no longer good quantum numbers. In fact, the only operators left that commute with both the intrinsic Hamiltonian and the angular momentum J_1 operators (and thus the total Hamiltonian), are parity (reflection about the origin) and signature (rotation about the x_1 axis by 180°).

The formula for the total energy E' of the system has the form:

$$E' = \sum_{i=1}^N e'_i = \sum_{i=1}^N (\langle e \rangle_i - \omega \langle J_1 \rangle_i) = \langle E \rangle - \omega \langle I_1 \rangle \quad (2.31)$$

where the angled brackets indicate the expectation value and $\langle e \rangle_i = e_i$, from which

$$\frac{de'_i}{d\omega} = -\langle J_1 \rangle_i \quad (2.32)$$

can be derived. The difference here from the previous section is that now $\langle J_1 \rangle_i$ is not equal to an eigenvalue of J_1 , so it varies with ω , and the slopes of the single particle Routhians are not constant.

2.5 Cranked Mean-Field Calculation with Pairing

It is necessary to correct the mean-field potential approximation for effects of the residual interaction. The most important contribution to the residual interaction

is well modeled by the pairing interaction, previously mentioned in section 2.1.1. The Hamiltonian with pairing interaction can not be diagonalized exactly, but is amenable to approximate treatment by BCS methods. This section describes the approximations made and method used to treat the pairing correlations for a cranked mean-field potential.

This method for solving the cranking Hamiltonian with pairing is applied to the following many-body Hamiltonian:

$$H = \sum_{i,j} \langle i | H_0 - \omega_x J_x | j \rangle a_i^\dagger a_j - G \sum'_{i,j} a_i^\dagger a_i^\dagger a_{\bar{j}} a_j. \quad (2.33)$$

where H_0 is the Woods-Saxon Hamiltonian in the intrinsic reference frame, and the bra and ket vectors $\langle i |, |j \rangle$ represent the basis states, which are usually chosen as the pre-calculated single-particle eigenstates of H_0 . The symbols a_i and a_i^\dagger represent the nucleon destruction and creation operators of the single-particle basis states respectively. The quantity $\langle i | H_0 - \omega_1 J_1 | j \rangle$ is the one-body matrix element of the cranked mean-field Hamiltonian. The second term in eq. (2.33) is the pairing interaction, with strength G . The two-body operator $a_i^\dagger a_i^\dagger a_{\bar{j}} a_j$ will be nonzero only when acting on states that contain both $|j \rangle$ and $|\bar{j} \rangle$ single-particle basis states. These states $|j \rangle$ and $|\bar{j} \rangle$ are the single-particle eigenstates of the intrinsic Hamiltonian which are time reverses of each other. Thus the pairing term only pairs states that are the same except for having antiparallel angular momentum. The \sum' is constrained to include only one term for each pair of time reversed basis states.

The introduction of the two-body operator renders the Hamiltonian unsolvable. We use a BCS technique which in effect uses a trial wave function

$$|\phi\rangle = \prod_i (u_i + v_i a_i^\dagger a_i^\dagger) |0\rangle \quad (2.34)$$

where u_i and v_i are constants to be determined. The occupation probability of state $|i\rangle$ is $v_i^2 = 1 - u_i^2$. The BCS state $|\phi\rangle$ does not have a definite number of particles.

The pairing interaction is simplified by applying the replacement

$$a_i^\dagger a_i^\dagger a_j a_j \longrightarrow \frac{1}{2} \langle \phi | a_j a_j | \phi \rangle (a_i^\dagger a_i^\dagger + a_i a_i). \quad (2.35)$$

The resulting Hamiltonian

$$H_{BCS} = \sum_{i,j} \langle i | H_0 - \omega_1 J_1 | j \rangle a_i^\dagger a_j - \frac{1}{2} G \sum_j \langle a_j a_j \rangle \sum_i (a_i^\dagger a_i^\dagger + a_i a_i) \quad (2.36)$$

can be diagonalized by introducing quasiparticles via a Bogoliubov transformation. Its ground state $|\phi\rangle$ is the quasiparticle vacuum. Like every BCS state vector, $|\phi\rangle$ corresponds to an indefinite number of particles. This is reasonable, because the particle number operator N does not commute with the operator $\sum_{i<} (a_i^\dagger a_i^\dagger + a_i a_i)$ in eq. (2.36). We ensure that $|\phi\rangle$ has the correct average number of particles by introducing a Lagrange multiplier λ , and replacing the Hamiltonian H with $H - \lambda N$. The optimal values of u_i and v_i , and hence $|\phi\rangle$, depend on λ . Solutions are then found such that the expectation value $\langle \phi | N | \phi \rangle$ is equal to the actual number of particles in the system. This involves iterative adjustment of λ , which can then be identified as the Fermi energy of the system. Since the Schrödinger equation also contains the quantity $\Delta = \sum_j \langle \phi | a_j a_j | \phi \rangle$ which depends on the unknown state $|\phi\rangle$, an initial value of Δ is estimated and the value of Δ is adjusted along with λ during each iteration.

2.6 Strutinsky Shell Correction

The liquid drop model and the shell model provide two different values for the energy of a nucleus. The method of Strutinsky shell correction is to reconcile these two models by expressing the nuclear energy E_{tot} as the sum of a liquid drop model part E_{LD} and a shell correction part E_{sh}

$$E_{tot} = E_{LD} + E_{sh}. \quad (2.37)$$

The shell model accurately describes the small fluctuations of the nuclear energy with respect to neutron and proton numbers N and Z . So E_{sh} is derived from the shell model energy with a smooth part subtracted so that E_{sh} averages to zero over a range of atomic mass number. It is appropriate to choose E_{LD} as the liquid drop model because it accurately describes the trend of the nuclear energy with atomic mass numbers N and Z . The resulting E_{tot} is then the sum of a smooth part E_{LD} and a fluctuating part E_{sh} .

We use Nilsson and Ragnarsson's method [2] to obtain E_{sh} . It is found from the sum of a proton shell energy $E_{sh}(\text{prot})$ and a neutron shell energy $E_{sh}(\text{neutr})$. Both $E_{sh}(\text{prot})$ and $E_{sh}(\text{neutr})$ are similarly found from the shell energy minus a smoothed part. Figure 2.10 shows a plot of $e_{\text{stair}}(N)$, the shell model single-particle energy levels of neutrons in a spherical Woods-Saxon potential appropriate for $N = 126$ and $Z = 82$, and $\bar{e}(N)$, the corresponding smoothed part. The neutron shell part for ^{208}Pb is then

$$E_{sh}(\text{neutr}) = \sum_{N=1}^{126} e_{\text{stair}}(N) - \int_0^{126} \bar{e}(N) dN. \quad (2.38)$$

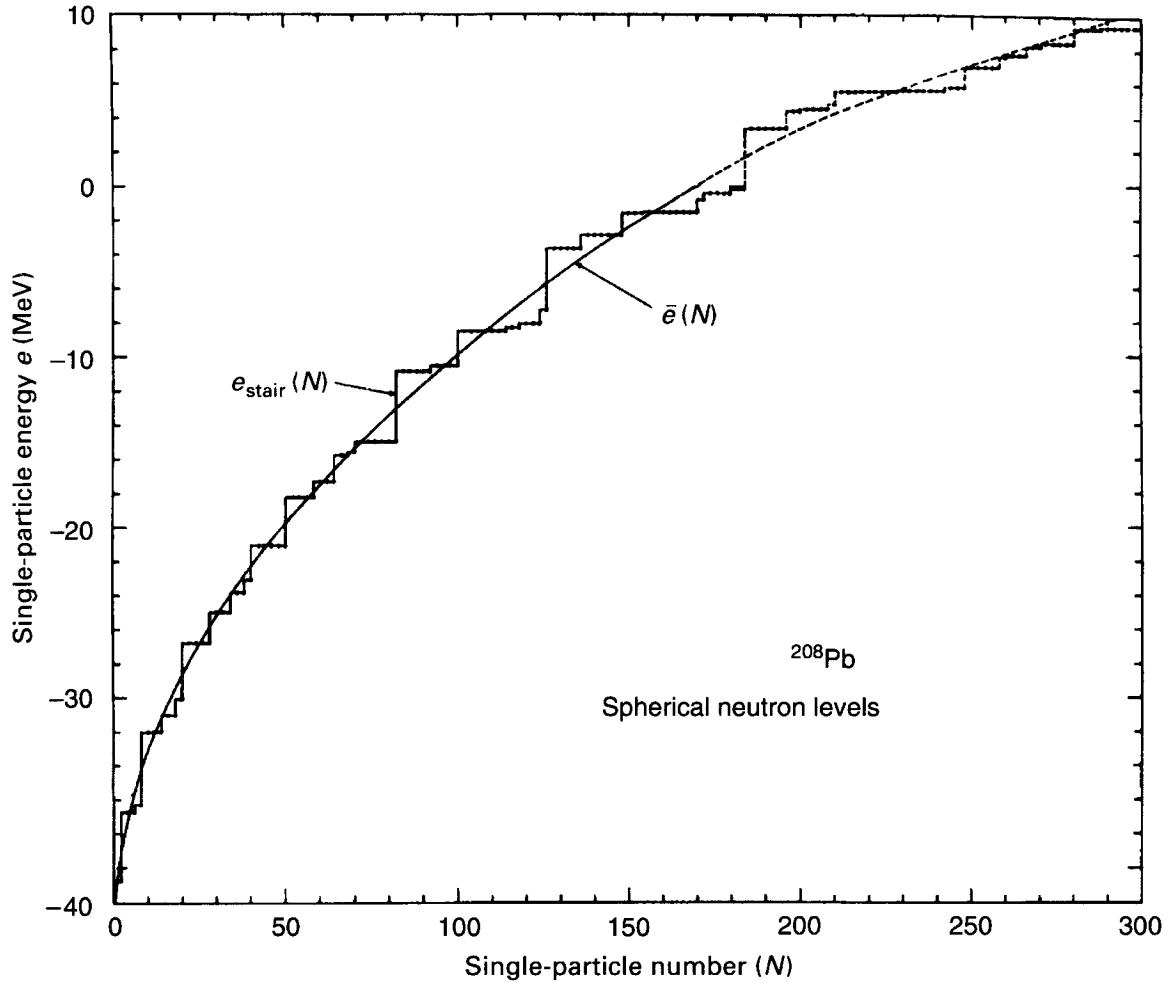


Figure 2.10: Example of smoothed energy levels used for Strutinsky smoothing. Single particle energy levels for a spherical ^{208}Pb nucleus $e_{stair}(N)$ are shown with dots and lines connecting the dots in a staircase pattern. The corresponding smoothed energy level function $\bar{e}(N)$ is also shown.

For an additional neutron, the single-particle states will not change significantly, but the addition of the 127th neutron just above the shell will increase the energy more than the smooth part. So $E_{sh}(\text{neutr})$ will retain the desired shell fluctuations, but averages to zero over N

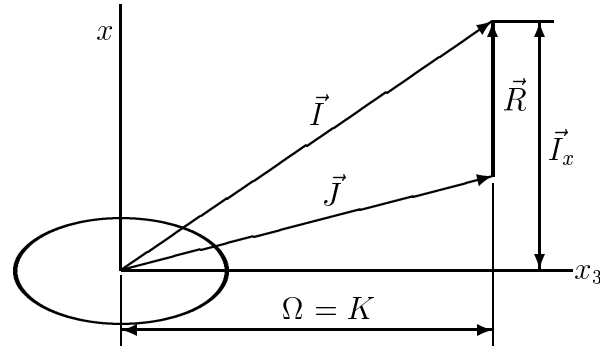


Figure 2.11: Components of the angular momentum shown for the case of rotation about the x axis, where the x axis is perpendicular to the symmetry or x_3 axis.

2.7 Comparing Theory to Experiment

It has become usual to compare theory to experiment at the level of the Routhian to get information about configurations, angular momentum, etc.

Classically, one can consider a model of a rotor free to rotate with any one of its principal axes aligned along the space fixed x axis, such as is shown in Fig. 2.11. It will have a Hamiltonian $H = H(I_x)$ where I_x is the canonical momentum conjugate to the angle of rotation ϕ . So Hamilton's equations of motion are:

$$\dot{\phi} = \frac{\partial H}{\partial I_x} = \frac{dE}{dI_x}, \quad \dot{I}_x = -\frac{\partial H}{\partial \phi} = 0. \quad (2.39)$$

The first of these gives

$$\omega = \frac{dE}{dI_x} \quad (2.40)$$

which also makes sense in quantum mechanics and enables us to define the angular velocity ω .

Since the angular momentum I is measured, but I_x (the component of the angular momentum along the cranking axis) will relate most quantities, we relate I

and I_x with:

$$I_x(I) = \sqrt{(I + 1/2)^2 - K^2} \quad (2.41)$$

where K is the angular momentum perpendicular to the cranking axis. This is similar to $I^2 = I_x^2 + K^2$ for the addition of perpendicular vectors with the eigenvalue for the operator \vec{I}^2 being $I(I + 1)$, but eq. (2.41) is traditional. So the angular velocity can be expressed as

$$\omega(I) = \frac{dE(I)}{dI_x(I)} \approx \frac{E(I + 1) - E(I - 1)}{I_x(I + 1) - I_x(I - 1)}. \quad (2.42)$$

The static and dynamic moments of inertia denoted by $\mathfrak{S}^{(1)}$ and $\mathfrak{S}^{(2)}$ respectively are

$$\mathfrak{S}^{(1)}(I) = \frac{I_x(I)}{\omega(I)} \quad (2.43)$$

and

$$\mathfrak{S}^{(2)}(I) = \frac{dI_x(I)}{d\omega(I)} \approx \frac{I_x(I + 1) - I_x(I - 1)}{\omega(I + 1) - \omega(I - 1)} \quad (2.44)$$

From the cranking Hamiltonian $H' = H - \omega J_x$, the total Routhian is given by

$$E'(I) = E(I) - \omega(I)I_x(I) \approx \frac{1}{2} [E(I + 1) + E(I - 1)] - \omega(I)I_x(I). \quad (2.45)$$

When investigating small effects in the energy or spin, it is convenient to subtract out the larger effect of the rotor. One way to subtract the rotor effect is by using the Harris formula $\mathfrak{S} = J_0 + J_1\omega^2$ with parameters J_0 and J_1 [6]. Values for J_0 and J_1 can be chosen based on the ground state band of the nucleus under study, or can be adopted from another nucleus for comparison. A good reference nucleus would be the nearest even-even nucleus with fewer or equal N and Z to the nucleus under study because it is less likely to show strong single-particle effects.

The reference energy and reference angular momentum are defined by

$$E^{reference}(\omega) = \frac{-\omega^2}{2}J_0 - \frac{\omega^4}{4}J_1 + \frac{\hbar^2}{8J_0}, \text{ and} \quad (2.46)$$

$$I_x^{reference} = \omega J_0 + \omega^3 J_1. \quad (2.47)$$

These reference values for energy and spin describe the collective, rotor-like motion.

By subtracting this reference as follows

$$e'(\omega) = E'(\omega) - E^{reference}(\omega) \quad (2.48)$$

and

$$i(\omega) = I_x(\omega) - I_x^{reference}(\omega), \quad (2.49)$$

the remaining structure shows the single particle shell effects that can be seen from the experimental data. For this reason e' is referred to as the quasiparticle energy and $i(\omega)$ is referred to as the aligned spin.

This provides a method for finding I_x , $\mathfrak{S}^{(1)}$, $\mathfrak{S}^{(2)}$, e' , and i from experiment and comparing to quantities in the cranking model. From these results, conclusions can be drawn about the configuration and parameters of the nucleus.

Chapter 3

EXPERIMENT AND ANALYSIS METHODS

Three similar experiments were performed. This chapter will describe the apparatus and analysis methods used. The specifics that differ in each of these experiments will be discussed in the next chapter prior to the discussion of the results from each experiment.

The experiments all used the fusion-evaporation reaction to obtain highly-excited, high-spin states in a nuclei. The Gammasphere [7] and Microball [8] detector arrays were used to detect γ rays and evaporated charged particles. Data was stored event by event on magnetic tape and sorted for later interpretation.

3.1 Population of High Spin Nuclear States

High-spin states ($I \approx 15\hbar$ to $70\hbar$) in a nucleus can be obtained through fusion-evaporation experiments. In each of our experiments, a target nucleus of mass $\approx 60u$ and $Z \approx 28$ is bombarded with a projectile nucleus of mass $\approx 30u$ and $Z \approx 15$ at an energy sufficient to overcome the Coulomb barrier. The two nuclei may fuse to

form a highly excited compound nucleus at high spin. The compound nucleus then decays by particle evaporation and γ ray emission.

The cross-section for particle evaporation is much larger than for γ ray emission, so in the first stages of de-excitation particle evaporation dominates [9]. Typically, each nucleon takes away $1\hbar$ to $2\hbar$ of angular momentum and about 8 MeV of energy from the compound nucleus. The nucleus then decays by γ ray emission. The example in Fig. 3.1 [10] contains schematic plots describing a fusion-evaporation experiment that uses a ^{40}Ar projectile nucleus on a ^{124}Sn target nucleus at a beam energy of 147 MeV. The middle plot shows the energy vs. angular momentum of the system for one to five evaporated neutrons: n, 2n, 3n, 4n, 5n. The “yrast” line indicated in Fig. 3.1 represents the lowest possible energy for the system at a given spin. The figure shows intensity profiles for the entry populations of the 3n, 4n, and 5n channels, and the expected input angular momentum for this experiment. The shaded areas show where the system does not have enough energy, as a function of angular momentum, to support particle evaporation. Further particle evaporation can occur if the energy and angular momentum are outside of the shaded region in Fig. 3.1. In this example, after three neutrons are evaporated the system can be sufficiently near the yrast line that further particle evaporation is excluded.

3.2 Gammasphere Detector Array at LBNL

Gammasphere is a spectrometer designed to detect γ rays with high energy resolution and high efficiency [7]. Gammasphere has the capacity to hold 110 high-

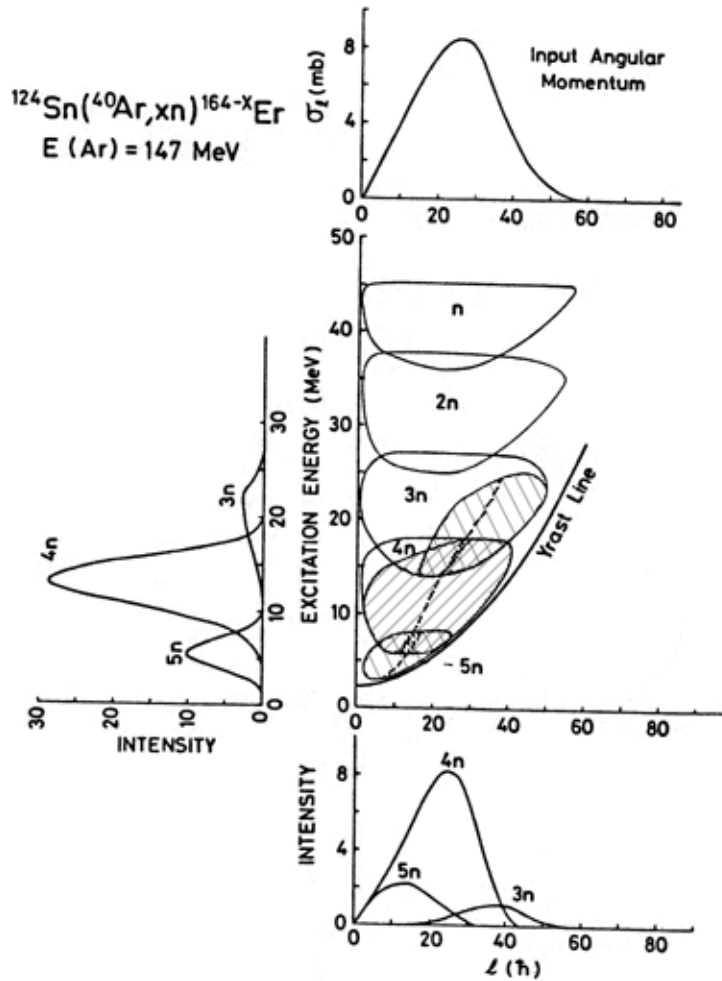


Figure 3.1: A schematic diagram showing the decay of a compound nucleus from the reaction $^{124}\text{Sn}(^{40}\text{Ar}, xn)^{164-x}\text{Er}$ with a beam energy of 147 MeV. The middle plot shows the energy vs. angular momentum of the system. Below and to the left are intensity profiles for the entry populations of the 3n, 4n, and 5n channels. The top plot shows the expected input angular momentum for this experiment [10].

purity germanium detectors, each enclosed in a bismuth-germinate (BGO) Compton-suppression shield. Compton suppression is discussed in more detail in the following subsection.

At the time of our experiments, Gammasphere was located at the 88-Inch Cyclotron of the Lawrence Berkeley National Laboratory's Nuclear Science Division. This cyclotron is a low-energy accelerator capable of providing the beams of $^{28,29}\text{Si}$, and ^{30}P at beam energies of about 130 MeV which were used in our experiments.

3.2.1 Compton-suppressed germanium detectors

Detectors that provide the best efficiency and resolution for γ rays in the MeV energy range are made using high-purity germanium crystals. The largest such crystals that can currently be produced commercially are cylinders of about 10 cm in diameter and 10 cm long [11]. For about 30% of incident 1 MeV γ rays, these detectors produce a signal with a full-energy peak with a full width at half of the maximum height of about 2 keV. For γ rays of 1 MeV energy, about three out of four γ rays are Compton scattered from the germanium crystal without depositing all of their energy. This leads to a continuum background of partial-energy signals. For a better ratio of full-energy to partial-energy events (called the peak-to-total or P/T ratio), the Ge detectors are surrounded by a high density scintillator (BGO being the most common) that detects γ rays which are Compton scattered out of the germanium crystal. When the BGO scintillator makes such a detection, the Ge detector signal is suppressed. This results in an improvement in the P/T ratio for a 1 MeV γ ray from about 0.25 for the bare Ge crystal to about 0.6 when this suppression

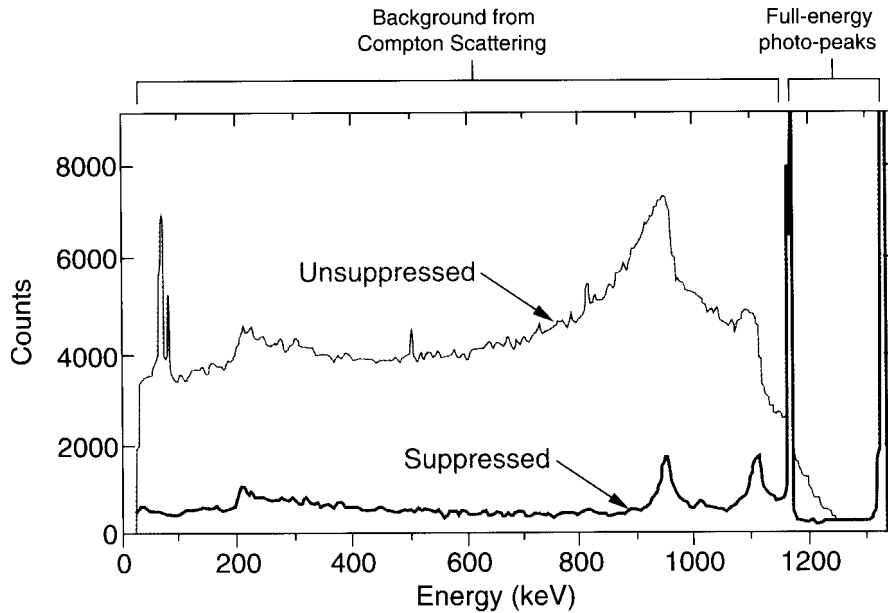


Figure 3.2: Two sample spectra demonstrating the affect of Compton suppression. The spectra contain two peaks with tails due to Compton scattering. The Compton suppressed spectrum has peak to total ratio much higher than the unsuppressed spectrum.

scheme is used. Figure 3.2 shows two ^{60}Co spectra that are identical except one has Compton suppression and one does not. Coincidence analysis, which is discussed in section 3.4.2, would be practically impossible without Compton suppression because of the large Compton-background.

3.3 Microball Detector Array

Microball [8], which was designed at Washington University in St. Louis, detects light, charged particles ($^1,^2,^3\text{H}$, and $^3,^4\text{He}$) emitted in the reaction process. It fits inside Gammasphere and consists of 95 CsI(Tl) scintillators closely packed to cover 97% of the full 4π steradians.

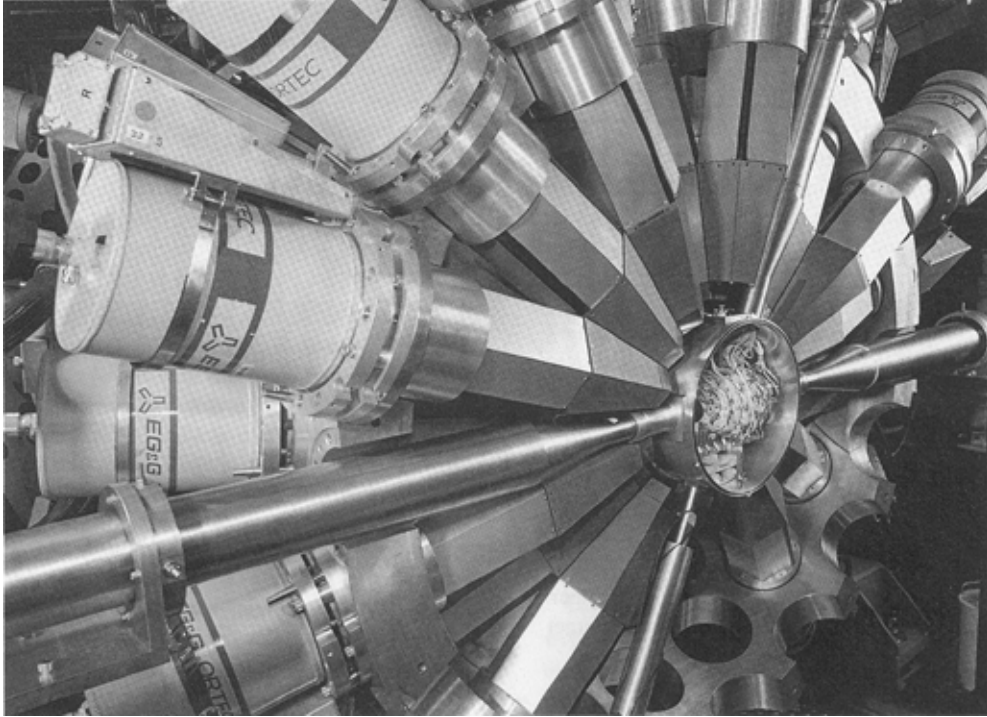


Figure 3.3: Picture of Microball placed inside of one hemisphere of Gammasphere.

The resolving power of Gammasphere is enormously improved by the capability of Microball to select specific charged-particle evaporation channels from among a large number of reaction products. It also measures the energies of light charged particles which allows Doppler shift corrections to be done on an event-by-event basis. Such corrections are described in section 3.4.1 and can improve the energy resolution of γ rays by factors of up to three. For more information on the design of Microball and its use in particle identification see reference [8]. Figure 3.3 shows a picture of Microball placed inside Gammasphere. One of Gammasphere's hemispheres can be seen, and the cover to Microball has been removed.

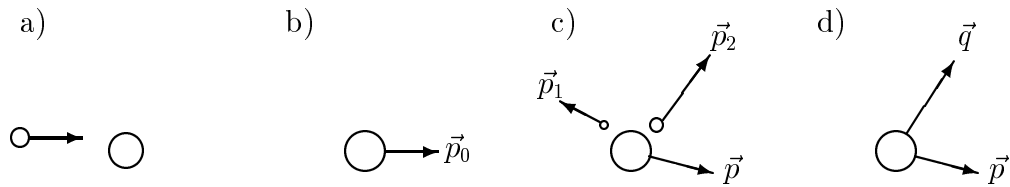


Figure 3.4: Diagram of the kinematics in a beam on target experiment: a) A projectile nucleus is incident on a target nucleus; b) The projectile and target nuclei fuse together to form a compound nucleus; c) The compound nucleus evaporates neutrons, protons, and/or α particles; d) The product nucleus decays through electromagnetic emission (\vec{q} being the momentum of the γ ray).

3.4 Data Analysis

3.4.1 Kinematics

A correction to the energy of each γ ray detected by a high-purity germanium detector during an experiment can be made with a detailed kinematic calculation. Figure 3.4 shows the momenta of the various particles involved during the reaction: a) a projectile is incident upon a target nucleus; b) the projectile and target fuse to form a compound nucleus; c) the compound nucleus decays by evaporating protons, neutrons, and α particles; d) the product nucleus further decays through the emission of γ ray radiation. The recoil of the product nucleus due to the emission of γ rays is very small and hence neglected. Since we are investigating the nucleus, we are interested in the energy of the γ rays in the rest frame of the product nucleus. So the energy measured by the detectors will be Doppler shifted as a result of the velocity of the product nucleus. Hence in the analysis, the measured γ ray energies need to be Doppler corrected.

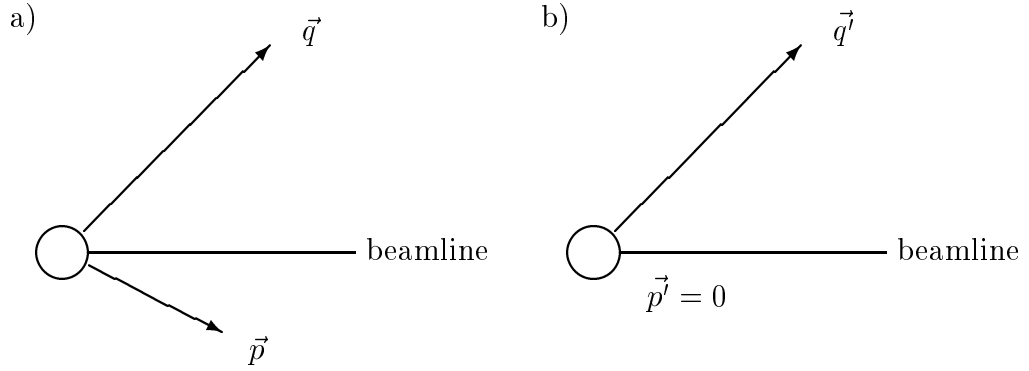


Figure 3.5: Emission of a γ ray in the a) lab frame and b) nuclear rest frame.

In our experiments, energies are low enough that particles with mass are not relativistic. Since momentum is conserved:

$$\vec{p} = \vec{p}_0 - \sum_i \vec{p}_i \quad (3.1)$$

where \vec{p} is the momentum of the product nucleus, \vec{p}_0 is the momentum of the compound nucleus, and \vec{p}_i is the momentum of each evaporated particle.

To obtain the Doppler correction for the emitted γ ray, consider the emission of a γ ray in the lab frame and the product nucleus rest frame shown in Fig. 3.5 where \vec{q} and \vec{p} are the momenta of the γ ray and the product nucleus. The primed system represents the rest frame of the product nucleus, which is about to emit the γ ray, and the un-primed system represents the lab frame. Using notation consistent with Jackson [12]: m is the rest mass of the product nucleus, the covariant momentum 4-vector of the γ ray is $q_\alpha = (E_\gamma/c, -\vec{q})$, and the contravariant momentum 4-vector of the product nucleus is $p^\alpha = (\gamma mc, \vec{p})$ where $\gamma = (1 - v^2/c^2)^{-1/2}$ is the relativistic coefficient. The invariant scalar product gives

$$q'_\alpha \cdot p'^\alpha = q_\alpha \cdot p^\alpha$$

$$(E'_\gamma/c)(\gamma' mc) - \vec{q}' \cdot \vec{p}' = (E_\gamma/c)(\gamma mc) - \vec{q} \cdot \vec{p}.$$

The primed system is in the rest frame of the product nucleus, so $\vec{p}' = 0$, and $\gamma' = 1$, so

$$(E'_\gamma)m = (E_\gamma)\gamma m - \vec{q} \cdot \vec{p}. \quad (3.2)$$

Relating $\vec{q} = (E_\gamma/c)\hat{q}$ and $\vec{p} = (\gamma mv)\hat{p}$

$$(E'_\gamma)m = (E_\gamma)\gamma m - (E_\gamma/c)(\gamma mv)\hat{q} \cdot \hat{p}$$

$$E'_\gamma = E_\gamma \gamma \left(1 - \frac{v}{c} \cos \theta\right) \quad (3.3)$$

which is a well known result. From the data, it is more convenient to calculate the vectors \vec{q} and \vec{p} in cartesian coordinates and use eq. (3.2) than to calculate θ , the angle between \vec{q} and \vec{p} . The vector \vec{q} can be found from the position of the detector and the energy of the γ ray. The energy and angle of each detected charged particle can be used to find the momentum of each charged particle non-relativistically. These momenta can then be applied to eq. (3.1) to obtain \vec{p} .

3.4.2 Coincidence Analysis

A nucleus can decay from one state to another state through many different intermediate states. Deducing the energy levels of a nucleus from all transitions in a single γ ray energy spectrum is in practice impossible. Because of the multiple detectors in Gammasphere, it is possible to detect multiple γ rays occurring within

a time interval consistent with a single nuclear decay. For our purposes, such γ rays are considered to occur in coincidence. By isolating the transitions that occur in coincidence, each decay sequence can be determined and fit together with all other decay sequences to form a complete energy level diagram.

It is convenient to store coincidence spectra in a two dimensional matrix called a coincidence matrix with elements M_{ij} . Consider an event with three detected γ rays: $\{\gamma_1, \gamma_2, \gamma_3\}$ of energies $\{E_{\gamma_1}, E_{\gamma_2}, E_{\gamma_3}\}$. The coincidence matrix is built by incrementing all elements in the matrix with coordinates equal to the permutations of the energies of each γ ray: $(E_{\gamma_1}, E_{\gamma_2}), (E_{\gamma_2}, E_{\gamma_3}), (E_{\gamma_1}, E_{\gamma_3}), (E_{\gamma_2}, E_{\gamma_1}), (E_{\gamma_3}, E_{\gamma_2}), (E_{\gamma_3}, E_{\gamma_1})$. Consider now the column vector at the coordinate E_{γ_1} . The column vector contains a spectrum with counts at E_{γ_2} and E_{γ_3} . If such an incrementation is performed for all events, the column at E_{γ_1} will contain a complete spectrum of all transitions that occur in coincidence with all γ rays of energy E_{γ_1} . Similarly, each column of the matrix contains a complete spectra of γ rays that occur in coincidence with a γ ray of energy equal to the coordinate of that column. Selecting a column spectrum is referred to as gating. Since γ ray peaks have some finite width, gating on a γ ray involves adding the column vectors at the coordinates that lie within the energy range of the γ ray's full width at half of the maximum. Note that due to the incrementation process, a coincidence matrix is always symmetric, so gating on rows or columns gives the same result. Similar to a coincidence matrix, a symmetric cube can be created to select spectra in coincidence with *two* other γ rays called an E_{γ_1} - E_{γ_2} - E_{γ_3} coincidence cube. Selecting a column spectra from such a cube is referred to as double gating.

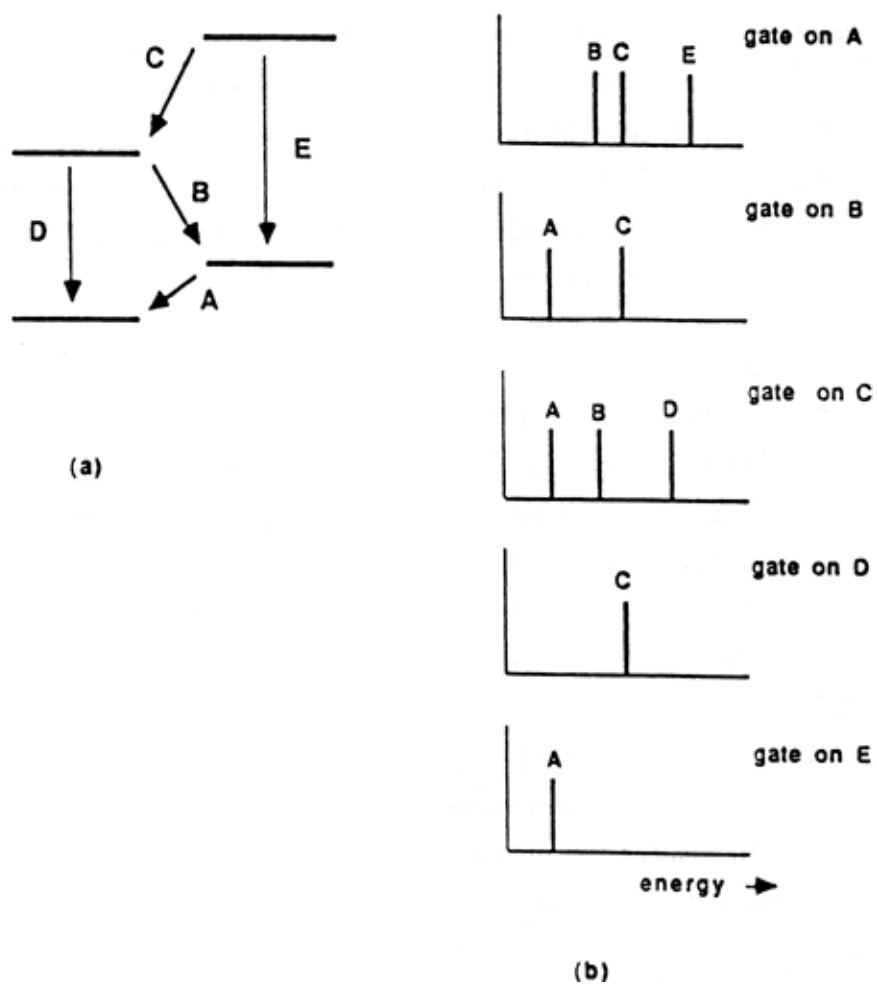


Figure 3.6: Schematic of the gates of a coincidence matrix from a sample level scheme.[13] (a) The sample level structure. (b) Spectra that result from various gates.

Figure 3.6 shows a schematic of the gates from a coincidence matrix for a sample level scheme. The sample level scheme is shown in a), and the ideal spectra resulting from gates are shown in b). Each gate results in a spectrum that contains counts at energies equal to the transitions that can occur in the same decay path as the transition of energy equal to the gating energy. Note that the transition of energy equal to the gating energy is not in the spectrum. One benefit of this is that it is possible to see if two transitions of equal energy occur in the same decay sequence.

3.4.3 Background Subtraction

In an ideal experiment each event contains only γ rays from a given decay sequence. In a realistic experiment, there will also be γ rays detected from unwanted sources. Compton scattering is the primary source of unwanted γ rays. Other unwanted sources include background radiation unconnected to the experiment, giant magnetic dipole resonance, and electron-positron annihilation. Each unwanted γ ray in an event will lead to multiple unwanted counts in the coincidence matrix because of the incrementation process described in section 3.4.2. Unwanted counts which have equal probability to occur in coincidence with each wanted event can be removed from the matrix with some statistical background subtraction techniques. Radford presented a method to do background subtraction [14] based on Palameta and Waddington's method [15]. This method uses the total projection of the matrix onto its axis

$$P_i \equiv \sum_j M_{ij}, \quad (3.4)$$

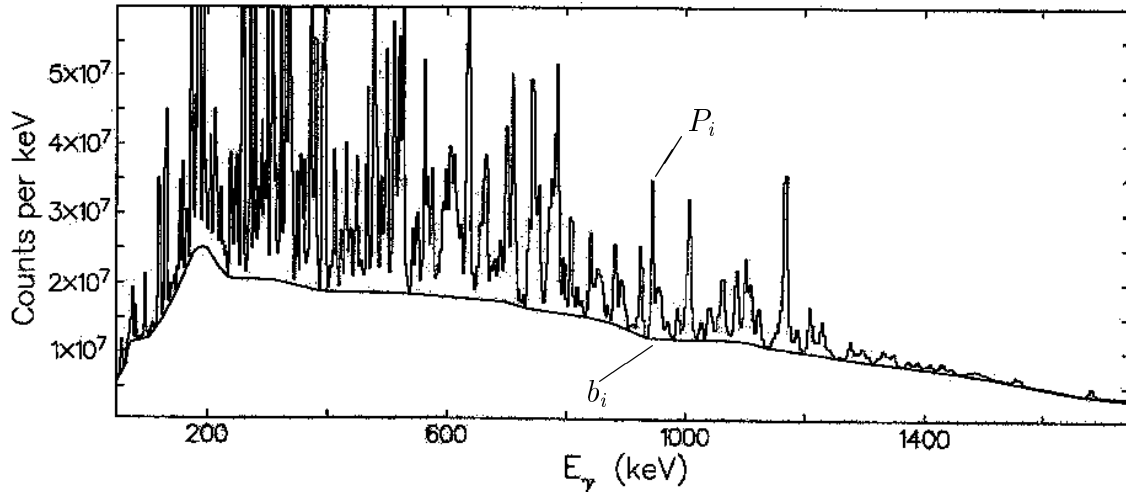


Figure 3.7: A sample plot of the total projection of a coincidence matrix. At $i = 930$ keV, $P_i \approx 3.5 \times 10^7$ counts and the estimated background $b_i \approx 1.3 \times 10^7$ counts.

where M_{ij} represents the coincidence matrix elements described in the previous section, and splits P_i into a peak spectrum p_i and a background spectrum b_i . See Fig. 3.7 for a pictorial description of the total projection and background spectra. The peak spectrum is

$$p_i = P_i - b_i. \quad (3.5)$$

The choice of how many counts in a channel are peak or background counts is estimated by eye, and does influence the quality of the background subtraction to a small degree. The background matrix B_{ij} which is subtracted from the coincidence matrix M_{ij} is then:

$$B_{ij} = \frac{1}{T}(P_i P_j - p_i p_j) \quad (3.6)$$

where T is the total number of counts in the original matrix. Radford also generalizes this method for many-fold coincidences such as coincidence cubes (3-fold) [14].

λ	1	2	3	4	...
$\pi_i = \pi_f$	<i>M1</i>	<i>E2</i>	<i>M3</i>	<i>E4</i>	...
$\pi_i = -\pi_f$	<i>E1</i>	<i>M2</i>	<i>E3</i>	<i>M4</i>	...

Table 3.1: Selection rules tabulated by the angular momentum and parity of the γ ray.

3.4.4 Gamma Decay and Gamma Angular Distributions

The γ ray decay of the excited nucleus must satisfy certain selection rules. Consider the decay between two states of spin and parities $I_i(\pi_i)$ and $I_f(\pi_f)$ and let λ be the angular momentum carried away by the emitted γ ray. Angular momentum conservation then requires that

$$|I_f - I_i| \leq \lambda \leq I_i + I_f. \quad (3.7)$$

The emitted radiation can then be of either electric or magnetic or mixed multipole character depending on whether $\pi_i = \pi_f$ or $\pi_i = -\pi_f$. This is summarized in Table 3.1, where M_i and E_i refer to magnetic and electric multipole radiation. In experiments of the type discussed here, the only transitions of importance are of electric and magnetic dipole ($E1$, $M1$) and electric quadrupole ($E2$) character. It should also be noted that typically, electric transitions dominate over magnetic transitions of the same λ . Of particular interest are transitions of mixed multipolarity. Consider the decay between the two states indicated in Fig. 3.8. Selection-rules tell us that the lowest two multiplicities for this decay are $M1$ and $E2$. Thus, the decay may be of mixed character. It is customary [16] to define the mixing ratio δ as the ratio between the two transition amplitudes $A(E2)$ and $A(M1)$

$$\delta = \frac{A(E2)}{A(M1)}. \quad (3.8)$$

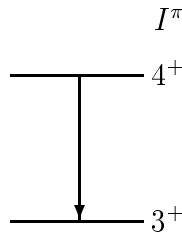


Figure 3.8: Decay from a spin and parity $I^\pi = 4^+$ state into a $I^\pi = 3^+$ state.

The transition amplitudes can be expressed in terms of $E2$ and $M1$ matrix-elements $\langle f||E\lambda||i\rangle$ and $\langle f||M\lambda||i\rangle$:

$$A(E\lambda) = \left[\frac{8\pi(\lambda+1)e^2b^\lambda}{\lambda[(2\lambda+1)!!]^2\hbar} \left(\frac{E_\gamma}{\hbar c} \right)^{2\lambda+1} \left(\frac{1}{2I_i+1} \right) \right]^{1/2} \langle f||E\lambda||i\rangle \quad (3.9)$$

for $\lambda = 2$ and

$$A(M\lambda) = \left[\frac{8\pi(\lambda+1)\mu_N^2b^{\lambda-1}}{\lambda[(2\lambda+1)!!]^2\hbar} \left(\frac{E_\gamma}{\hbar c} \right)^{2\lambda+1} \left(\frac{1}{2I_i+1} \right) \right]^{1/2} \langle f||M\lambda||i\rangle \quad (3.10)$$

for $\lambda = 1$. In the above equations, $e^2 = 1.440 \times 10^{-10}$ keV cm, $\mu_N^2 = 1.5922 \times 10^{-38}$ keV cm³, and $b = 10^{-24}$ cm².

By observing the angular distributions of emitted γ rays, the angular momentum λ carried away from the compound nucleus can be determined. However, it is not possible to distinguish between electric and magnetic transitions. A general analysis of angular distributions was done by Rose and Brink [17] and Vaillancourt and Taras [18]. A more specific analysis for γ rays following fusion-evaporation reactions was made by Mateosian and Sunyar [19], and Taras and Haas [20]. The results of these works show that angular distributions are dependent on the angular momentum removed from the nucleus and the emitted γ ray.

The angular distribution $W(\theta)$ can be represented by a Legendre polynomial series:

$$W(\theta) = \sum_k a_k P_k(\cos \theta) \quad (3.11)$$

where the intensity is normalized such that $a_0 = 1$. Theoretical values for a_k are plotted in Taras and Haas [20] as a function of the mixing ratio for $k = 2, 4, 6$ and for a change in the angular momentum of the nucleus from a gain of $2\hbar$ to a loss of $2\hbar$. Coefficients of a_k with odd k do not occur because of symmetry considerations. Figure 3.9 and 3.10 show the theoretical plots for angular momentum loss of $2\hbar$ ($J \rightarrow J - 2$) and $1\hbar$ ($J \rightarrow J - 1$) as a function of the mixing ratio. Solid and dashed lines represent angular distribution coefficients for two initial states of specific angular momentum. These two lines illustrate the variance that the angular distribution coefficients have on the initial spin.

There is some overlap in the angular distribution coefficients for certain combinations of angular momenta and mixing ratios, but such ambiguities can often be resolved by considering level scheme, selection rules, and intensity probabilities. Since the nucleus starts from a high spin state and ends in a low spin state, angular momentum loss is much more frequent than angular momentum gain. If the system loses $2\hbar$ of angular momentum with an observed γ ray, that γ ray is almost certainly a pure $E2$ transition. This is because $E3$, $M2$, and larger order multipolarities are too weak to be observed, and $E1$ and $M1$ transitions cannot carry the $2\hbar$ of angular momentum that is lost from the nucleus. Such a pure $E2$ transition is called a “stretched” $E2$ transition. The coefficients of the stretched $E2$ transition can be read from Fig. 3.9 as $a_2 = 0.4$, $a_4 \approx -0.18$, and $a_6 = 0.0$. Since a loss in angular momentum

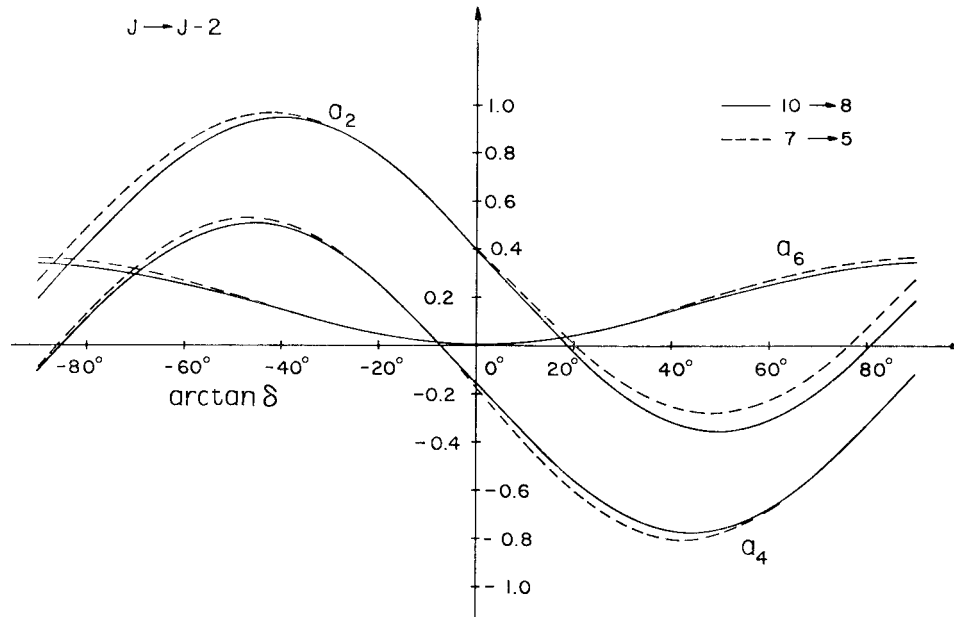


Figure 3.9: Plot of a_k for a change in angular momentum of $2\hbar$ ($J \rightarrow J - 2$). The solid line is calculated for an initial angular momentum of $10\hbar$ and final angular momentum of $8\hbar$. The dashed line is calculated for an initial angular momentum of $7\hbar$ and final angular momentum of $5\hbar$. Mixing ratio δ is the ratio of octupole to quadrupole transition strengths.

of $1\hbar$ does not have a negative value for a_4 (from Fig. 3.10), transitions that carry $2\hbar$ of angular momentum from the nucleus are distinguishable from transitions that carry $1\hbar$ of angular momentum. Where possible, it is assumed that transitions remove some angular momentum from the nucleus; but transitions that do not change or that increase the angular momentum of the nucleus can still occur. The majority of the angular distribution analysis focuses on determining if a transition is a stretched $E2$, a pure $E1$ or $M1$, or the mixing ratio for an $E2/M1$ transition. Pure $E1$ and pure $M1$ transitions are not distinguishable from angular distributions.

To create an angular distribution for a transition, the intensity of the corresponding γ ray at each angle is measured by summing the total number of counts in the peak at the transition energy for all detectors at a given angle. For an angle

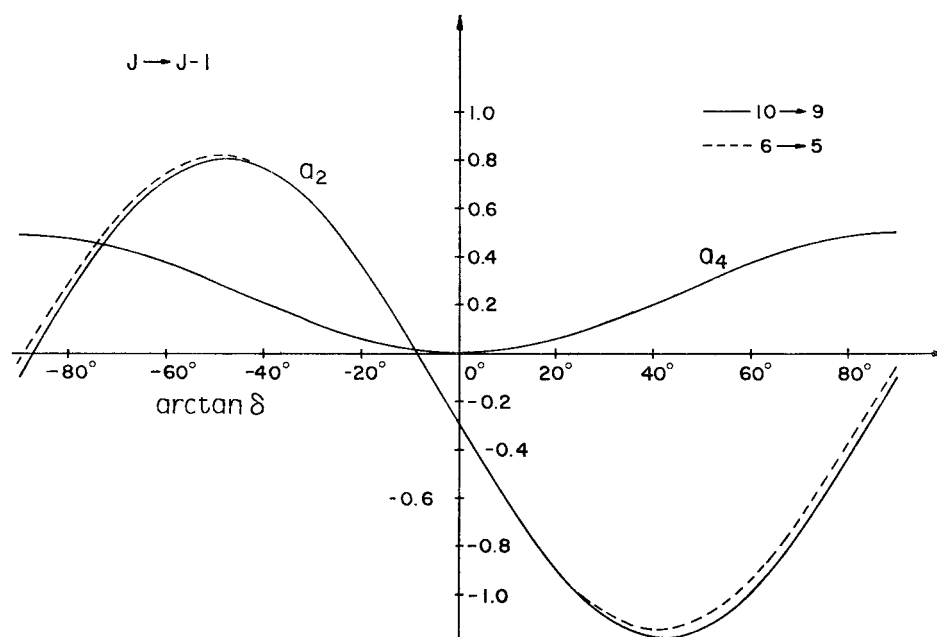


Figure 3.10: Plot of a_k for a change in angular momentum of $1\hbar$ ($J \rightarrow J - 1$). The solid line is calculated for an initial angular momentum of $10\hbar$ and final angular momentum of $9\hbar$. The dashed line is calculated for an initial angular momentum of $6\hbar$ and final angular momentum of $5\hbar$. Mixing ratio δ is the ratio of dipole to quadrupole transition strengths.

measured between the beamline and a detector, with the target being at the vertex, Gammasphere has slots for detectors positioned in rings at 17 different angles, making it possible to plot 17 points on an angular distribution plot. But since there are a different number of detectors in each ring, and each detector has a different efficiency, the number of counts measured for any given angle needs to be corrected. It is convenient and effective to measure the efficiency of each ring of detectors with a static calibration source, which emits radiation isotropically. However, during the experiment, absorption due to the target frame may lead to a slight shift in the effective efficiency of each ring, so the efficiency of each ring is corrected to known transitions in the nucleus under study.

Chapter 4

RESULTS AND DISCUSSION

The previous chapter described general methods applied to the three experiments performed. This chapter presents the specifics of each experiment followed by a discussion. Two isotopes were studied. This chapter is split into two sections, one for ^{80}Sr and one for ^{85}Y . Two experiments performed provided data on ^{80}Sr , one provided data for ^{85}Y . These isotopes are not specifically related to each other except that they both have a mass of about 80u, so both isotopes occupy single-particle states up to the $g_{9/2}$ subshell.

4.1 Strontium 80

4.1.1 Experimental Specifics

Two experiments were performed at the Lawrence Berkeley National Laboratory using the 88" cyclotron, Gammasphere, and Microball detector arrays (these detector arrays were discussed in Chapter 3).

In the first experiment, the 88" cyclotron provided a 128 MeV ^{29}Si beam onto a ^{58}Ni target producing ^{80}Sr via the $^{58}\text{Ni}(^{29}\text{Si}, \alpha 2p)^{80}\text{Sr}$ reaction. The self

supporting thin target had an effective thickness of $246 \mu\text{g}/\text{cm}^2$. This experiment was performed in March of 1994 when Gammasphere had 36 Compton suppressed Ge detectors installed. An E_γ - E_γ - E_γ coincidence cube was constructed with 1.3×10^8 events.

In the second experiment the 88" cyclotron provided a 130 MeV ^{28}Si beam onto a ^{58}Ni target producing ^{80}Sr via the $^{58}\text{Ni}(^{28}\text{Si}, \alpha 2p)^{80}\text{Sr}$ reaction. Thin target data was collected using two stacked, isotopically enriched ^{58}Ni foils, each with a thickness of approximately $400 \mu\text{g}/\text{cm}^2$. In addition, a backed target was used consisting of $420 \mu\text{g}/\text{cm}^2$ ^{58}Ni evaporated onto a ^{181}Ta backing of sufficient thickness to stop the recoiling ^{80}Sr nuclei completely. This experiment was performed in 1995 when Gammasphere had 57 detectors installed. Data was collected using the stacked thin target over a period of three days, and with the backed target over a period of 21 hours.

A total of 1.53×10^9 triple- or higher-fold γ ray coincident events were collected from the thin target run. Of these events, 1.82×10^8 had 2 protons and one α particle detected in coincidence. The thin target data from the second experiment had lower resolution than the data from the first experiment, and so did not provide additional results from coincidence analysis. For the backed target run, about 2.7×10^8 triple- or higher-fold γ ray coincident events were collected. Of these, 3.2×10^7 events were in the $\alpha 2p$ reaction channel. There was no previous backed target data, so lifetime measurements were entirely derived from the second experiment.

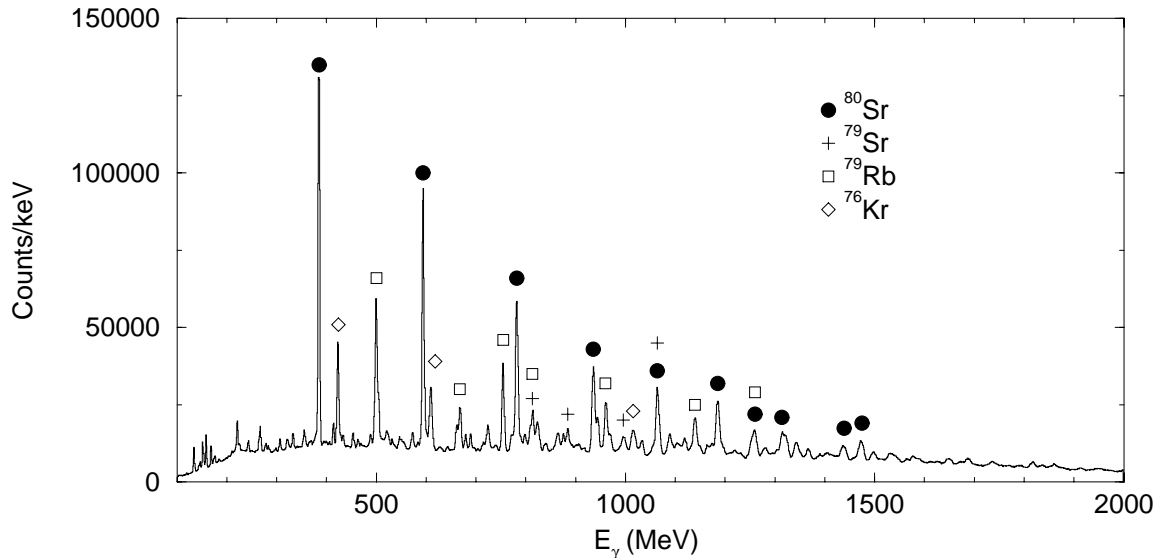


Figure 4.1: Total projection of the $\alpha 2p$ channel. The most intense peaks from each channel are labeled.

4.1.2 Results Using Thin Target Data

Figure 4.1 shows the total projection of triple-gated events in the $\alpha 2p$ exit channel. The dominant channel in the $\alpha 2p$ gate is ^{80}Sr . Other channels appear in the $\alpha 2p$ gate because of undetected particles. Primarily, these undetected particles are neutrons which are not detected in this experiment. Also, 3% of protons and α particles are not detected by Microball. As a result, while ^{80}Sr is the dominant channel in the $\alpha 2p$ gate, there are impurities from ^{79}Sr , ^{79}Rb , and ^{76}Kr , which are produced via the $\alpha 2pn$, $\alpha 3p$, and $2\alpha 2p$ decay channels respectively.

The level scheme deduced from the data is presented in Fig. 4.2. New energy levels and transitions are deduced from coincidence analysis (see section 3.4.2). New spin and parity assignments are deduced from angular distributions and selection rules (see section 3.4.4).

Figures 4.3 and 4.4 show gated spectra constructed from coincidences with each band labeled in Fig. 4.2. The upper panel of Fig. 4.3 shows a spectrum which is the sum of nine double gates. The two energies used for each of the nine double gates are from the nine combinations of 386, 595, or 783 keV with 1324, 1474, or 1578 keV. These nine pairs are (386, 1324), (386, 1474), (386, 1578), (595, 1324), (595, 1474), (595, 1578), (783, 1324), (783, 1474), and (783, 1578). The transitions 386, 595, and 783 keV are at the lower part of the ground state band (GSB) between states with spins $0-6\hbar$, and the transitions 1324, 1474, and 1578 keV are from the middle of the GSB between states with spins $12-18\hbar$. The counts selected from these gates result in a spectrum that contains peaks from transitions in the GSB band. Note that compared to the other selected peaks, the gated peaks in the spectra have intensities which appear to be weaker than their actual transition strengths. This is because each spectrum used for the summation does not include the peaks at the gated energies (as seen in Fig. 3.6). Similarly, the remaining panels in Figs. 4.3 and 4.4 include spectra also resulting from nine double gates each between transitions 386, 595, or 783 keV with a set of three transitions appropriate for each band indicated. These are: (lower panel of Fig. 4.3) 970, 1121, or 1260 keV for SB1; (bottom panel of Fig. 4.4) 877, 997, or 1105 keV for SB2; (middle panel of Fig. 4.4) 662, 867, or 1035 keV for SB3; (top panel of Fig. 4.4) 1030, 1165, or 1307 keV for SB4. In Fig. 4.4, transitions within the band are marked with triangles, and transitions that feed from the band to the ground state band are marked with crosses.

The GSB band was mostly unchanged from the previous level scheme [21]. The one change made was the removal of the 1860 keV line previously placed in the

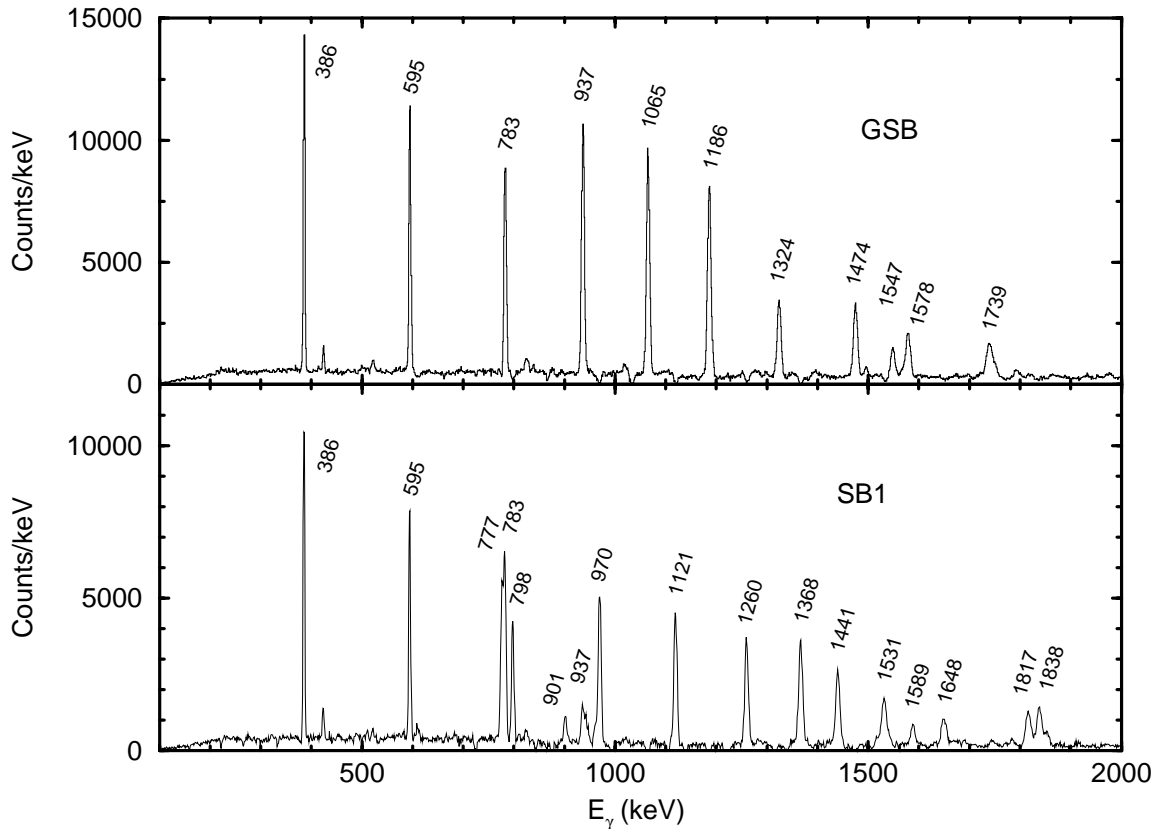


Figure 4.3: Both spectra are the sum of nine double gated spectra from the $\alpha 2p$ coincidence cube. (*Upper panel*) the two gated energies for each of the nine spectra are the combinations of 386, 595, or 783 keV with 1324, 1474, or 1578 keV. The strongest peaks are from transitions in the ground state band (GSB): 386, 595, 783, 937, 1065, 1186, 1324, 1474, 1578, and 1739 keV. The 1547 keV peak is from a transition that feeds into the 9328 keV state in the GSB from side band “a”. (*Lower panel*) The two gated energies for each of the nine spectra are the combinations of 386, 595, or 783 keV with 970, 1121, or 1260 keV. The strongest peaks are from transitions in the first side band (SB1): 777, 970, 1121, 1260, 1368, 1441, 1531, and 1648; states feeding out from SB1: 798, 901, 1817, and 1838 keV; and states in the GSB that are fed by SB1: 386, 595, 783, and 937. The 1589 keV transition feeds into SB1 at the 7730 keV state.

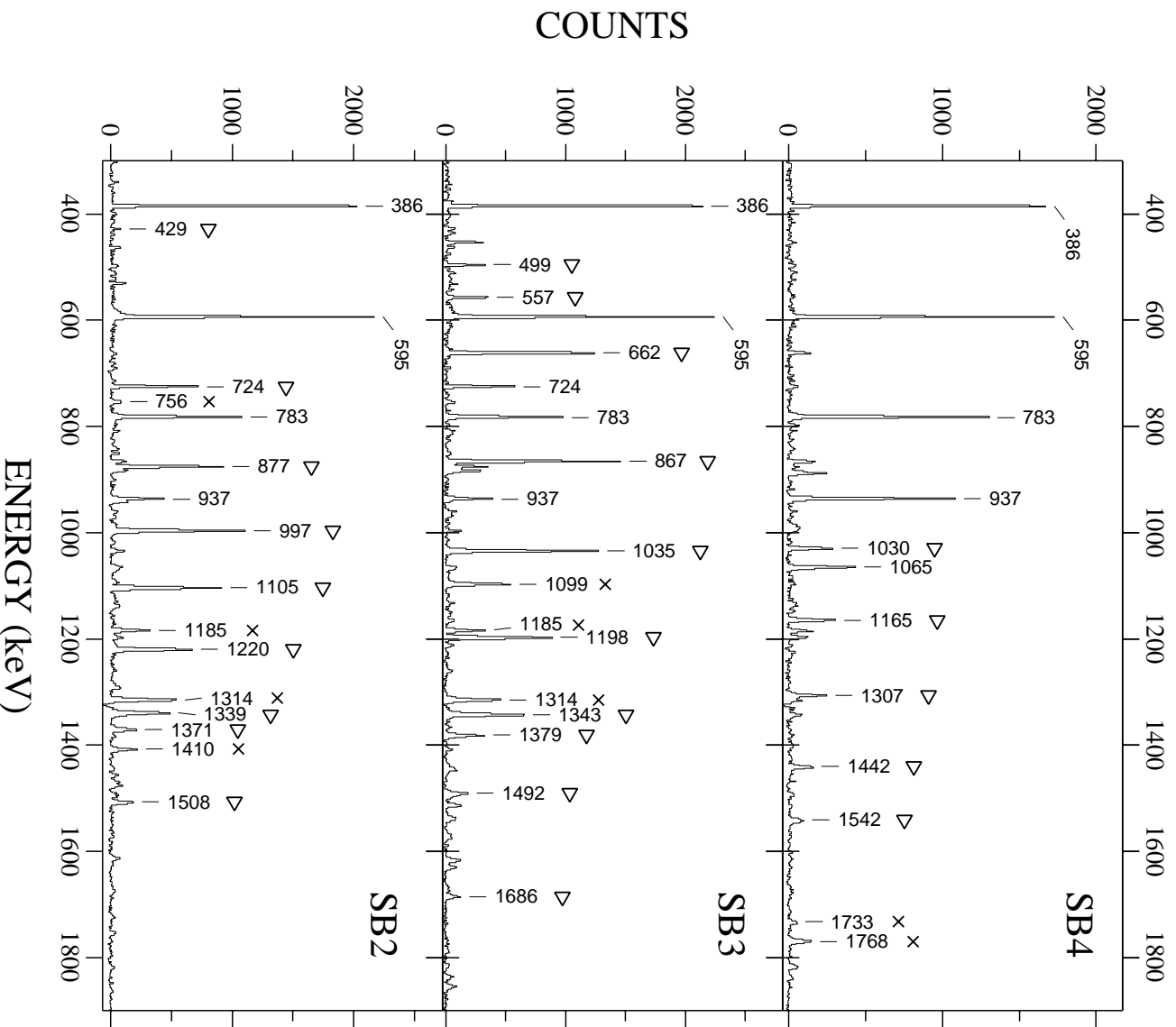


Figure 4.4: Similar to Fig. 4.3, these three panels show spectra that are the sum of nine double gated spectra each. The spectra in each panel are constructed to select transitions from the fourth, third, and second side bands titled SB4, SB3, and SB2 respectively. Transitions marked with triangles belong to the band titled in the panel. Peaks marked with crosses are transitions that feed from the band into the GSB. The gates in each panel consist of the double gates of 386, 595, or 783 keV energies with (*Upper panel*) 1030, 1165, or 1307; (*Middle panel*) 662, 867, or 1035; (*Lower panel*) 877, 997, or 1105 keV.

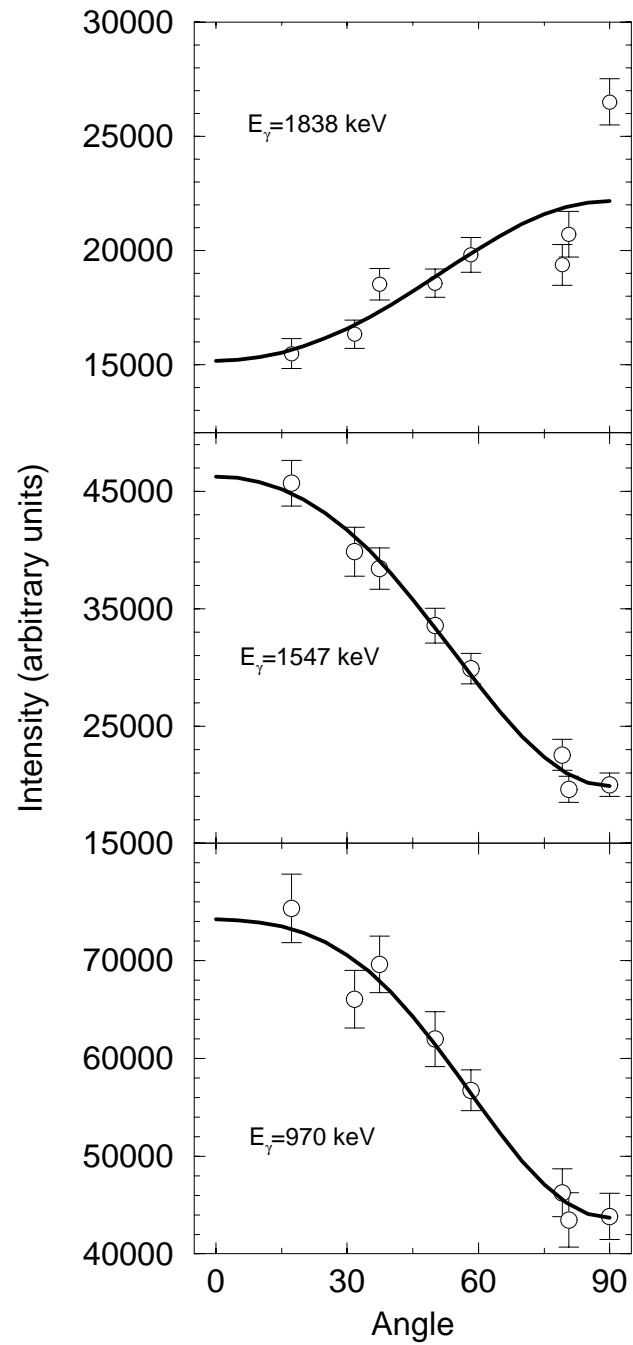


Figure 4.5: Some sample angular distributions. The solid line indicates the best fit to the Legendre polynomial function $W(\theta)$.

GSB band above the 20^+ level. Also, four short new sequences were added that feed into the GSB, labeled as a , b , c , and d in Fig. 4.2. Sequence c contains the 1860 keV transition which was previously placed in the GSB.

The energy of SB3 was shifted down. Previously the 7^+ state in SB3 fed into the 5^+ state of SB2 via a 1343 keV transition. This work substituted a 1099 keV transition for the 1343 keV transition, shifting the whole of SB3 down by 244 keV. This also led to the discovery of other side feeding from SB3 to SB2 via the 884 and 754 keV transitions. Similarly, two more states and four more transitions were discovered that fed from the bottom of SB3 into the GSB. The two states are the 2897 and 2837 keV states, the four transitions are the 499, 557, 1914, and 1856 keV transitions.

Six new levels and seven new transitions were discovered that form the new band, SB4, which feeds into the 8^+ and 10^+ states of the GSB. The transitions were not strong enough to measure spin or parity for the states in SB4.

The 1851 keV transition was added to the top of SB1. Also added were the 1589 keV transition which feeds into the middle of SB1 at the 7730 keV energy level, and the 901 keV transition that feeds out of SB1 into the 8^+ level of the GSB. The 429 and 756 keV transitions were added to the bottom of SB2. Five new transitions were added to the top of SB3. These transitions include the 1343 keV transition which was previously described by Davie *et al.* [21] as feeding from the 7^+ state of SB3 to the 5^+ state of SB2.

An angular distribution analysis was performed for many of the transitions using the techniques described in section 3.4.4. The data was fit to the function

$W(\theta) = A_0[1 + A_2P_2(\cos \theta) + A_4P_4(\cos \theta)]$. Examples of the fits are shown in Fig. 4.5. Since $W(\theta)$ is symmetric about 90° , placing data points for angles $\theta' > 90^\circ$ instead at angles of $\theta = 90^\circ - \theta'$ does not effect the fit. This reflection about 90° is done to aid inspection by placing the data points closer together. With the arguments described in section 3.4.4 and the angular distribution coefficients shown in Table 4.1, we can determine the appropriate spin change of the system associated with many of the transitions. The 1838 keV line appears to take $1\hbar$ of angular momentum from the nucleus because the coefficient of the 1838 keV angular distribution listed in Table 4.1 $a_2 = -0.25$ is not possible for a stretched $E2$ (see Fig. 3.9, $\delta = 0$). Since $a_4 \neq 0$ for the 1838 keV transition, we can say it is not a pure $J \rightarrow J - 1$ transition, so it must be a mixed $E2/M1$ transition. By selection rules, we know the parity does not change for an $E2/M1$ transition, so the 3602 keV state in SB1 has spin and parity $I^\pi = 7^+$. The 1547 keV transition can not take only $1\hbar$ of angular momentum from the system because, with such a large value of a_2 , a $J \rightarrow J - 1$ transition would have $a_4 \geq 0.1$, but the 1547 keV has $a_4 = -0.08 \pm 0.11$. Thus the 1547 keV transition must be a stretched $E2$ transition, so we know that the 10875 keV state in side band "a" has $I^\pi = 20^+$. Similar deduction was used to determine the spins and parities of six other states which were not previously known. From the mixed $E2/M1$ nature of the 1314, 1817 keV transitions, we can deduce the spins and parities of the 2295, 3581 keV states, respectively (shown in Fig. 4.2). From the stretched $E2$ nature of the 877, 884, 662 keV transitions we can deduce the spins and parities of the 3172, 4056, 3394 keV states. From the stretched $E2$ nature of the 777 and 798 keV we can deduce using either of the two transitions the spin and parity of the 4397 keV level.

E_γ	I_i^π	I_f^π	Intensity ^a	a_2	a_4	Multipolarity	δ
662	9 ⁺	7 ⁺	19.9(3)	0.12(6)	-0.01(8)	E2	
724	5 ⁺	3 ⁺	23.5(5)	0.13(5)	-0.10(7)	E2	
777	9 ⁺	7 ⁺	14.3(4)	-0.53(9)	0.59(11)	E2	
783	6 ⁺	4 ⁺	100(1)	0.42(6)	-0.16(8)	E2	
798	9 ⁺	7 ⁺	7.9(5)	0.29(15)	-0.04(21)	E2	
877	7 ⁺	5 ⁺	13.1(2)	0.30(6)	-0.11(9)	E2	
884	9 ⁺	7 ⁺	20.7(2)	0.21(6)	-0.08(8)	E2	
902	7 ⁺	8 ⁺	3.0(3)	0.65(12)	0.31(16)	M1/E2	~ 1.2
937	8 ⁺	6 ⁺	73.4(6)	0.32(5)	-0.09(7)	E2	
970	(11 ⁺)	9 ⁺	15.4(4)	0.39(8)	-0.09(7)	E2	
1035	(13 ⁺)	(11 ⁺)	13.6(3)	0.31(7)	-0.17(9)	E2	
1065	10 ⁺	8 ⁺	57.8(6)	0.42(5)	-0.14(8)	E2	
1105	(11 ⁺)	(9 ⁺)	8.0(2)	0.50(8)	-0.09(10)	E2	
1165	(17 ⁺)	(15 ⁺)	10.4(3)	0.42(8)	-0.13(10)	E2	
1186	12 ⁺	10 ⁺	63.3(4)	0.31(6)	-0.05(7)	E2	
1198	(15 ⁺)	(13 ⁺)	9.8(4)	0.40(8)	-0.35(12)	E2	
1220	(13 ⁺)	(11 ⁺)	6.9(3)	0.42(8)	-0.15(11)	E2	
1262	(15 ⁺)	(13 ⁺)	30.6(4)	0.40(5)	-0.11(8)	E2	
1314	5 ⁺	4 ⁺	30.6(3)	0.33(5)	-0.02(8)	M1/E2	-0.38(5)
1324	14 ⁺	12 ⁺	21.5(3)	0.43(7)	-0.07(9)	E2	
1343	(17 ⁺)	(15 ⁺)	20.5(3)	0.33(6)	0.07(8)	E2	
1368	(17 ⁺)	(15 ⁺)	12.7(3)	0.35(7)	0.01(9)	E2	
1441	(19 ⁺)	(17 ⁺)	12.8(4)	0.20(6)	0.00(8)	E2	
1474	16 ⁺	14 ⁺	29.2(3)	0.40(5)	-0.05(8)	E2	
1547	20 ⁺	18 ⁺	8.2(3)	0.62(8)	-0.08(11)	E2	
1686	(23 ⁺)	(21 ⁺)	11.4(3)	0.46(6)	-0.07(9)	E2	
1817	7 ⁺	6 ⁺	8.2(2)	0.07(6)	-0.05(8)	M1/E2	-0.18(5)
1838	7 ⁺	6 ⁺	5.3(2)	-0.25(6)	0.02(8)	M1/E2	-0.18(5)
1914	(5 ⁺)	4 ⁺	3.0(3)	0.21(9)	0.14(11)	M1/E2	~ -0.34
1937	(25 ⁺)	(23 ⁺)	1.4(2)	0.60(14)	0.08(17)	E 2	
2113	(26 ⁺)	(24 ⁺)	2.0(3)	0.87(12)	-0.11(15)	E2	

^a Normalized to 783 keV transition.

Table 4.1: Partial table of transitions in ⁸⁰Sr.

4.1.3 Backed-Target Data: Lifetimes and Intrinsic Quadrupole Moments

The lifetimes and quadrupole measurements are of considerable interest because they give direct information regarding the collectivity of the states involved. In many cases one observes a phenomenon called “band termination.” Band termination occurs when, at high spins, it becomes energetically favorable for a nucleus to achieve a high angular momenta from the alignment of the individual nucleons with respect to the “axis of rotation”. Within a given shell there is a limit to the maximum angular momentum that can be formed from the available states. When a nucleus reaches this limit it is referred to as band termination. Thus, band termination corresponds to a transition from collectivity to single particle structure. Experimentally, such a transition results in a significant decrease in the intrinsic quadrupole moment Q_t with increasing spins. It has been suggested that band termination could occur in ^{80}Sr .

Backed target data can be used to determine the lifetimes of states in cases where the lifetime is shorter or of the order of the stopping time of the recoils in the target backing. Backed target analysis was performed by Winchell *et al.* [22], and included in this thesis because the author is a coauthor on that paper and it is relevant to the discussion. The line shape of the gamma-ray peak is determined by the “history” of the slowing down and decay process of each recoil. Using the backed-target data, lifetimes of several states in the GSB and SB1 were analyzed using Monte Carlo calculations done by the `LINESHAPE` codes [23]. For a detailed discussion of these programs and their use, see reference [24] and references quoted therein. The spectra

used in the fitting procedure were created by gating below the transitions of interest, using the matrices described in section 4.2.1. For the GSB, the spectrum was created by gating on the 783 keV $6^+ \rightarrow 4^+$ transition. In order to avoid contamination from lines in SB2 and SB3, gates on the 386 keV and 595 keV transitions were not used. For SB1, clean spectra were obtained by gating on the 777, 798, 1817, and 1838 keV transitions. Because the spectra used in the fitting procedure were created by gating from below the transitions of interest, some assumptions had to be made regarding side feeding into the states being analyzed. Intensities for side feeding were deduced from the relative intensities of transitions within the band. For the lifetimes of side-feeding transitions, a rotational model of three transitions with a fixed moment of inertia of $35\hbar^2/\text{MeV}$ was assumed. Quadrupole moments for side feeding are adjusted to give minimum χ^2 during the LINESHAPE fitting procedure.

Examples of the fitted spectra for one of the ground state band transitions are shown in Fig. 4.6. From the analysis, lifetimes of five states in the ground-state band and four states in SB1 are extracted and tabulated in Table 4.2. These lifetimes are converted into transition quadrupole moments using the formula

$$Q_t^2 = \frac{16\pi}{5} \times \frac{1}{\tau} \times \frac{1}{1+\alpha} \times [12.3E_\gamma^5 \langle IK20|I-2K \rangle^2]^{-1}, \quad (4.1)$$

where Q_t , E_γ and lifetime τ are in units of eb, MeV, and picosecond, respectively, and α is the total internal conversion coefficient of the transition. A value of $K = 6$ was assumed for SB1.

The extracted transition quadrupole moments (Q_t) for the ground-state band are plotted in Fig. 4.7 along with those obtained by Davie *et al.* [21]. The uncertainties of the measured Q_t 's do not include those associated with the uncer-

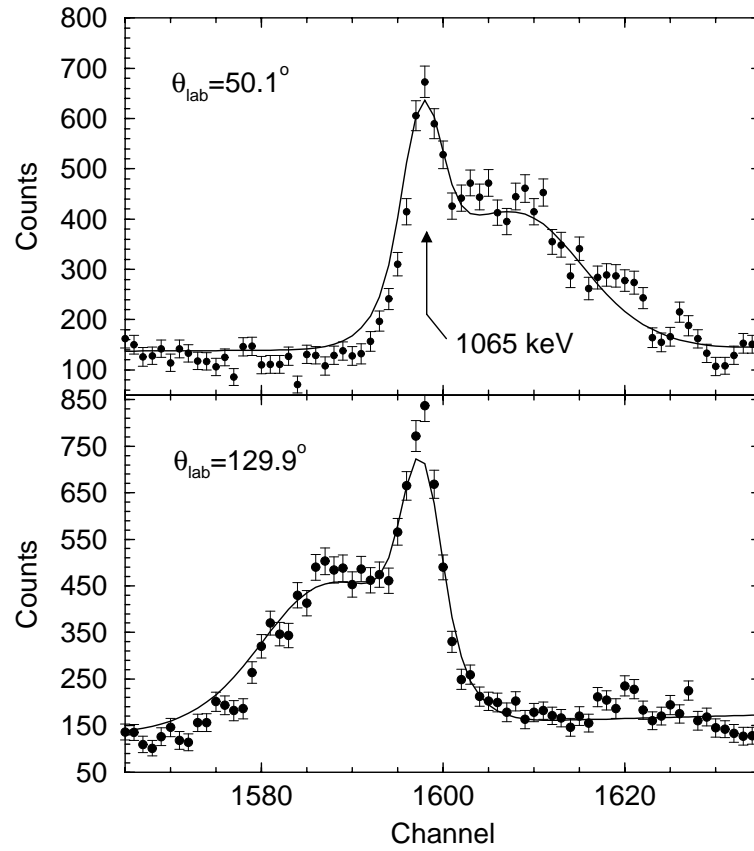


Figure 4.6: Example of backed target data, showing DBLS fit. The line shown is the 1065 keV $10^+ \rightarrow 8^+$ transition.

I^π	E_x (keV)	τ (ps)	Q_t (eb)
8^+	2701	0.41(1)	$2.89^{+0.05}_{-0.04}$
10^+	3766	0.18(1)	$3.12^{+0.04}_{-0.04}$
12^+	4952	0.13(1)	$2.80^{+0.07}_{-0.14}$
14^+	6276	0.17(1)	$1.82^{+0.05}_{-0.02}$
16^+	7750	0.04(1)	$2.97^{+0.37}_{-0.25}$
11^+	5349	0.42(3)	$3.8^{+0.2}_{-0.2}$
13^+	6470	0.19(3)	$3.4^{+0.3}_{-0.2}$
15^+	7730	0.12(3)	$3.0^{+0.4}_{-0.3}$
17^+	9098	0.06(3)	$3.2^{+1.1}_{-0.3}$

Table 4.2: Measured lifetimes and quadrupole moments for selected transitions in the GSB and SB1 of ^{80}Sr .

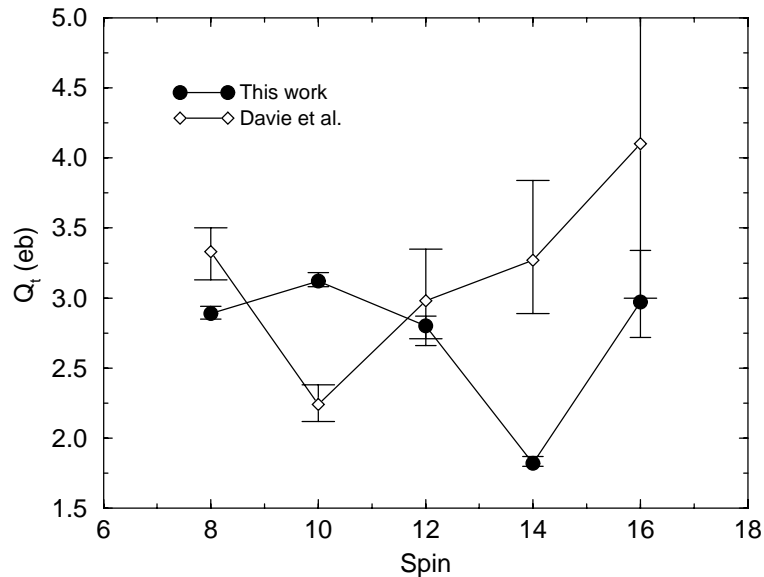


Figure 4.7: Transition quadrupole moments in the ground-state band derived from lineshape analysis. Also shown are results from an earlier work in ^{80}Sr .

tainties of the stopping powers. While the previous results and present work are not in agreement for all levels, neither set of results shows a clear downward trend in the Q_t 's with increasing spin, which would be expected for band termination.

As can be seen in Table 4.2, quadrupole moments for SB1 are roughly constant over the measured range. Quadrupole moments for this band were extracted with the assumption that $K = 6$. Assuming an axially symmetric prolate shape, the measured quadrupole moments correspond to a deformation of $\beta_2 \approx 0.35$.

4.1.4 Cranking Analysis

A cranking analysis of the data was performed as outlined in section 2.7. Kinematic and dynamic moments of inertia for the GSB are plotted in Fig. 4.8. A gradual alignment can be seen at a frequency of $\hbar\omega = 0.55$ MeV, followed by a more abrupt alignment at $\hbar\omega = 0.78$ MeV. In ^{82}Sr , which has a similar pattern in the

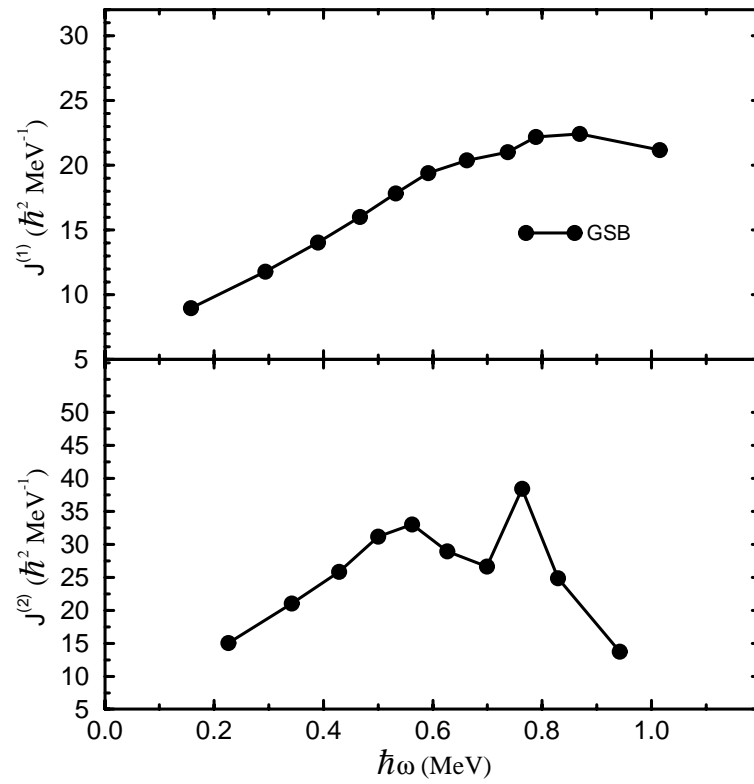


Figure 4.8: Experimental $\mathfrak{J}^{(1)}$ and $\mathfrak{J}^{(2)}$ for the ground state band in ^{80}Sr .

moment of inertia of the ground-state band, measurements made by Kucharska *et al.* of the g -factors near the first backbend show that the alignment is due to a pair of $g_{9/2}$ protons [25]. The second upbend in ^{82}Sr would then be due to a neutron alignment. Comparisons to other nuclei in this mass region support this interpretation. The yrast band of the odd- N nucleus ^{79}Sr shows a sharp upbend at $\hbar\omega = 0.57$ MeV [26]. This must be attributed to the alignment of a pair of protons, since the odd neutron blocks the alignment of a neutron pair. The neighboring odd- Z Nuclei ^{79}Rb [27] and ^{81}Y [28] show no crossings below about $\hbar\omega = 0.68$ MeV, indicating that the higher upbend involves an alignment of a pair of $g_{9/2}$ neutrons. Because our assignments for transitions in the high-spin portion of the GSB are different than Davie *et al.* [21], we do not see the unexplained staggering previously seen in the $\mathfrak{S}^{(2)}$ plot. It is worth noting that the dip in Q_t at $I = 14\hbar$ occurs near the top of the broad proton-crossing alignment discussed above, suggesting that the loss in collectivity, noted in the lifetime measurements, might be related to band-band interaction.

The moments of inertia for the sidebands are plotted in Fig. 4.9. SB2 shows a proton upbend at $\hbar\omega \approx 0.5$ MeV, similar to the one seen in the GSB, and so is most likely based on a neutron excitation. SB1 and SB3 show sharp upbends at frequencies of 0.68 MeV and 0.72 MeV, respectively. Assuming these are similar to the neutron crossing seen in the GSB, this might indicate slightly different deformations for these configurations. SB4, which does not extend as high in angular frequency as SB1 or SB3, shows what might be the beginning of an upbend at about $\hbar\omega = 0.75$ MeV. A comparison to theoretical models will aid in the interpretation of these upbends.

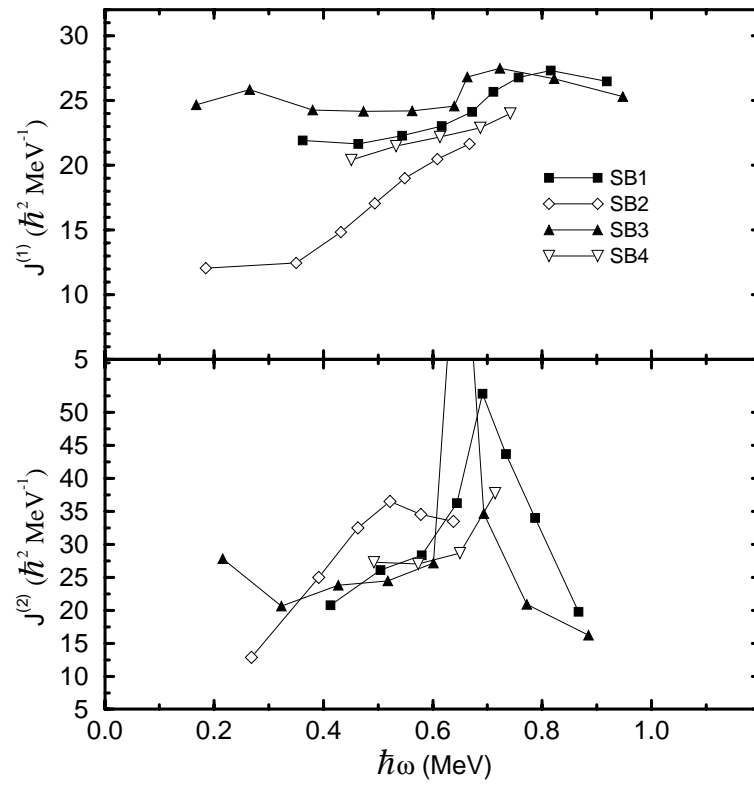


Figure 4.9: Experimental $\mathfrak{S}^{(1)}$ and $\mathfrak{S}^{(2)}$ for the side bands in ^{80}Sr .

4.1.5 Comparison to cranked mean-field with pairing Calculations

In order to better understand the nature of the collective excitations and the evolution of shape in ^{80}Sr , cranked mean-field with pairing calculations were performed. From calculating the total energy of the model for different deformations, using Strutinsky shell correction, total Routhian surfaces can be constructed as seen in Fig. 4.10. The four surfaces each consist of a 15×17 mesh of data points smoothed and plotted on a Hill-Wheeler coordinate system. The angular coordinate $\gamma = 0^\circ$ is angled at 30° above the horizontal with counter-clockwise being the positive direction so that the plot is symmetric about the $\gamma = 60^\circ(120^\circ)$ line. Minima in these plots are the energetically favored deformations. Two competing minima, labeled as a and b , are relevant for the following discussion. As can be seen in the figure, collective prolate deformation a with $\beta_2 \approx 0.35$ is predicted to be the preferred shape at low angular frequency. At $\hbar\omega = 0.4$ MeV, there is pronounced gamma softness towards the collective oblate axis ($\gamma = -60^\circ$), and at $\hbar\omega = 0.6$ MeV there is a minimum at the triaxial deformation b at coordinates $(\beta_2, \gamma) = (0.24, 30^\circ)$ in addition to the prolate minimum. At $\hbar\omega = 0.8$ MeV the prolate minimum a has disappeared and the triaxial minimum b has become more well defined and has moved closer to the $\gamma = -60^\circ$ axis.

Because pairing is treated self-consistently, a comparison can be made between calculated and experimental moments of inertia. In Fig. 4.11, the predicted kinematic moments of inertia for the two sets of deformation parameters are plotted along with the experimental values for the GSB and side band “a”. The theoretical

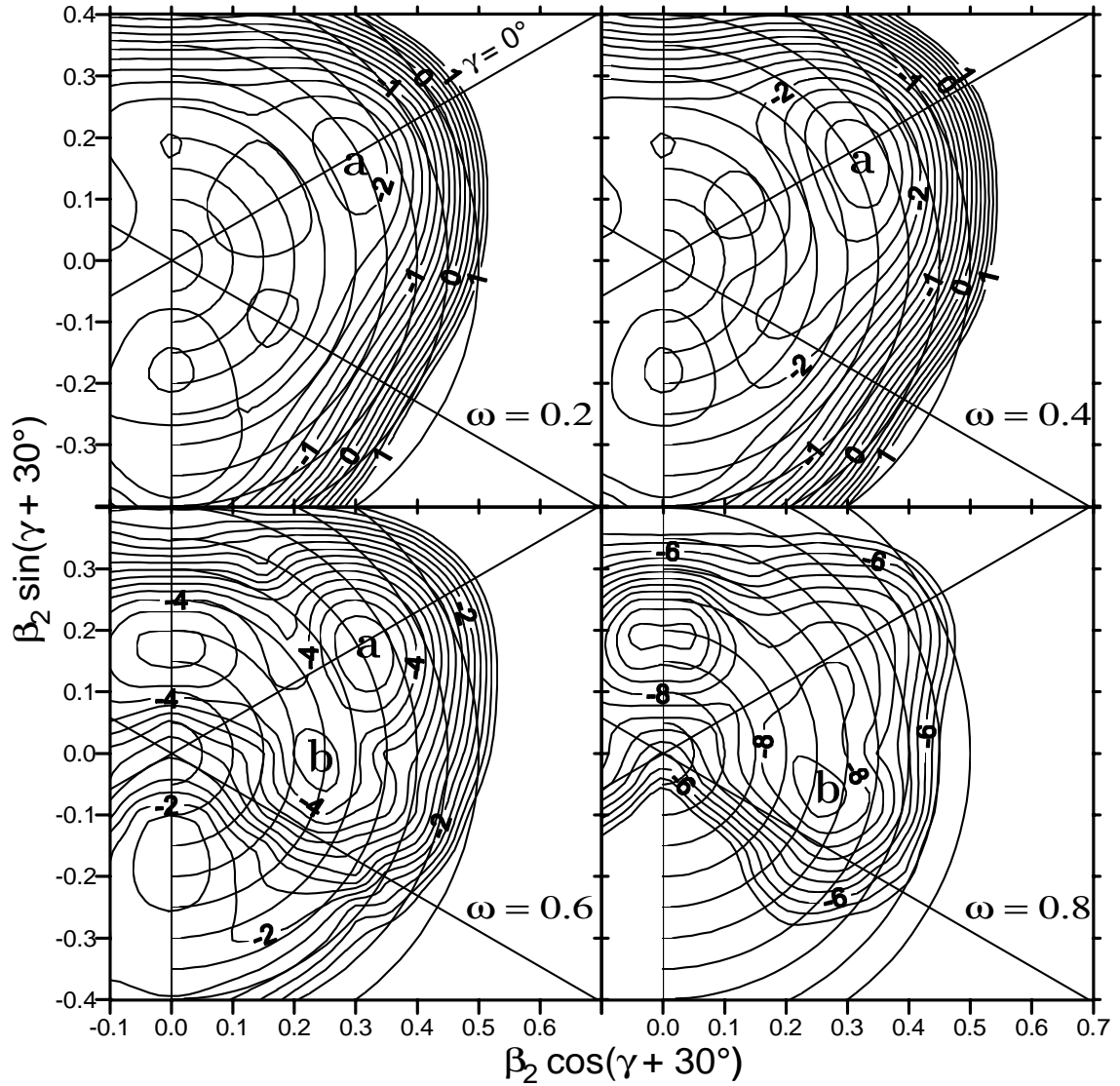


Figure 4.10: TRS surfaces calculated for ^{80}Sr . The angular velocity is labeled in each plot in units of MeV/\hbar . For $\omega = 0.2 \text{ MeV}/\hbar$, the deepest minima is labeled 'a'. Another local minima exists at coordinates $(\beta = 0.20, \gamma = -60^\circ)$, and two more local minima $(\beta = 0.20, \gamma = +60^\circ)$ and $(\beta = 0.35, \gamma = -120^\circ)$ which are due to the symmetry related with low angular velocity. Local maxima exist at $(\beta = 0.20, \gamma = 0^\circ)$ and $(\beta = 0.20, \gamma = -120^\circ)$. At $\omega = 0.6 \text{ MeV}/\hbar$ the local maximum at $\gamma = 0^\circ$ has disappeared. At $\omega = 0.8 \text{ MeV}/\hbar$ only two local minima remain.

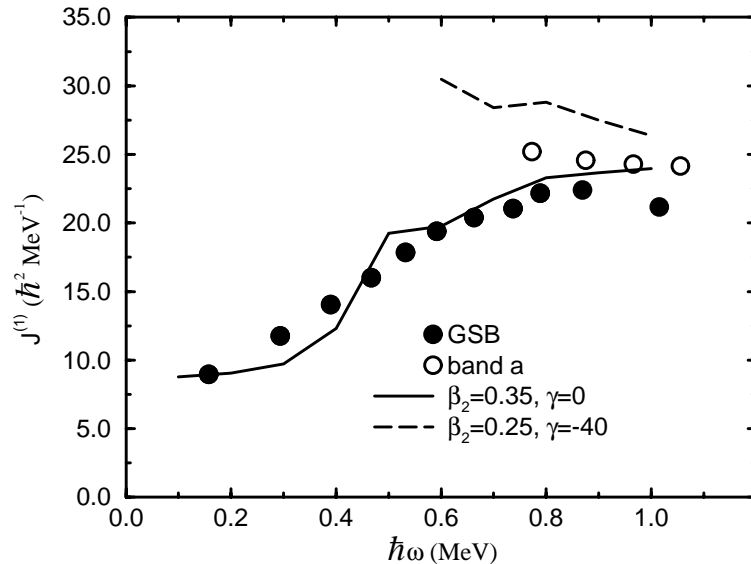


Figure 4.11: Theoretical $\mathfrak{S}^{(1)}$ for ^{80}Sr .

moment of inertia for the prolate deformation a (solid line) is in good agreement with the experimental moments of inertia for the GSB (dots). The theoretical moments of inertia for the triaxial deformation b (dashed line) agrees qualitatively with the experimental moments of inertia for side band “a” (circles).

This compares closely with theoretical predictions by Nazarewicz *et al.* [29], shown in Figs 4.12 and 4.13. In these figures the theoretical energies are plotted as a function of angular momentum for several equilibrium deformations. These deformations are described in the insets using Hill-Wheeler coordinates and labeled 1-21. The parities of states with $\pi = +1$ or $\pi = -1$ are indicated with dots or circles, respectively. States with signature $\alpha = 0$ are plotted in Fig. 4.12. States with $\alpha = 1$ signature are plotted in Fig. 4.13. In Fig. 4.12 the prolate deformation numbered as 1 is yrast up to $20\hbar$ of angular momentum. At this angular momentum, the triaxial deformation labeled 2 in Fig. 4.12, consistent with deformation b from Fig. 4.10,

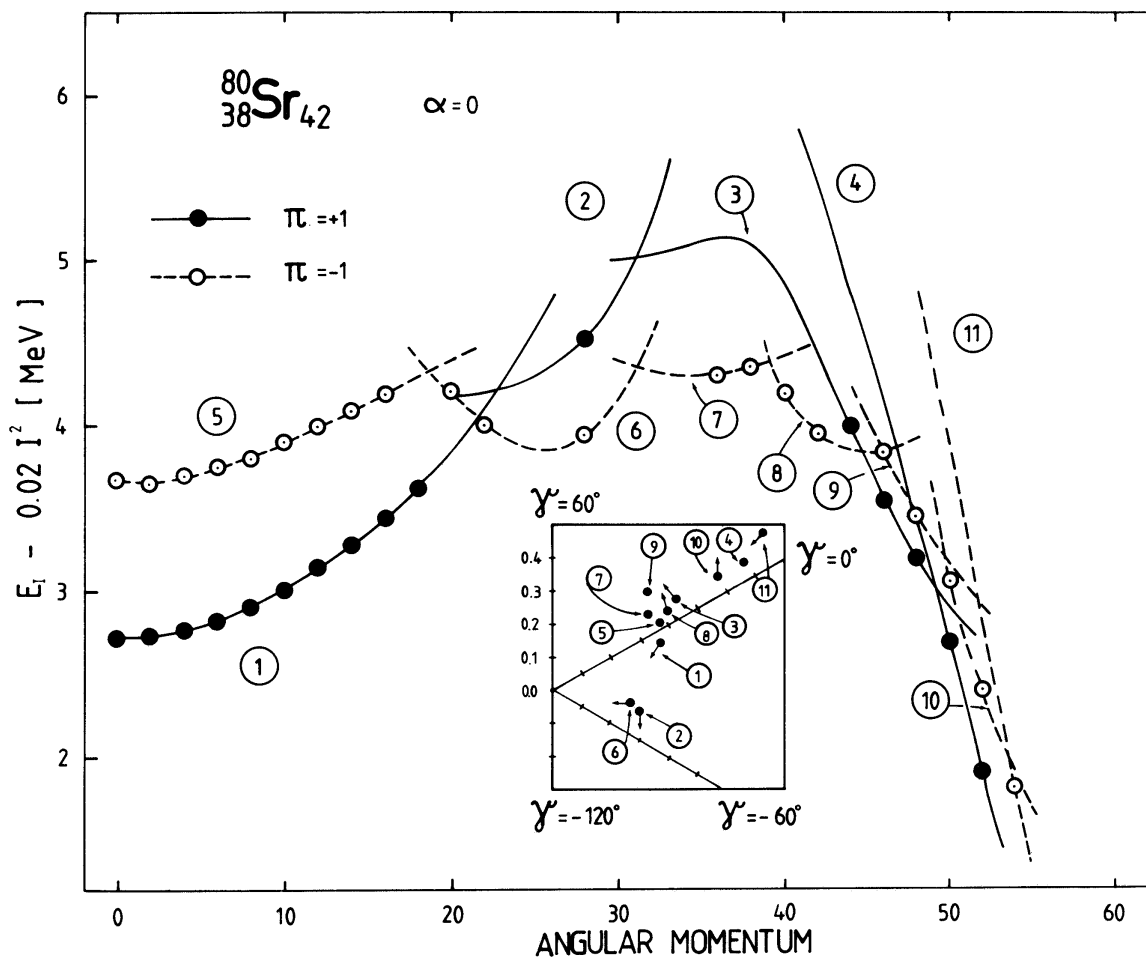


Figure 4.12: Figure obtained from Nazarewicz *et al.* [29] for the energies of even signature states of ^{80}Sr at various deformations described in the inset using the Hill-Wheeler coordinates.

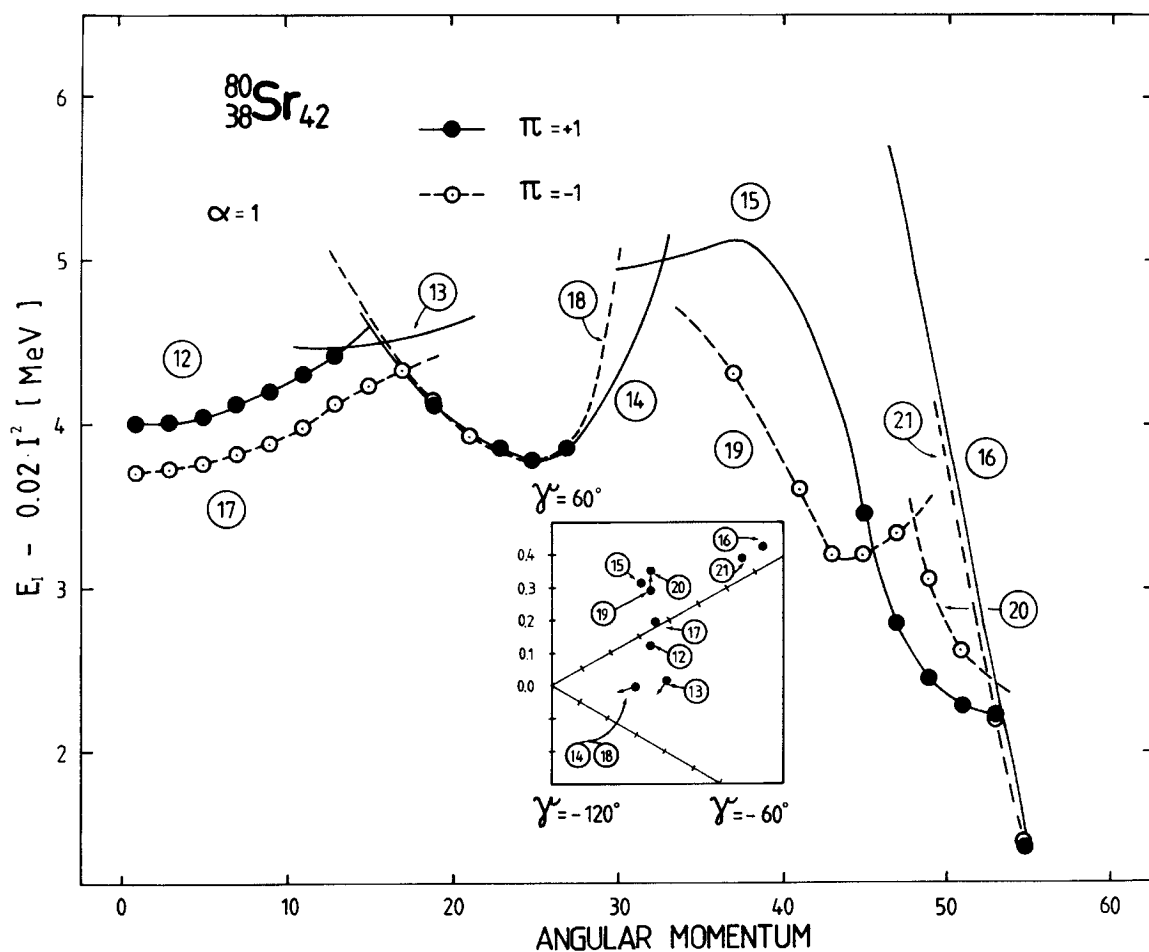


Figure 4.13: Figure obtained from Nazarewicz *et al.* [29] for the energies of odd signature states of ^{80}Sr at various deformations described in the inset using the Hill-Wheeler coordinates.

becomes yrast. This is consistent with our experimental side band “a” which becomes yrast at $20\hbar$. However, Nazarewicz predicts the positive parity and even signature ($r = +1$) triaxial states to be about 0.7 MeV higher in energy than the corresponding odd signature ($r = -1$) states which are shown in Fig. 4.13. With the magnitude of the energies involved, it is not unexpected to observe such a discrepancy.

4.2 Yttrium 85

4.2.1 Experimental Specifics

The experiment was performed at the 88-Inch Cyclotron at the Lawrence Berkeley National Laboratory. High-spin states in ^{85}Y were populated via the $^{58}\text{Ni}(^{31}\text{P}, 4p)$ reaction at a beam energy of 134 MeV. The target was a self-supporting, $380 \mu\text{g}/\text{cm}^2$ ^{58}Ni foil. Gamma rays were detected with the Gammasphere array [7], then comprised of 86 Compton suppressed Ge detectors. Evaporated charged particles were detected with Microball [8], an array of 95 CsI(Tl) detectors covering about 97% of 4π . The event trigger required the presence of a minimum of three Compton-suppressed Ge detectors and registered any coincidence of charged particles that were detected with the Microball. Calibration data consisted of gamma spectra from ^{56}Co and ^{152}Eu sources that were obtained immediately after the run, and scattering data from reactions of protons, deuterons, and α particles on carbon and gold targets for the Microball. A total of 3×10^9 events were collected. This paper describes results from the $4p$ channel, which contained 7.5×10^7 events.

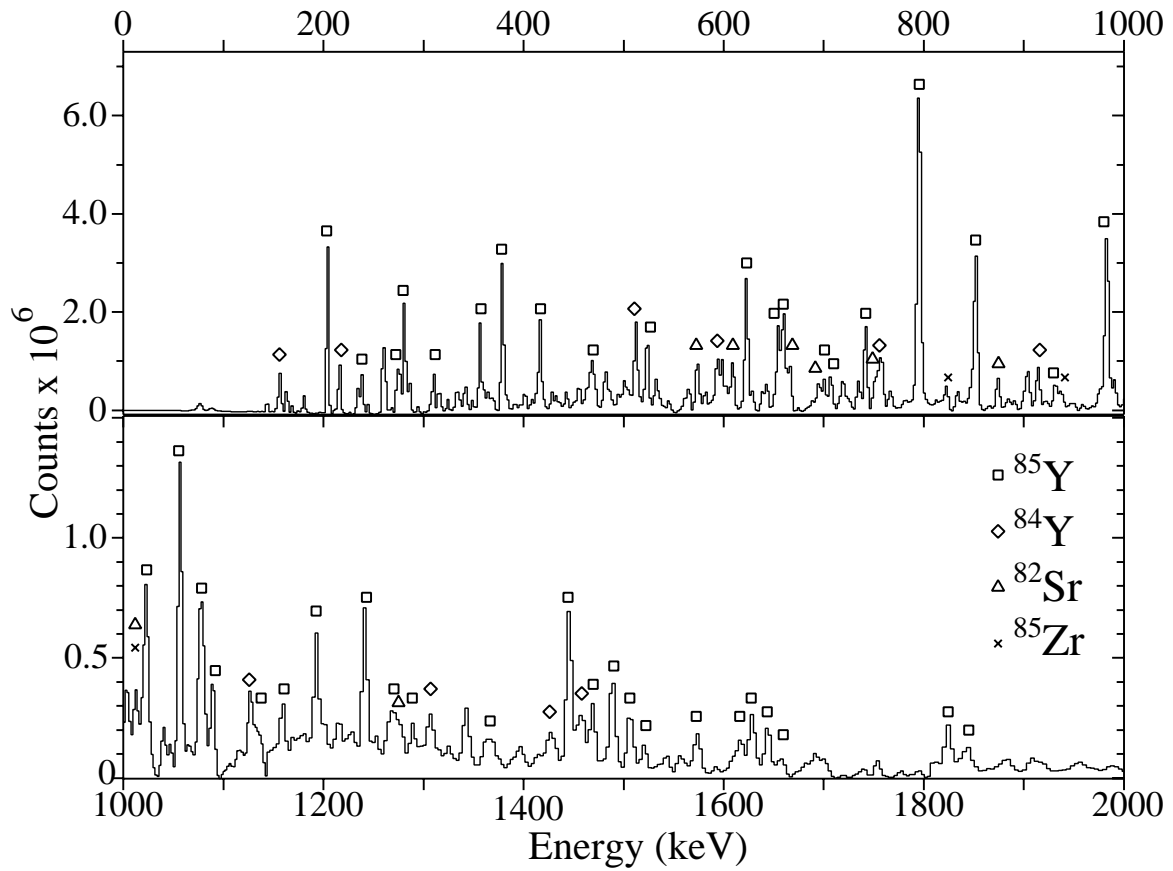


Figure 4.14: Total projection of data from the ^{85}Y experiment. The upper panel shows the spectrum from 0 to 1 MeV, the lower panel shows the spectrum from 1 to 2 MeV. Some of the identifiable peaks from transitions in ^{85}Y , ^{84}Y , ^{82}Sr , and ^{85}Zr are labeled with squares, diamonds, triangles, and crosses.

4.2.2 Results

Figure 4.14 shows a singles spectrum constructed from all triple and higher fold events of γ rays in coincidence with four protons and no α particles. Peaks labeled with a square in Fig. 4.14 are associated with transitions in ^{85}Y . By intensity, this spectrum contains 81% ^{85}Y . Also present in this spectrum are γ rays from ^{84}Y , ^{82}Sr , and ^{85}Zr which are associated with the $4pn$, $\alpha 3p$, and $3pn$ evaporation channels, and are populated with relative intensities of 11.4%, 4.6%, and 3.0%, respectively. In the case of the $3pn$ channel, a neutron was not detected and an additional proton

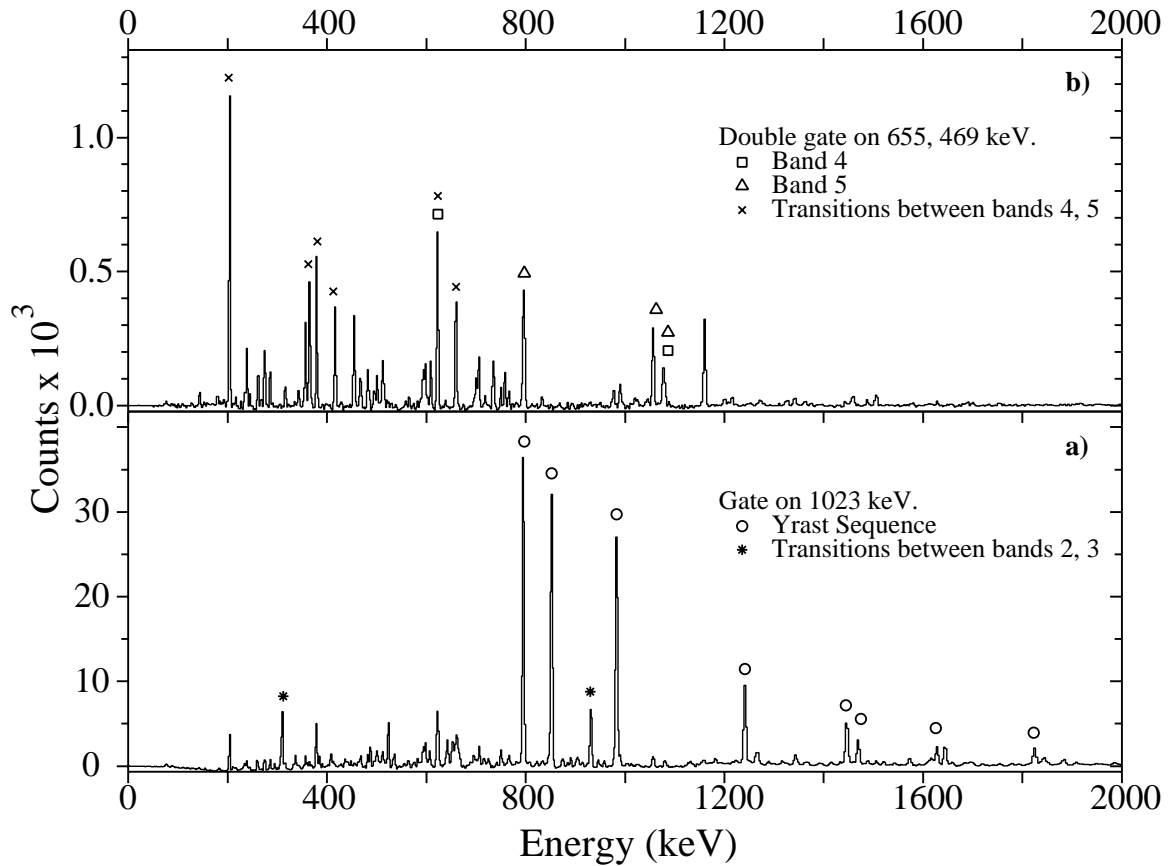


Figure 4.16: Some gated spectra for ^{85}Y . The bottom panel contains a plot of a single gated spectrum on 1023 keV. The top panel contains a plot of a double gated spectrum on 655 with 469 keV. The most intense peaks are labeled by the band to which they belong (see Fig. 4.15 for band labels).

intense peaks in this spectrum are from transitions in the yrast band and strong interband transitions. Double gated spectra were generated from the $E_\gamma - E_\gamma - E_\gamma$ cube. Figure 4.16b shows the spectrum resulting from a double gate on the 469 keV and 655 keV transitions. This spectrum identifies transitions in two negative parity decay sequences feeding the yrast band only at low spin. It also demonstrates the complexity involved in identifying the level structure of the negative-parity states and shows many low intensity peaks that could not be placed in the level scheme.

A sample of the angular distribution data is shown in Fig. 4.17. These plots show data points and best fits to the Legendre polynomial $W(\theta) = A_0[1 +$

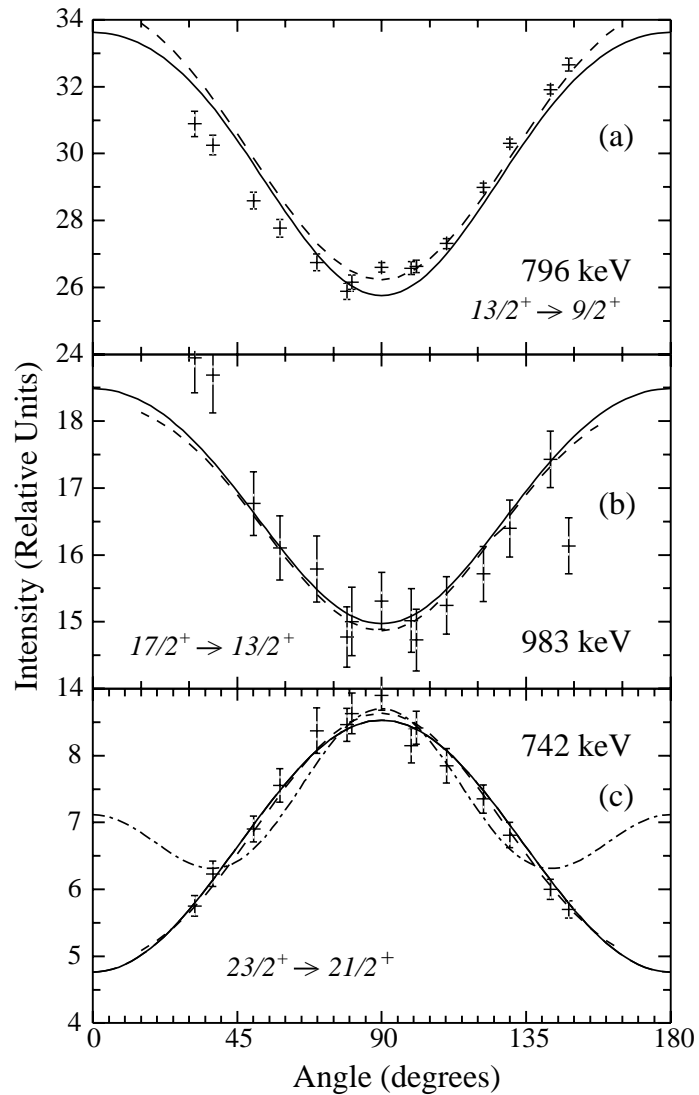


Figure 4.17: Angular distributions for some transitions in ^{85}Y . The solid line indicates the best fit to the Legendre polynomial. The dotted lines in the top two panels indicate the theoretical fit for a pure $E2$ transition. The dotted and dash dotted lines in the bottom panel indicate the theoretical fit for a transition γ ray carrying L units of angular momentum for a pure $L = 1$ or $L = 2$ transition.

$A_2P_2(\cos\theta) + A_4P_4(\cos\theta)$]. In the top and middle panels, theoretical angular distributions for stretched $E2$ transitions are drawn as dotted lines. The bottom panel shows an angular distribution that appears to belong to a transition that takes $1\hbar$ of angular momentum away from the nucleus. This conclusion is made based on the values of the coefficients A_2 and A_4 obtained from the Legendre fit, listed in Table 4.3. For the 742 keV transitions, the A_2 and A_4 values are proportional to the calculated coefficients a_2 and a_4 in 3.10 for a $J \rightarrow J - 1$ transition at $\arctan\delta \approx 0^\circ$ or 90° . In the bottom panel of Fig. 4.17, two additional lines are drawn to show the theoretical angular distributions for a pure $E1$ or $M1$ transition (dotted line), and for a pure $E2$ transition (dash-dotted line). One can see from the figure that detectors at angles near 0° and 180° degrees would make mixing measurements more accurate (the lack of detectors at these angles was due to the difficulties related to having detectors near the beamline).

4.2.3 Level Scheme

The level scheme shown in Fig. 4.15 extends the previous level scheme [21] by adding 37 new γ rays and 24 new energy levels. The placement of levels in the present study was based on coincidence, intensity, and energy relations. Spin assignments were based on angular distributions and selection rules. Tables 4.3-4.7 list the observed transitions in ^{85}Y according to the band and energy of the transitions' initial states. Listed at the end of Table 4.6 and in Table 4.7 are 15 states from the level scheme that do not belong to one of the six numbered bands.

E_i	I_i^π	I_f^π	E_γ	Intensity	A_2	A_4	Multipolarity or $\tan^{-1}\delta_{min}$	$\chi^2(\delta_{min})$
2991	$\frac{21}{2}^+$	$\frac{21}{2}^+$	341	3.8(2)	0.06(3)	0.01(5)	36(30), -57(25)	9, 20
		$\frac{17}{2}^+$	1193	13.6(5)	0.26(3)	-0.04(4)	$E2$	
4080	$\frac{25}{2}^+$	$\frac{23}{2}^+$	690	2.2(2)				
		$\frac{21}{2}^+$	1089	8.4(3)	0.13(6)	-0.25(8)	$E2$	
5449	$\frac{29}{2}^+$	$\frac{27}{2}^+$	844	2.2(2)				
		$\frac{25}{2}^+$	1288	4.3(2)				
		$\frac{25}{2}^+$	1369	2.9(2)				
6740	$\frac{33}{2}^+$	$\frac{33}{2}^+$	378	2.5(2)				
		$\frac{29}{2}^+$	1291	1.6(2)	0.26(5)	-0.08(6)	$E2$	
		$\frac{29}{2}^+$	1825	4.1(2)	0.23(3)	-0.11(2)	$E2$	
3392	$\frac{23}{2}^+$	$\frac{21}{2}^+$	402	2.4(2)	-0.32(9)	0.02(15)	4(6), 7.00	17, 30
		$\frac{21}{2}^+$	742	27.6(8)	-0.36(2)	0.03(3)	6(3), 81(2)	8, 29
4604	$\frac{27}{2}^+$	$\frac{25}{2}^+$	524	8.6(3)				
		$\frac{25}{2}^+$	931	10.4(3)	-0.56(3)	0.04(4)	$\sim 10, \sim 78$	35, 80
		$\frac{23}{2}^+$	1212	2.5(2)				
6179	$\frac{31}{2}^+$	$\frac{27}{2}^+$	730	0.6(1)			$E2$	
		$\frac{27}{2}^+$	1574	3.7(2)	0.26(4)	-0.07(5)	$E2$	

Table 4.3: Table of transitions in ^{85}Y for bands 1 and 2.

E_i	I_i^π	I_f^π	E_γ	Intensity	A_2	A_4	Multipolarity or $\tan^{-1}\delta_{min}$	$\chi^2(\delta_{min})$
815	$\frac{13}{2}^+$	$\frac{9}{2}^+$	795	105.6(30)	0.19(1)	-0.01(1)	$E2$	
1799	$\frac{17}{2}^+$	$\frac{13}{2}^+$	983	80.3(24)	0.18(2)	-0.08(2)	$E2$	
2650	$\frac{21}{2}^+$	$\frac{17}{2}^+$	852	57.9(16)	0.21(3)	-0.08(4)	$E2$	
3673	$\frac{25}{2}^+$	$\frac{23}{2}^+$	281	23.3(7)	-0.40(1)	-0.09(2)	$\sim 4, \sim 85$	120, 460
		$\frac{21}{2}^+$	1023	17.6(5)	0.35(1)	-0.06(2)	$E2$	
4914	$\frac{29}{2}^+$	$\frac{27}{2}^+$	310	8.4(3)	-0.35(2)	-0.01(3)	5(4), ~ 85	22, 56
		$\frac{25}{2}^+$	1241	17.7(5)	0.33(2)	-0.16(2)	$E2$	
6361	$\frac{33}{2}^+$	$\frac{29}{2}^+$	1447	12.4(4)	0.24(1)	-0.12(2)	$E2$	
8007	$\frac{37}{2}^+$	$\frac{33}{2}^+$	1268	4.1(1)				
		$\frac{33}{2}^+$	1646	6.1(2)	0.48(5)	-0.26(2)	$E2$	
9478	$\frac{41}{2}^+$	$\frac{37}{2}^+$	1470	7.1(2)	0.30(2)	-0.20(3)	$E2$	
11107	$\frac{45}{2}^+$	$\frac{41}{2}^+$	1629	5.3(2)				
12936	$\frac{49}{2}^+$	$\frac{45}{2}^+$	1829	3.0(1)				
15135	$\frac{53}{2}^+$	$\frac{49}{2}^+$	2199	0.6(1)			$E2$	

Table 4.4: Table of transitions in ^{85}Y for band 3.

E_i	I_i^π	I_f^π	E_γ	Intensity	A_2	A_4	Multipolarity or $\tan^{-1}\delta_{min}$	$\chi^2(\delta_{min})$
2304	$\frac{15}{2}^-$	$\frac{13}{2}^+$	655	14.8(5)	-0.25(1)	-0.02(2)	(E1)	
		$\frac{13}{2}^+$	1489	8.5(3)	-0.11(2)	0.00(4)	(E1)	
2927	$\frac{19}{2}^-$	$\frac{21}{2}^+$	276	5.4(2)	0.00(3)	-0.09(5)	(E1)	
		$\frac{15}{2}^-$	623	11.6(5)				
		$\frac{17}{2}^+$	666	9.9(4)	-0.31(9)	-0.02(9)	(E1)	
		$\frac{17}{2}^+$	1129	3.2(2)				
4006	$\frac{23}{2}^-$		485					
		$\frac{21}{2}^-$	700	6.3(3)	-0.58(5)	-0.09(7)	10(8), 80(5)	6, 24
		$\frac{19}{2}^-$	1079	8.1(3)	0.24(2)	-0.10(2)	E2	
5025	$\frac{27}{2}^-$	$\frac{25}{2}^-$	660	21.5(6)	-0.52(2)	-0.05(2)	7(2), ~83	18, 300
2508	$\frac{17}{2}^-$	$\frac{15}{2}^-$	204	25.2(9)	-0.28(1)	-0.14(2)		
3306	$\frac{21}{2}^-$		286					
		$\frac{19}{2}^-$	379	20.8(8)	-0.31(1)	0.11(1)	~5, ~84	57, 73
		$\frac{17}{2}^-$	798	10.5(8)				
4363	$\frac{25}{2}^-$	$\frac{23}{2}^-$	357	10.3(4)	-0.32(1)	0.09(2)	~5, ~84	110, 150
		$\frac{21}{2}^-$	1057	20.6(6)	0.18(2)	-0.18(3)	E2	
5439	$\frac{29}{2}^-$	$\frac{27}{2}^-$	417	11.7(4)	-0.34(4)	0.01(5)	5(7), 85(6)	8, 19
		$\frac{25}{2}^-$	1076	8.2(3)				

Table 4.5: Table of transitions in ^{85}Y for bands 4 and 5.

E_i	I_i^π	I_f^π	E_γ	Intensity	A_2	A_4	Multipolarity or $\tan^{-1}\delta_{min}$	$\chi^2(\delta_{min})$
			1659	1.1(1)				
			1787	0.1(1)				
			1909	0.3(1)				
			2056	0.1(1)				
			2200	0.1(1)				
474		$\frac{9}{2}^+$	454	1.3(7)				
1180	$\frac{11}{2}$	$\frac{13}{2}^+$	365	1.7(2)	-0.19(3)	0.08(5)	-2(5), 85(5)	18, 19
			706	1.6(2)	-0.09(4)	-0.02(5)		
		$\frac{9}{2}^+$	1159	2.4(2)	-0.55(4)	0.15(5)	~12, ~74	100, 100
1649	$\frac{13}{2}^+$	$\frac{11}{2}$	469	7.8(3)				
		$\frac{13}{2}^+$	834	4.7(3)				
		$\frac{9}{2}^+$	1630	1.7(5)				
1790		$\frac{13}{2}^+$	976	9.2(6)				

Table 4.6: Table of transitions in ^{85}Y for band 6 and some of the levels in the level scheme that do not appear to belong to a band.

E_i	I_i^π	I_f^π	E_γ	Intensity	A_2	A_4	Multipolarity or $\tan^{-1}\delta_{min}$	$\chi^2(\delta_{min})$
2260	$\frac{17}{2}^+$	$\frac{17}{2}^+$	463	4.3(3)				
		$\frac{13}{2}^+$	1445	10.1(6)	0.27(9)	-0.11(2)	$E2$	
2747		$\frac{17}{2}^-$	238	4.6(2)	-0.01(3)	-0.20(4)	$E2$	
3020			274	4.0(4)	-0.40(4)	0.00(5)	6(6), 83(4)	14, 29
			512					
3521			501					
4160	$\frac{25}{2}^+$	$\frac{25}{2}^+$	487	2.4(3)	-0.12(5)	-0.03(6)	$\sim 52, \sim 78$	
		$\frac{23}{2}^+$	768	4.2(3)	-0.42(4)	-0.02(7)	7(8), 81(7)	7, 16
		$\frac{21}{2}^+$	1169	2.8(3)				
		$\frac{21}{2}^+$	1510	3.2(4)				
5066	$\frac{29}{2}^+$	$\frac{25}{2}^+$	905	2.7(3)	0.18(3)	-0.01(5)	$E2$	
6968	$\frac{33}{2}^+$	$\frac{29}{2}^+$	1521	3.3(2)	0.52(6)	-0.12(8)	$E2$	
8512	$\frac{37}{2}^+$	$\frac{33}{2}^+$	1543	1.0(1)	0.42(8)	-0.05(10)	$E2$	
8585	$\frac{37}{2}^+$	$\frac{33}{2}^+$	1618	1.2(2)				
14781	$\frac{53}{2}^+$	$\frac{49}{2}^+$	1846	2.2(2)	0.18(3)	-0.11(3)	$E2$	
17253		$\frac{53}{2}^+$	2472	0.7(1)				

Table 4.7: Table of transitions in ^{85}Y for some of the levels in the level scheme that do not appear to belong to a band.

4.2.3.1 Yrast Band

Band 3, or the yrast band, has been previously seen up to spin $29/2^+$. The new transitions above spin $29/2^+$ are clearly seen in coincidence with the yrast sequence. However, some investigation was required to determine the ordering of these transitions. Two transitions of similar energy, 1825 and 1829 keV, caused some difficulty in the coincidence analysis, but gates on the 1646 and 1268 keV transitions separated the two decay paths to reveal the 6361, 6740, and 8007 keV levels. The ordering of the 1470, 1629, 1829 keV transitions above the 8007 keV level is based on energy and intensity considerations.

Angular distributions imply that the 1447, 1646, and 1470 keV transitions above the 4914 keV level are stretched $E2$ transitions, allowing for definite spin and

parity assignments for the 6361, 6740, 8007, and 9478 keV levels. Statistics were not good enough to produce meaningful angular distributions for transitions above the 9478 keV level.

4.2.3.2 Bands 1, 2 and Possible New Band

We have established 17 new transitions and 7 new levels that belong to bands 1, 2, and possibly another band with a band head energy of $E = 4160$ keV. Most of the spins and parities of these levels could be determined with certainty. The spin and parity of the two lowest levels in band 1 are certain because of the stretched $E2$ transitions 1193, 1089 keV. The spin and parity of the 6740 keV level in band 1 is certain because of the stretched $E2$ transitions 1268, 1825 keV. Only two levels, with energies 5449 and 4160 keV, connect the $I=33/2^+$ state at 6740 keV to the $I=21/2^+$ state at 2650 keV. Thus, the three connecting transitions, which remove $6\hbar$ of angular momentum from the nucleus, must each remove $2\hbar$ of angular momentum. So the 1291, 1288, and 1510 keV transitions must be stretched $E2$, and the 5449, 4160 keV levels must have spin-parities of $29/2^+$ and $25/2^+$ respectively. Also, since angular distributions show that the 905 keV transition is a stretched $E2$, we can assign spin-parity of $29/2^+$ to the 5066 keV level.

Angular distributions show that the 742, 281, 931, and 310 keV transitions remove $1\hbar$ of angular momentum from the nucleus. This makes the spins of band 2 certain. However, the parity can not be determined. For example, from Fig. 4.17, the angular distribution of the 742 keV line includes few angles near 0° and 180° , making it difficult for us to be certain whether the transition is $E1$ or a mixed $M1/E2$

transition. So we adopt the assignment from Diller *et al.* [21] for the 3392 keV level in band 2. Diller *et al.* found the 742 and 281 keV transitions to be mixed $M1/E2$, and thus the parity of the $23/2$ level to be positive. The other two states in band 2 were tentatively labeled as having positive parity.

4.2.3.3 Negative Parity Bands 4 and 5

The details of the level structure of bands 4 and 5 was difficult to resolve using single and double coincidence analysis. Because of the large number of multiplets and the non-collective nature of the bands, any spectrum resulting from a single or double gate would include nearly all of the other transitions in these bands. Also because of the irregular structure of these bands, comparison with a rotational band structure could not aid in sorting out the transitions of these bands. As a result, we have made minimal changes to the negative-parity levels presented by Diller *et al.* [21]. (We have adopted the assignment of negative parity to this band by Diller *et al.* [30], discussed in section 4.2.4). One change involved the removal of a 623 keV transition. Coincidence data show that the 623 keV transition is a doublet. The level scheme presented in this work places only one 623 keV line, between the 2927 and 2304 keV levels of band 4. The previous level scheme placed a second 623 keV line that fed into the 4363 keV level. In the present analysis we were able to verify the existence, but not the placement of a second 623 keV line.

In addition to the transitions shown in the level scheme, transitions of energies 260, 466, 594, 600, 610, 623, 735, 758, 874, 904, 990, 1460 and 1506 keV are also seen in coincidence with bands 4 and 5. They are not placed in the level scheme

because of the difficulties with the coincidence analysis. Angular distribution analysis verified the spin assignments of levels at energies of 1180, 1649, 2304, 2927, 3306, 4006, 4363, 5025, and 5439 keV in bands 4 and 5 and the levels connecting these bands to the yrast state. The 474 keV state is labeled tentatively as $9/2^+$ because of the low intensity of the 454 and 706 keV transitions. As argued by Diller *et al.*, the relatively long lifetimes of the 2304 and 2927 keV levels suggest these states are negative-parity [30], but one cannot exclude the possibility that these transitions are of retarded $M1$ character.

4.2.3.4 Band 6

We report here band 6 as a tentative superdeformed band. Its γ -ray energies and lack of connecting transitions to other bands is typical of a superdeformed band in the mass 80 region. Spectra resulting from single gates on transitions in band 6 generally contain peaks not much larger than the background. Spectra resulting from double gates on these transitions contained too few counts to discern peaks.

Figure 4.18 shows the spectrum resulting from the sum of single-gated spectra of all the transitions in band 6. A fraction of the total projection is subtracted to compare transitions fed from band 6 (positive peaks) to impurities and transitions that are not fed by band 6 (negative peaks). From this spectrum we can conclude that this band feeds primarily into the yrast $29/2^+$ state above the 1241 keV transition. Due to the low intensity of these transitions, we are only reporting this band as tentative. To be certain of this band, an experiment focused on populating high spin states in ^{85}Y would be needed.

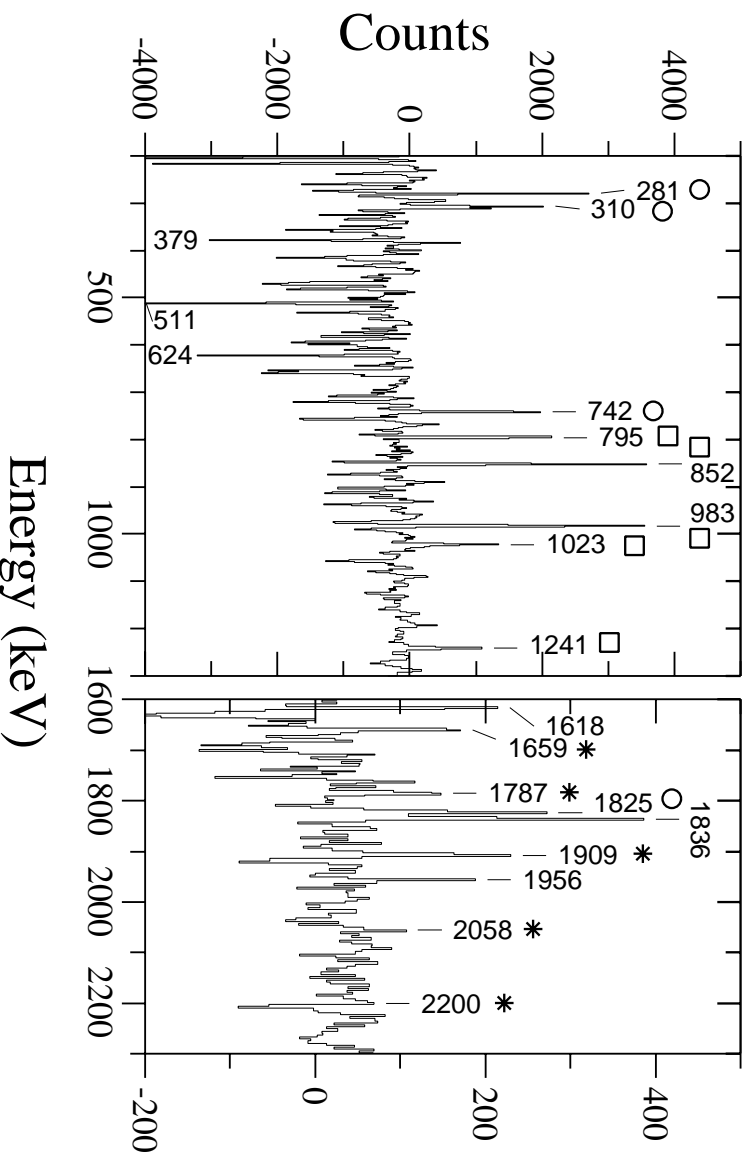


Figure 4.18: Spectrum resulting from the sum of transitions in band 6 corresponding to energies 1659, 1787, 1909, 2056, and 2200 keV. An additional fraction of the total projection was subtracted to illustrate sequences fed by band 6. Energies between 1300 and 1600 keV are not shown to save space, no notable peaks are seen in that region. Transitions tentatively assigned to band 6 are labeled with an asterisk, transitions belonging to yrast band in ^{85}Y are labeled with a square, and other transitions in ^{85}Y are labeled with a circle.

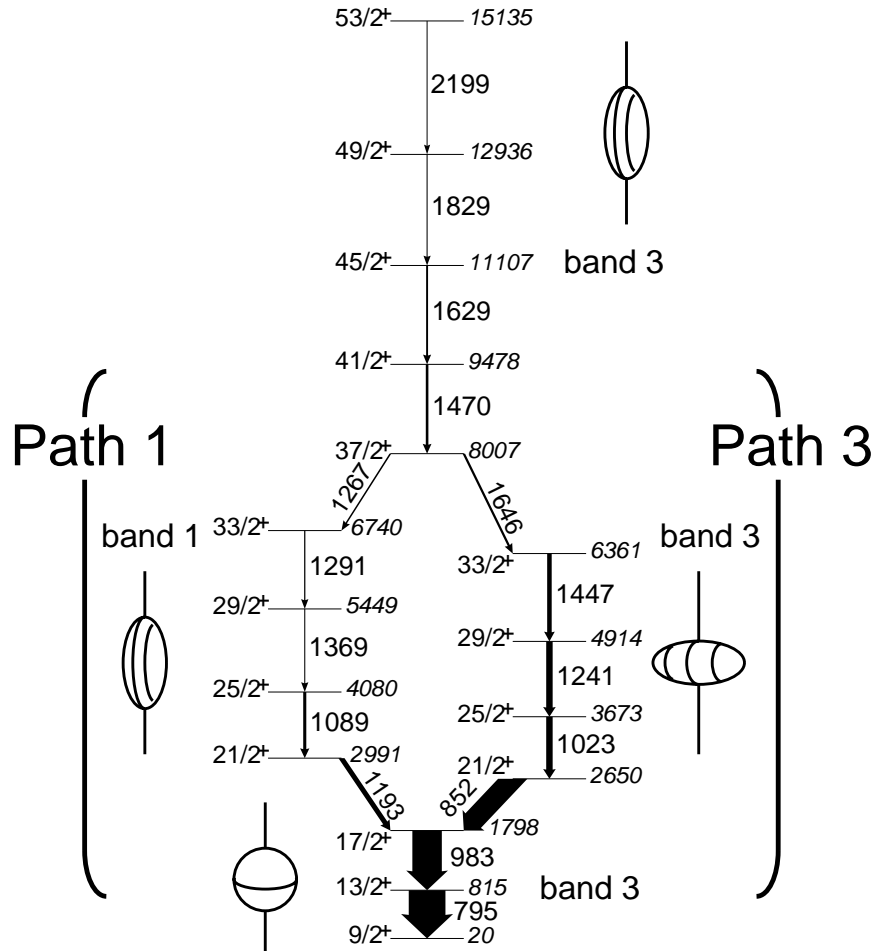


Figure 4.19: Decay sequence for the $(\pi, \alpha) = (+, +)$ states drawn to illustrate the forking. Path 1 indicates the entire decay sequence that passes through band 1, and path 2 indicates the entire decay sequence through the yrast states in band 3.

4.2.4 Discussion

We first focus on the decay of the two positive parity positive signature bands 1 and 3. For this discussion it is useful to represent the decay of these bands in an alternative way as shown in Fig. 4.19. A notable feature of this decay is the occurrence of forking. One notes that in the interval between $I^\pi = 17/2^+$ and $37/2^+$ there are two sequences of states with identical spin and parity but different excitation energies. A very similar forking exists in the isotone ^{87}Nb [31]. The fork at $I^\pi = 17/2^+$ extends

to $I^\pi = 29/2^+$, but no direct transition has been established between the $29/2^+$ state and the $33/2^+$ member of the yrast band. Forking has also been established in even-even nuclei in this mass region, namely ^{84}Sr [32], ^{78}Sr and ^{82}Zr [33]. In the latter two nuclei, Rudolph *et al.* argue that forking may be explainable (in the cranking model) by the existence of two competing shapes: prolate and prolate-triaxial. We will show in section 4.2.4.2 that in ^{85}Y , these two forks are associated with collective prolate and oblate deformations. The states below the $21/2^+$ states are consistent with non-collective, near spherical rotation because the band structure does not resemble that of a rotor and has a very small moment of inertia (see Sec. 4.2.4.1).

The negative parity bands have been previously analyzed by Diller *et al.* [30] who pointed out the similarity in the transition strengths between the negative parity states in ^{84}Sr and ^{85}Y . Neither the present work nor that of reference [30] provide direct evidence for the parity of these bands. The parity assignment is based on the similarity between these bands and the negative parity bands in ^{84}Sr [32]. In the case of ^{84}Sr the parity could be assigned on the basis of g-factor determinations, which suggest the intrinsic structure of these states to be $\pi(g_{9/2}^1(p_{3/2}, f_{5/2})^{-1})$. For ^{85}Y , the additional proton would occupy the $g_{9/2}$ orbital, maintaining the negative parity of the bands.

4.2.4.1 Cranking Model Analysis

A cranking-model analysis [34] was performed for the two positive parity positive signature decay paths 1 and 3. Figure 4.20a shows the kinematic moment of inertia $\mathfrak{S}^{(1)}$ and experimental Routhians as a function of rotational frequency along

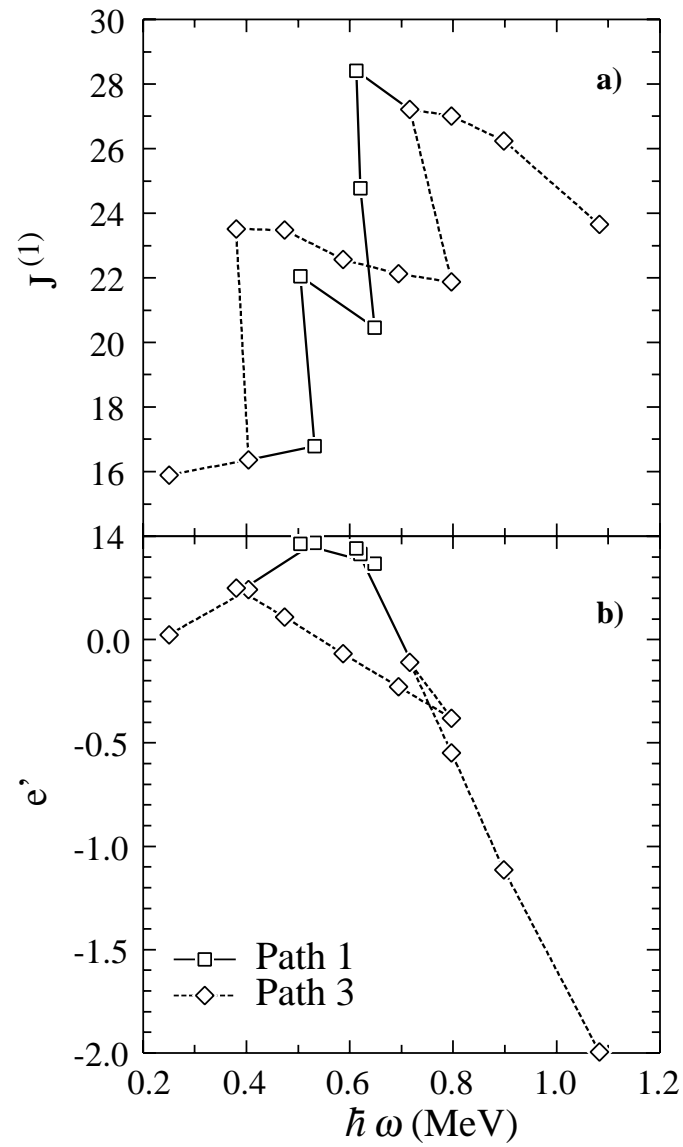


Figure 4.20: (a) Experimental $\mathfrak{J}^{(1)}$ and (b) Routhians for paths 1 (solid) and 3 (dashed), showing the backbends in each case.

these two paths. The kinematic moment of inertia along path 3 shows first an upbend at $\hbar\omega \approx 0.4$ MeV followed by a second upbend at $\hbar\omega \approx 0.8$ MeV. Changes similar to the first upbend have been observed in the isotones ^{83}Rb [35] and ^{87}Nb [31] where the proton number differs by two from that of ^{85}Y . It has been argued [33] that this change in ^{83}Rb and ^{87}Nb may be the result of the alignment of a pair of neutrons, a change in shape, or a combination of the two. The change in $\mathfrak{S}^{(1)}$ at the first upbend (path 3) exceeds that associated with the second upbend. The $\mathfrak{S}^{(1)}$ corresponding to path 1 behaves very differently; the first upbend occurs at $\hbar\omega \approx 0.5$ MeV which is immediately followed by an upbend at $\hbar\omega \approx 0.6$ MeV. The change in $\mathfrak{S}^{(1)}$ at the lower frequency is considerably smaller than that of the higher frequency. The experimental Routhians shown in Fig. 4.20b reflect the same behavior. The first upbend in path 3 is associated with a large change in slope (alignment) while the second upbend involves a smaller change in alignment. Along path 1, the first change in slope occurs at a higher frequency and is immediately followed by another large change in slope. States in the yrast sequence between $\hbar\omega > 0.4$ MeV and $\hbar\omega < 0.8$ MeV (band 3) have a nearly constant moment of inertia indicative of collective rotation.

4.2.4.2 Cranked mean-field calculations

Comparisons were made with cranked-shell-model calculations using a Woods-Saxon potential, monopole pairing, and Strutinsky shell correction. A more detailed description of the model may be found in references [29, 36].

Calculated total Routhian surfaces (Fig. 4.21) show five minima labeled ‘a’ through ‘e’ that exist over varying ranges of rotational frequencies. These minima

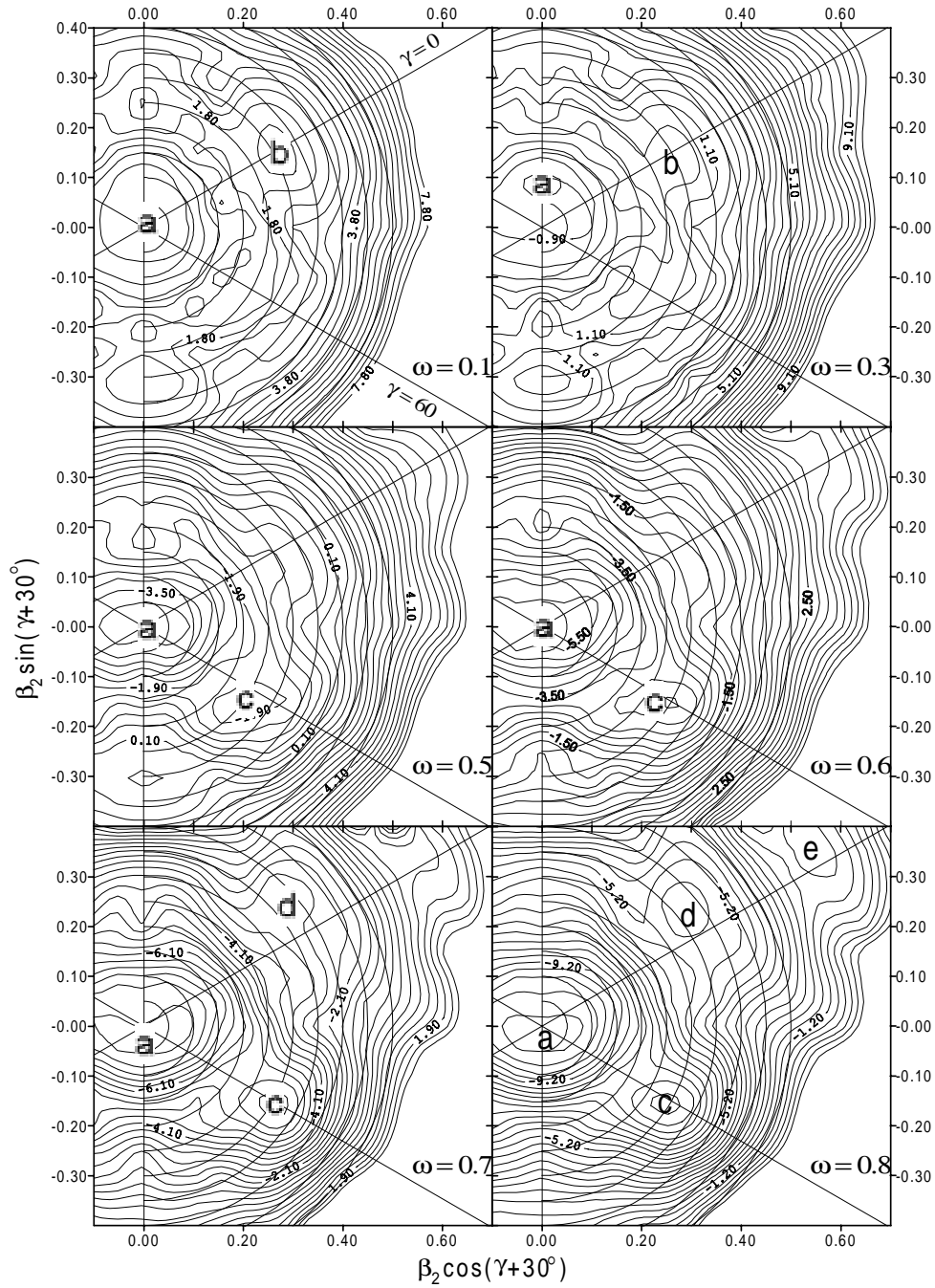


Figure 4.21: Total Routhian surfaces for $(\pi, \alpha) = (+, +)$ at cranking frequencies $\hbar\omega = 0.3, 0.6,$ and 1.0 MeV. Minima are labeled 'a' through 'e'. Equipotential lines are 1 MeV apart.

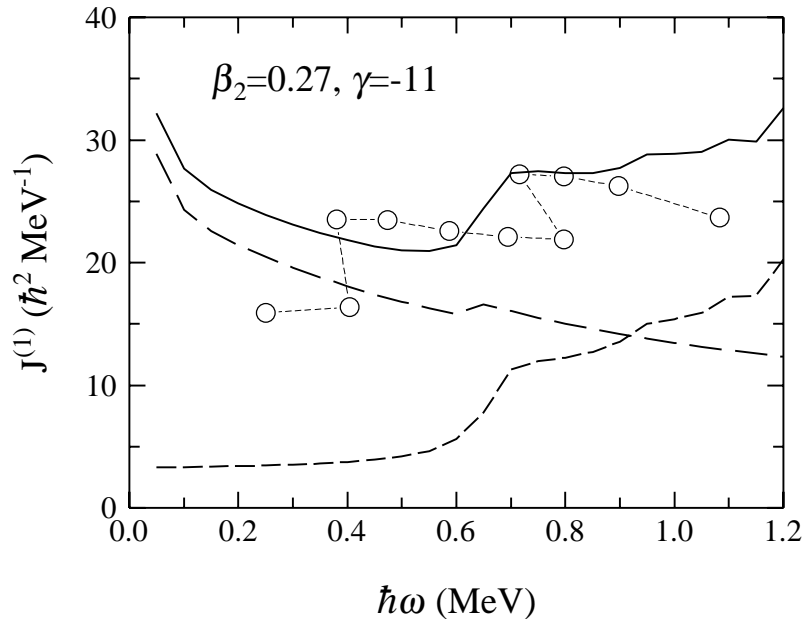


Figure 4.22: $\mathfrak{S}^{(1)}$ plot comparing experiment to HFBC calculations for lowest energy $(\pi, \alpha) = (+, +)$ prolate deformation ($\beta_2 = 0.27$, $\gamma = -11$, $\beta_4 = 0.010$). The circles indicate the data for band 3, the solid line indicates theory. The long and medium dashed lines represent the theoretical proton and neutron contributions respectively. The theoretical calculations are for $0.4 \text{ MeV} < \hbar\omega < 0.7 \text{ MeV}$.

correspond to deformations of (a) near-spherical ($\beta_2 < 0.05$, $\gamma \approx 0^\circ$), (b) prolate collective ($\beta_2 \approx 0.27$, $\gamma \approx 0^\circ$), (c) oblate collective ($\beta_2 \approx 0.25$, $\gamma \approx -60^\circ$). At $\hbar\omega > 0.7 \text{ MeV}$ two additional prolate collective minima exist at (d) $\beta_2 \approx 0.40$, $\gamma \approx 0^\circ$ and (e) $\beta_2 \approx 0.60$, $\gamma \approx 0^\circ$.

In this model, pairing was treated self-consistently at all frequencies. This makes it possible to compare theoretical $\mathfrak{S}^{(1)}$ to experiment. Previous work has shown that such comparisons are useful in determining shapes and shape changes [36, 37, 38].

Comparisons of the properties of the states belonging to bands 3 and 1 with model predictions show reasonable agreement with the assignment of prolate and oblate collective shapes, respectively. Figure 4.22 shows a plot of both the experimental $\mathfrak{S}^{(1)}$ for band 3 and the predicted $\mathfrak{S}^{(1)}$ of the collective prolate shape corre-

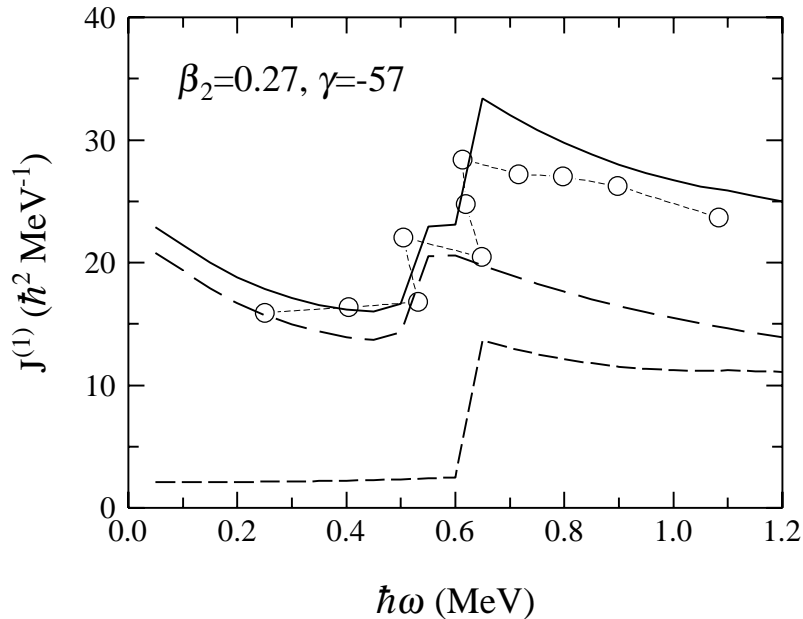


Figure 4.23: $\mathfrak{S}^{(1)}$ plot comparing experiment to HFBC calculations for lowest energy $(\pi, \alpha) = (+, +)$ oblate deformation ($\beta_2 = 0.27$, $\gamma = -57$, $\beta_4 = 0.010$). The circles represent data along decay path 1, the solid line indicates theory. The long and medium dashed lines represent the proton and neutron contributions respectively.

sponding to deformation b in Fig. 4.21. Due to shape change between near spherical at low spins and prolate collective, the model for the prolate collective shape does not reproduce the experimental points at low frequencies or the upbend at $\hbar\omega < 0.4$ MeV. Between the two upbends (i.e., in the frequency range of $0.4 \text{ MeV} < \hbar\omega < 0.7$ MeV), the model is in agreement with experiment. The frequency of the second upbend at $\hbar\omega \approx 0.7$ MeV is predicted slightly lower and not as sharp as the experimental upbend. (It should be noted that calculations of $\mathfrak{S}^{(1)}$ as a function of ω can only produce upbends, not backbends.) Since the calculated $\mathfrak{S}^{(1)}$ does not match the experimental values below the first backbend or above the second backbend, we suggest that the shape is only prolate along path 3 between $\hbar\omega = 0.4$ and 0.7 MeV.

Figure 4.23 compares a plot of the experimental $\mathfrak{S}^{(1)}$ for decay path 1 with the predicted $\mathfrak{S}^{(1)}$ corresponding to the collective oblate shape corresponding to deformation ‘c’ in Fig. 4.21. The calculation for this deformation closely reproduces the experimental data for path 1 above frequencies of about 0.2 MeV. Both the experimental and calculated $\mathfrak{S}^{(1)}$ values upbend at $\hbar\omega \approx 0.5$ MeV followed by a second upbend at $\hbar\omega \approx 0.6$ MeV. The magnitudes of each of these upbends are also predicted quite well. We thus suggest that the shape through path 1 remains oblate for all but the few lowest-energy states which, as mentioned before, we believe to be near spherical.

Using these comparisons for prolate and oblate shapes, the shape evolution for the positive parity, positive signature forking can be understood (as diagrammed in Fig. 4.19). Below the first backbend, the shape evolves from near spherical to oblate collective shape. During this evolution it forks into a prolate shape (yrast), and an oblate shape (band 1). Above $\hbar\omega \approx 0.8$ MeV the prolate minima disappears, and the oblate shape becomes yrast. The disappearance of the prolate minima is reproduced in the TRS plots (Fig. 4.21) where the prolate deformation disappears around $\hbar\omega \approx 0.6$ MeV.

4.2.4.3 Shape mixing and the decay out of the $37/2^+$ state

The forking of the decay out of the $37/2^+$ state into the oblate and prolate $33/2^+$ states at 6740 and 6361 keV requires some discussion. It could possibly be explained by strong mixing in the $37/2^+$ state between the two different shapes. This is consistent with the total Routhian surface at $\hbar\omega = 0.7$ MeV which show an oblate

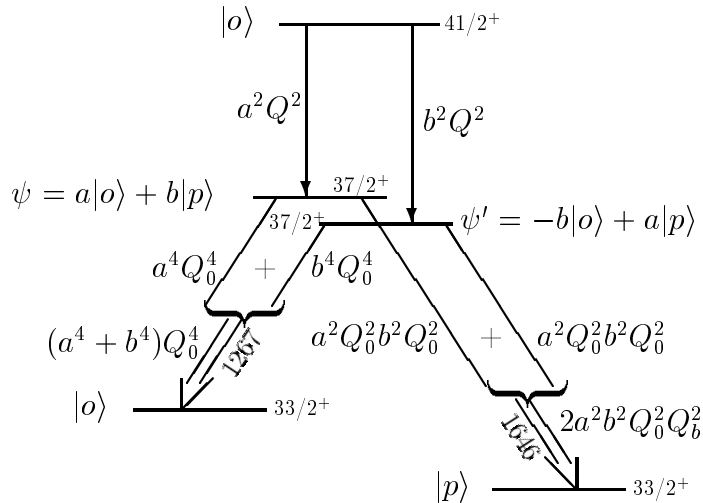


Figure 4.24: Schematic branching scheme. Note that the states ψ and ψ' are very close in energy. Their separation is exaggerated in the figure.

minimum (c) at approximately -3.5 MeV and a very soft, plateau-like prolate minimum (d) at approximately -2.5 MeV. The large signature splitting of single particle Routhians at approximately 0.7 MeV (see Fig. 4.24) indicates significant mixing between the $g_{9/2}$ orbitals of both protons and neutrons which may allow shape mixing to occur.

In the following we outline a schematic shape mixing model for this decay.

Let

$$\psi = a|o\rangle + b|p\rangle \quad (4.2)$$

and

$$\psi' = -b|o\rangle + a|p\rangle \quad (4.3)$$

describe two shape-mixed and mutually orthogonal $37/2^+$ states. The kets $|o\rangle$ and $|p\rangle$ represent oblate and prolate shape eigenstates, and a and b are normalized mixing amplitudes ($a^2 + b^2 = 1$). In order to obtain appreciable mixing it is necessary that the two $37/2^+$ states are close in energy. The separation is presumably less

than the energy resolution of the γ ray detectors, consistent with the fact that only a single $37/2^+$ state could be identified. We assume that the two wave functions above the states ψ and ψ' are pure $|o\rangle$ and those below pure $|o\rangle$ and pure $|p\rangle$ as indicated in Fig. 4.24. From these assumptions it is possible to calculate the relative strength of the 1267 and 1646 decays out of the $37/2^+$ states in terms of the $E2$ matrix elements $\langle o|E2|o\rangle$ and $\langle p|E2|p\rangle$ which in turn are proportional to the oblate and prolate intrinsic quadrupole moments Q_o and Q_p . Matrix elements of the form $\langle o|E2|p\rangle$ are neglected since they are generally expected to be very small based on the smallness of typical overlap integrals between the many-body wave functions. Thus the relative population strengths of states ψ and ψ' are $a^2Q_o^2$ and $b^2Q_p^2$, and the total reduced transition probabilities into the oblate and prolate $33/2^+$ states are proportional to $(a^4 + b^4)Q_o^4$ and $2a^2b^2Q_o^2Q_p^2$. The ratio of the two transition probabilities $B(E2; 1267)/B(E2; 1646)$ can be expressed in terms of the ratios $\kappa = (a/b)^2$ and $\lambda = (Q_o/Q_p)^2$:

$$\frac{B(E2; 1267)}{B(E2; 1646)} = \frac{\kappa^2 + 1}{2\kappa} \lambda \quad (4.4)$$

From the experimental relative intensities 4.1 and 6.1 of the 1267 and 1646 keV transitions one can extract the ratio of the reduced transition probability

$$\frac{B(E2; 1267)}{B(E2; 1646)} = \frac{4.1/1267^5}{6.1/1646^5} = 2.49 \quad (4.5)$$

The Routhian surfaces suggest that the magnitude of β_2 for the oblate and prolate shapes are about the same (i.e. $\beta_2 \approx 0.27$), hence $Q_o^2 \approx Q_p^2$ and $\lambda \approx 1$. Thus it is possible to determine the ratio $a^2/b^2 = \kappa = 4.77$ ($a^2 = 827, b^2 = 0.173$).

Chapter 5

SUMMARY

High spin structure of ^{80}Sr and ^{85}Y have been studied using high fold detector arrays, Gammasphere and Microball, and high resolution γ ray spectroscopy. Comparing the data to a cranked mean-field with pairing calculations, the shapes and shape changes for different values of angular momentum were investigated for each isotope.

In ^{80}Sr , cranked shell-model calculations show good agreement with experimental results, indicating a shape change from prolate collective to oblate collective. Lifetimes do not indicate a loss of collectivity in the spin range measured, however some evidence for shape evolution was seen at higher spins.

In ^{85}Y , the nuclear shape evolved from a spherical shape, at low excitations, to prolate and oblate shapes. At $I^\pi = 17/2^+$, the yrast band becomes prolate, and an oblate band branches from the yrast band. The oblate band then becomes yrast at $I^\pi = 37/2^+$, and the prolate band seems to disappear with a visible transition to the oblate band. A tentative new superdeformed band was identified. To be certain of this band, an experiment focused on the production of high spin states in ^{85}Y would be needed.

Bibliography

Bibliography

- [1] W.D. Myers and W.J. Swiatecki, *Nuc. Phys.***81**, 1 (1966).
- [2] Nilsson and Ragnarsson, “Shapes and Shells in Nuclear Structure”, Cambridge University Press (1995).
- [3] J. Dudek and Werner, *J. Phys. G4*, 1543 (1978).
- [4] J. Dudek and Werner, *J. Phys. G5*, 1359 (1979).
- [5] J. Dudek and Werner, *Phys. Lett.* 267B, 431 (1991).
- [6] Samuel M. Harris, *Phys. Rev.*138, B509 (1965).
- [7] I.Y. Lee, *Nuc. Phys.* A520, 641c (1990).
- [8] D.G. Sarantites, P.-F. Hua, M. Devlin, L.G. Sobotka, J. Elson, J.T. Hood, D.R. LaFosse, J.E. Sarantites, M.R. Maier, *Nucl. Instrum. Meth.* A3 61, 418 (1996).
- [9] J.R. Grover and J. Gilat, *Phys. Rev.* 157, 802 (1967).
- [10] R. Bengtsson, J.D. Garrett, “The Cranking Model”, World Scientific Publishing Co., *International Review of Nuclear Physics* Vol. 2 (1987).
- [11] M.A. Riley *et al.*, “Gammasphere The Beginning ... 1993-1997”, Florida State University (1998).
- [12] J.D. Jackson, “Classical Electrodynamics” 2nd edition, John Wiley and Sons (1975).
- [13] David Winchell, Ph.D. Thesis, “Investigation of the Structure of ^{75}Kr and ^{76}Br at High Angular Momentum”, University of Pittsburgh (1990).
- [14] D.C. Radford, *Nucl. Instrum. Methods Phys. Res.*A361, 306 (1995).
- [15] G. Palameta and J.C. Waddington, *Nucl. Instrum. Methods Phys. Res.*A234, 476, (1985).
- [16] Richard B. Firestone *et al.*, “Table of Isotopes, Volume II” 8th Edition, John Wiley and Sons, Appendix I-1 (1996).
- [17] H.J. Rose and D.M. Brink, *Rev.Mod.Phys* 39, 306 (1967).

- [18] R. Vaillancourt and P. Taras, Nucl.Instr. and Meth. 114, 333 (1974).
- [19] E. Der Mateosian and A.W. Sunyar, At. Data and Nucl. Data Tables 13, 391 (1974).
- [20] P. Taras and B. Haas, Nucl. Instr. Methods 123, 73 (1975).
- [21] R.F. Davie, D. Sinclair, S.S.L. Ooi, N. Poffe, H.G. Price, C.J. Lister, B.J. Varley, and I.F. Write, Nuc. Phys. A463, 683 (1987).
- [22] D.F. Winchell, V.Q. Wood, J.X. Saladin, I. Birriel, C. Baktash, M.J. Brinkman, H.-Q. Jin, D. Rudolph, C.-H. Yu, M. Devlin, D.R. LaFosse, F. Lerma, D.G. Sarantites, G. Sylvan, S. Tabor, R.M. Clark, P. Fallon, I.Y. Lee, A.O. Macchiavelli, Phys. Rev. C61, 44322 (2000).
- [23] J.C. Wells and N.R. Johnson, "LINESHAPE: a Computer Program for Doppler-Broadened Lineshape Analysis," ORNL Physics Division Progress Report for period ending September 30, 1991, No. ORLN-6689.
- [24] N.R. Johnson, F.K. McGowan, D.F. Winchell, C. Baktash, J.D. Garrett, I.Y. Lee, J.C. Wells, L. Chaturvedi, W.B. Gao, W.C. Ma, S. Pilotte, and C.H. Yu, Phys. Rev. C53, 671 (1996).
- [25] A.I. Kucharska, J. Billowes, and C.J. Lister. J. Phys. G **15** 1039 (1989).
- [26] A.A. Chishti, W. Gelletly, C.H. Lister, B.J. Varley, and Ö. Skeppstedt., J. Phys. G **16** 481 (1990).
- [27] D.H. Smalley, R. Chapman, P.J. Dagnall, C. Finck, B. Haas, M.J. Leddy, J.C. Lisle, D. Prévost, H. Savajols, and A.G. Smith., Nuc. Phys. **A611**, 96 (1996).
- [28] T.D. Johnson, A. Raguse, C.J. Gross, M.K. Kabadiyski, D. Rudolf, M. Weiszflog, T. Burkardt, J. Eberth, and S. Skoda., Z. Phys. **A350**, 189 (1994).
- [29] W. Nazarewicz, J. Dudek, R. Bengtsson, T. Bengtsson, and I. Ragnarsson, Nuc. Phys. A435, 397 (1985).
- [30] R. Diller, K.P. Lieb, L. Lühmann, T. Osipowicz, P. Sona, B. Wörmann, L. Cleemann, J. Eberth, Z. Phys. A321, 659 (1985).
- [31] A. Jungclaus, K.P. Lieb, C.J. Gross, J. Heese, D. Rudolph, D.J. Blumenthal, P. Chowdhury, P.J. Ennis, C.J. Lister, Ch. Winter, J. Eberth, S. Skoda, M.A. Bentley, W. Gelletly, B.J. Varley, Z. Phys. A340, 125 (1991).
- [32] S. Chattopadhyay, H.C. Jain, M.L. Jhingan, Phys. Rev. C50, 93 (1994).
- [33] D. Rudolph, C. Baktash, C.J. Gross, W. Satula, R. Wyss, I. Birriel, M. Devlin, H.-Q. Jin, D.R. LaFosse, F. Lerma, J.X. Saladin, D.G. Sarantites, G.N. Sylvan, S.L. Tabor, D.F. Winchell, V.Q. Wood, C.-H. Yu, Phys. Rev. C56, 98 (1997).

- [34] R. Bengtsson, S. Frauendorf, and F.-R. May, *At. Data Nucl. Data Tables* 35, 15 (1986).
- [35] W. Gast, K. Dey, A. Gelburg, U. Kaup, F. Paar, R. Richter, K.O. Zell, P. von Brentano, *Phys. Rev. C* 22, 469 (1980).
- [36] D.F. Winchell, M.S. Kaplan, J.X. Saladin, H. Takai, J.J. Kolata, and J. Dudek, *Phys. Rev. C* 40, 2672 (1989).
- [37] E. Landulfo, D.F. Winchell, J.X. Saladin, F. Cristancho, D.E. Archer, J. Döring, G.D. Johns, M.A. Riley, S.L. Tabor, V.A. Wood, S. Salem-Vasconcelos, and O. Dietzsch, *Phys. Rev. C* 54, 626 (1996).
- [38] D.F. Winchell, L. Wehner, J.X. Saladin, M.S. Kaplan, E. Landulfo, *Phys. Rev. C* 55, 111 (1997).

Index

cranked mean-field with pairing, 23

80sr, 50

85y, 73

angular distributions, 44, 76

backed target, 61

background subtraction, 42

coincidence analysis, 39, 52

coincidence cube, 40

coincidence matrix, 40, 43

cranking model, 19, 23, 28, 64, 68

deformation, 7

double gates, 40

gates, 40

gating, 40

level scheme, 52

liquid drop model, 26

mixing ratios, 44

Nilsson model, 14

nuclear density, 12

pairing, 24

Routhians, 20, 23

semi empirical mass formula, 4

shape parameters, 7

single gates, 40

single particle Routhians, 20, 23

Spherical Shell Model, 11

Strutinsky shell correction, 26

Woods-Saxon potential, 12